

# Atomic Scale Investigation of Pressure Induced Phase Transitions in the Solid State

DISSERTATION

zur Erlangung des akademischen Grades

Doctor rerum naturalium

(Dr. rer. nat.)

vorgelegt

der Fakultät Mathematik und Naturwissenschaften

der Technischen Universität Dresden

von

**M. Sc. Salah Eddine Boulfefel**

geboren am 25.05.1979 in Constantine, Algerien

Eingereicht am: 21.07.2009

Die Dissertation wurde in der Zeit von 10/2004 bis 07/2009  
im Max-Planck-Institut für Chemische Physik fester Stoffe angefertigt.



to my parents

Publications:

*Intrinsic Nucleation Mechanism at the Paraelectric to Ferroelectric Phase Transition in BaTiO<sub>3</sub>*

M. Pasciak, S. E. Boulfelfel, and S. Leoni  
submitted to Phys. Rev. Lett. (2009)

*Competing intermediates in the pressure-induced wurtzite to rocksalt phase transition in ZnO*

S. E. Boulfelfel and S. Leoni  
Phys. Rev. B **78**, 125204 (2008)

*Walking the path from B<sub>4</sub>- to B<sub>1</sub>- type structures in GaN*

S. E. Boulfelfel, D. Zahn, Yu. Grin, and S. Leoni  
Phys. Rev. Lett. **99**, 125505 (2007)

*Low-dimensional sublattice melting by pressure: Superionic conduction in the phase interfaces of the fluorite-to-cotunnite transition of CaF<sub>2</sub>*

S. E. Boulfelfel, D. Zahn, O. Hochrein, Yu. Grin, and S. Leoni  
Phys. Rev. B **74**, 094106 (2006)

*Structural preference versus metal within the MB<sub>2</sub>C<sub>2</sub> (M = Mg, Sc, Ca, Y, Ln) phases: the coloring problem revisited by DFT calculations*

X. Rocquefelte, S. E. Boulfelfel, M. Ben Yahia, J. Bauer, J.-Y. Saillard,  
and J.-F. Halet  
Angew. Chem. Int. Eng. Ed. **117**, 7714 (2005)

---

# Contents

---

<b>Motivation</b>	<b>1</b>
<b>1 Introduction</b>	<b>3</b>
1.1 Types of Phase Transitions . . . . .	3
1.2 Theories of Phase Transitions . . . . .	5
1.2.1 Classical Nucleation Theory . . . . .	5
1.2.2 Landau Theory for Continuous Phase Transitions . . . . .	6
<b>2 Phase Transition Simulations</b>	<b>11</b>
2.1 Rare Events in Complex Systems . . . . .	11
2.2 Transition State Theory . . . . .	13
2.2.1 Open-end Methods . . . . .	14
2.2.2 Two-end Methods . . . . .	15
2.2.3 Limitations . . . . .	15
2.3 Transition Path Sampling . . . . .	16
2.3.1 Importance Sampling of Trajectory Space . . . . .	17
2.3.2 Defining the Transition Path Ensemble . . . . .	18
2.3.3 Sampling the Transition Path Ensemble . . . . .	20
2.4 Methodology Development . . . . .	26
2.4.1 Chemical Substitution and Defects Incorporation . . . . .	27
<b>3 Phase Transitions in Semiconducting Materials</b>	<b>32</b>
3.1 Gallium Nitride, GaN . . . . .	32
3.1.1 Polymorphism . . . . .	32
3.1.2 Electronic Structure and Equilibrium Properties . . . . .	33
3.1.3 Phase Transition Models . . . . .	34
3.1.4 Wurtzite-to-Rocksalt (B4-B1) Phase Transition . . . . .	38
3.2 $\text{Al}_x\text{Ga}_{(1-x)}\text{N}$ and $\text{In}_x\text{Ga}_{(1-x)}\text{N}$ Solid Solutions . . . . .	45
3.2.1 Substitution of Gallium with Indium . . . . .	46
3.2.2 Substitution of Gallium with Aluminum . . . . .	48

3.3	Zinc Oxide, ZnO . . . . .	51
3.3.1	Polymorphism . . . . .	51
3.3.2	Electronic Structure and Equilibrium Properties . . . . .	53
3.3.3	Phase Transition Models . . . . .	54
3.3.4	Wurtzite-to-Rocksalt (B4-B1) Phase Transition . . . . .	56
<b>4</b>	<b>Phase Transitions in Superionic Materials</b>	<b>66</b>
4.1	Calcium Fluorite, CaF <sub>2</sub> . . . . .	66
4.1.1	Polymorphism . . . . .	66
4.1.2	Electronic Structure and Equilibrium Properties . . . . .	68
4.1.3	Crystallographic Aspects of The Phase Transition in CaF <sub>2</sub> . . . . .	69
4.1.4	Solid- <i>Solid</i> -Solid Regime . . . . .	72
4.1.5	Solid- <i>Liquid</i> -Solid Regime . . . . .	73
4.2	Silver Iodide, AgI . . . . .	78
4.2.1	Polymorphism and Properties . . . . .	78
4.2.2	Transition Models . . . . .	81
4.2.3	Wurtzite/Zinblende-to-Rocksalt (B4/B3-B1) Phase Transition . . . . .	81
<b>5</b>	<b>Phase Transitions in Elements</b>	<b>89</b>
5.1	Phosphorus, P . . . . .	89
5.1.1	Polymorphism and Properties . . . . .	89
5.1.2	Phase Transition Models . . . . .	92
5.1.3	Orbital Localization in Phosphorus from Maximally Localized Wannier Functions . . . . .	93
5.1.4	Orthorhombic A17 to Rhombohedral A7 Phase Transition . . . . .	95
	<b>Conclusions and Outlook</b>	<b>103</b>
	<b>Bibliography</b>	<b>105</b>
	<b>Acknowledgements</b>	<b>112</b>

# List of Figures

1.1	Different approaches of phase transitions classifications. . . . .	4
1.2	Plot of Landau free energy for temperatures above and below the transition temperature. The equilibrium value of the order parameter $\eta$ is given by the minimum of the free energy. At high temperatures ( $T \geq T_c$ ) there is a single minimum at $\eta = 0$ . At low temperatures ( $T \ll T_c$ ) the free energy has a maximum at $\eta = 0$ and minima at non-zero values of $\eta = \pm\eta_0$ . . . . .	7
1.3	The dynamic evolution (thin lines) labeled by the number of dynamical iterations of free energy minima flooding using metadynamics method. . . . .	9
2.1	Schematic representation of a dynamical trajectory of a system crossing between two basins of long-lived states A and B (blue regions). The system spends the majority of the time wandering within basins A and B, while the crossing is fleeting. Colors: blue, green, yellow, and red reflect an ascending energy scale. . . . .	12
2.2	Time evolution of a dynamical trajectory of system crossing from state A to state B. Residence times spent in the states are very long compared to the time needed to switch between states. A and B can be distinguished using an order parameter like the coordination number of an atom. . . . .	13
2.3	Schematic illustrating the crossover between two different states in the framework of the transition state theory. . . . .	14
2.4	Schematic illustration of two types of potential energy surface topologies as controlled by (a) energetic effects (2 <sup>nd</sup> order phase transitions) and (b) entropic effects (1 <sup>st</sup> order phase transitions). Color scale distinguishes between low energy (blue) and high energy (red) regions. . . . .	16
2.5	Schematic illustrating (a) a shooting move and (b) a shifting move, two essential steps in the transition path sampling method. (a) The atomic momenta of randomly chosen time slice $x(t)$ from an existing trajectory are slightly modified (a). (b) Propagating the modified state forward and backward in time is accepted if transition is observed. Otherwise (c) the failed trajectory is rejected. . . . .	22

vi LIST OF FIGURES

2.6 Transition path sampling iterations at work: (a) a state (black square) is randomly chosen from an existing  $A \rightarrow B$  trajectory and a new trajectory is shot off in direction of  $A$ . If successful, trajectory is retained, and another shooting point is chosen from it. (b)-(c) The shooting step is repeated in both directions,  $A \rightarrow B$  and  $B \rightarrow A$ , shifting both limits of the shooting window until trajectory decorrelation is achieved. . . . 25

2.7 Different simulation levels of the chemical doping procedure. The core simulation (Inner layer) describes the time evolution of the system in configuration space to produce dynamical trajectories. The latter are sampled by (Monte Carlo) random walk in trajectory space (Middle layer). Chemical composition of the system is systematically modified using a stepwise Monte Carlo procedure (outer layer). Doping moves are separated by intervals of TPS iterations to relax the modified system to its favorable transition regime. . . . . 27

2.8 Diagram summarizing different steps of chemical doping procedure. Starting point is a reactive trajectory taken from TPS simulation. Substitution of atoms is only depending on the reactivity of the generated trajectory. The perturbation caused by substitution is accommodated by immediate sampling of the modified system. . . . . 29

2.9 Schematic illustration of small and local changes in energy landscape resulting from chemical substitution. (a) Complex energy landscape corresponding to initial transition regime is systematically perturbed by small changes, (b) and (c). The topology and location of energy bottlenecks is changed lowering probability and reactivity of actual transition pathway. At the same time, other energy bottlenecks appear, compelling the system to another transition route (d). The change in transition regime is a direct result of stepwise substitution. Colors: blue, green, yellow, and red reflect an ascending energy scale. . . . . 31

3.1 GaN polymorphs: (left) the wurtzite – B4, (middle) the zincblende – B3, and (right) the rocksalt – B1 type structures. . . . . 33

3.2 Total energy vs volume for GaN polymorphs . . . . . 34

3.3 Three types of common cell orientation for building transition models for the B4–B1 phase transformation in GaN. TP1, TP2, and TP3 models are described in common subgroups  $Cmc2_1$ ,  $Pna2_1$ , and  $P2_1$ , respectively . . . . . 35

3.4 Two transition models for B4-to-B1 phase transformation in semiconducting materials (GaN, AlN, InN, ZnO, CdSe, etc . . .). The blue path is achieved through a hexagonal intermediate structure ( $P6_3/mmc$ ). The red path is realized through a tetragonal intermediate structure ( $I4mm$ ). Both intermediates have fivefold coordinated atoms. . . . . 36

3.5 Model transformation mapping the network of (a) B4 onto the network of (c) B1. The Ga (gray) and N (red) atom sets are separated from each other by a PNS (the corresponding gray/green manifold is displayed). The latter develops perpendicularly with respect to shortest Ga–N connections. Figure 1(b) represents an intermediate between (a) and (c). 38



3.6	Enthalpy vs. pressure of GaN polymorphs . . . . .	39
3.7	Time evolution of Ga average coordination number (CN) during the B4–B1 transformation in the course of transition path sampling iterations. Green curves correspond to early trajectories produced during sampling. Blue curves mark local appearance of tetragonal intermediate $iT$ . Red curves are characterized by predominance of $iT$ in early stages of transformation and during reconstruction of WZ structure. Black curve is a representative profile of Ga CN variation corresponding to real mechanism. Therein, $iT$ appears as metastable phase as indicated by the plateau at CN=5. . . . .	40
3.8	Snapshots taken from a representative trajectory of B4–B1 transition mechanism in GaN. Front view, parallel to $(001)_{B4}$ , is shown. Ga atoms are colored according to coordination number. Nucleation centers appeared at $t = 0$ ps. Interface is created via $(001)_{B4}$ layers shearing between $t = 3$ and $t = 4$ ps. WZ structure is completely transformed into intermediate structure with fivefold coordinated atoms, $iT$ , at $t = 5$ ps. Transformation into RS structure is accompanied with CN increase from 5 to 6 between $t = 5$ to $t = 8$ ps. . . . .	42
3.9	Snapshots taken from a representative trajectory of B4–B1 real transition mechanism in GaN. Side view, along $[001]_{B4}$ , is shown. While relative spacing between sublattices in WZ is not changed, intermediate structure with fivefold coordinated atoms is formed because of $(001)_{B4}$ layers shearing ( $t = 0 - 5$ ps). Inset on the intermediate metastable structure $iT$ indicates a pyramidal environment in a tetragonal cell described in space group $I4mm$ . Transformation into RS structure is realized by $iT$ structure compression along $[001]_{iT}$ . The overall B4–B1 transition mechanism is a two-step transformation. . . . .	43
3.10	Two different fashions of $(001)_{B4}$ 6-rings compression into $(001)_{B1}$ squares	44
3.11	Early stages of the B4→B1 transformation in pure GaN (upper) and after (lower) doping with In (grey polyhedra). Grouping in small clusters is preferred by In atoms to minimize strain caused by cell parameter difference between GaN and InN. $(001)_{B4}$ layers shearing direction, marked by blue long arrow, is maintained after doping. Nucleation of intermediate structure $iT$ is preferentially started at In clusters. . . . .	47
3.12	The variation of coordination number of Ga atoms during B4→B1 transformation in pure GaN (black curve) and after (red curve) doping with Al . . . . .	48
3.13	Early stages of the B4→B1 transformation in pure GaN (upper) and after (lower) doping with Al (grey polyhedra). $(001)_{B4}$ layers shearing direction, marked by blue long arrow, is modified as a result of transition regime change. Nucleation of intermediate structure $iT$ is preferentially started off Al sites. The latter are spread in simulation box to avoid quenching the transition path through tetragonal intermediate $iT$ . . . . .	49
3.14	Phase boundary between wurtzite and rocksalt phases of ZnO. . . . .	52

3.15	The $sp^3$ hybridization in the WZ structure of ZnO represented by maximally localized Wannier functions. . . . .	53
3.16	Hexagons deformation in the hexagonal network in WZ ZnO parallel to (001) according to (left) $Cmc2_1$ , (middle) $Pna2_1$ , and (right) the simplest combination of both. . . . .	54
3.17	Schematic drawing of two possible Peierls distortions: chair-type (upper) and boat-type (lower) for the RS (left) $\rightarrow$ WZ (right) transformation. . . . .	55
3.18	Snapshots taken from a representative trajectory corresponding to the favorable transition mechanism of WZ–RS transformation in bulk ZnO. Transition is initiated by $(001)_{B4}$ layers shearing (direction marked by black arrows). Further growth of high pressure modification, RS, is developed perpendicular to shearing direction, until transition is completed. . . . .	57
3.19	The internal structural parameter $u$ of WZ ZnO as a function of pressure. The parameter $u$ is the $z$ coordinate of atom in position $2(b)$ and corresponds to the cations and anions sublattices spacing. . . . .	58
3.20	Snapshots taken from a trajectory corresponding to a less-favored transition path going through hexagonal $iH$ intermediate (b). Before layers shearing is initiated (c), the system is compressed along $[001]_{B4}$ and $iT$ is formed (a)-(b). As soon as WZ reconstruction is started, the system is again relaxed into WZ structure (b)-(c). . . . .	59
3.21	Intermediate motifs $iT$ (left) and $iH$ (right) appearing during distinct TPS simulation runs with corresponding structural extents during the transformation (upper panel). . . . .	60
3.22	Volume variation profiles of transition paths visiting the $iH$ (continuous line) or bypassing it (dashed line). . . . .	61
3.23	Defects formation due to intermediates competition during a B1 $\rightarrow$ B4 transition. (a)-(b) The reverse transition, B1 $\rightarrow$ B4, is achieved via layers shearing. Competition between intermediate structures, $iH$ and $iT$ , caused the survival of RS island (c). Local resolution of RS fraction resulted into defects (d)-(f). . . . .	63
3.24	Scheme of the displacement vectors associated with the six different phonon modes of WZ ZnO at the $\Gamma$ point. . . . .	64
4.1	CaF <sub>2</sub> polymorphs: the ambient conditions fluorite structure (left) and the high-pressure modification PbCl <sub>2</sub> -type structure cotunnite (right). Structures are shown in double unit cells. . . . .	67
4.2	Group-subgroup relations between the space groups of the fluorite (top) and the cotunnite (bottom) polymorphs of CaF <sub>2</sub> . . . . .	70
4.3	Geometric model used as a starting transformation route of CaF <sub>2</sub> from the cubic structure (a) to the orthorhombic (c), over an orthorhombic intermediate structure ( $Immm$ ) (b). . . . .	71
4.4	Reconstruction of the Ca <sup>2+</sup> sublattice via layer shearing along $[011]$ . Antiparallel shifts within adjacent (100) layers in the fluorite causes the reorientation of half octahedral voids highlighted by green polyhedra (lower panel). . . . .	73

4.5	Local changes in atomic arrangements highlighting the different stages of the cubic-to-orthorhombic transition in $\text{CaF}_2$ . . . . .	74
4.6	Fluoride ions mobility highlighted with illuminated lines. (upper panel) Early stage of transformation is marked by high anionic mobility causing the reconstruction of cation sublattice. (lower panel) Percolation of anions via fluorite octahedral voids creates a front of anion sublattice local melt. Octahedra reorientation (red and green polyhedra) solidifies again the $\text{F}^-$ sublattice in the high pressure structure. . . . .	76
4.7	Two group-subgroup relations reflecting different symmetry aspects of (red path) the geometric model of the initial regime, and (blue path) the different symmetry-lowering steps identified during the simulations. . . . .	77
4.8	Phase diagram of $\text{AgI}$ . . . . .	78
4.9	Polymorphs of $\text{AgI}$ . Phases I, II, and II' are also known as $\alpha$ , $\beta$ , and $\gamma$ , respectively. . . . .	79
4.10	Different $\text{AgI}$ polytypes represented in terms of close-packed iodine tetrahedra occupied by silver ions. The stacking sequences are represented by ABC and <i>hc</i> notations. . . . .	80
4.11	Geometric model based on transforming periodic nodal surfaces connecting the WZ structure to the RS structure of $\text{AgI}$ over an ordered intermediate configuration. . . . .	82
4.12	The $\text{RS} \rightarrow \text{WZ/ZB}$ transformation mechanism in $\text{AgI}$ . Different phases are identified and colored according to their $\text{Ag}^+$ ions coordination polyhedra: grey for octahedra, dark and light blue for fourfold coordination to emphasize ABAB and ABC stacking in WZ and ZB respectively. . . . .	83
4.13	Two final configurations resulting from the simulations on the $\text{RS} \rightarrow \text{WZ/ZB}$ transformation in $\text{AgI}$ . Different WZ/ZB stacking sequences are identified and highlighted. . . . .	84
4.14	Traces of longest $\text{Ag}^+$ movements in the form of a cascade piercing many layers along the mixed WZ/ZB system. . . . .	85
4.15	A representative path of $\text{Ag}^+$ ion long movement within WZ $\text{AgI}$ . . . . .	86
4.16	A representative path of $\text{Ag}^+$ ion long movement within ZB $\text{AgI}$ . . . . .	87
5.1	Polymorphs of phosphorus: (a) black phosphorus P1 (A17), (b) As-I like PV (A7), (c) PVIII ( <i>bcc</i> ), (d) PVII ( <i>sh</i> ), (e) PVI ( <i>sc</i> ), (f) incommensurate PIV ( <i>ic</i> ), and (g) white phosphorus P4. . . . .	90
5.2	Dependence of the atomic volume on pressure for phosphorus solid phases. . . . .	91
5.3	Symmetry relationships between space groups of A17 (blue frame) and A7 (red frame) phases of P based on a displacive approach of the transformation. Three paths are proposed: one going through a common subgroup (green path) and two paths implying a symmetry upgrade to ensure the connection (black paths). . . . .	92
5.4	Local reorientation of a lone pair associated with the A17-A7 phase transition in P pictured via a schematic representation of lone pair flipping between two local environments corresponding to both structures. . . . .	93

5.5	Maximally localized Wannier functions projected on $3s$ and $3p$ states of P for both PI (upper row) and PV (lower row) phases. The $\sigma$ bond like character for the three first functions corresponding to P–P contacts is displayed ((a)-(c) and (e)-(g)), while the <i>pillow</i> shape ((d) and (h)) is a clear signature of an orbital carrying a lone pair. The ensemble of the four MLWFs indicates, for each structure, an $sp^3$ hybridized bonding picture. . . . .	94
5.6	Common cells (solid black lines) used to relate atomic positions in the (a) PI structure and the (b) PV structure using a monoclinic subgroup $P2/c$ . . . . .	95
5.7	Snapshots taken from a representative trajectory of the real mechanism for the PI-PV phase transition. Both front (upper row) and side (lower row) views are shown for better visibility of relevant atomic displacements along the transition. The nucleus marking the onset of the $A7 \rightarrow A17$ (or $A17 \rightarrow A7$ ) transition is highlighted by blue (or red) circle. . . . .	96
5.8	Total and projected densities of states for phosphorus in the normal pressure (left) A17 structure and (right) the high pressure A7 structure. Fermi level is set to zero. . . . .	97
5.9	Changes of two MLWFs of a selected atom during the A17-A7 transformation. Two MLWFs are shown. The opaque function is initially associated with a lone pair, and the transparent one with a $\sigma$ P–P bond. The overall picture emphasizes a lone pair $\leftrightarrow$ simple bond conversion mechanism during the A17-A7 transition in phosphorus. . . . .	98
5.10	Schematic diagram of the frontier molecular orbitals of P in a threefold symmetry. Blue and red lines represent the correspondence between states after phase transition. . . . .	99
5.11	Isolines of the valence charge density projected on $(100)_{A17}$ in the phase coexistence regime of A17 and A7 structures. An low dimensional (1D) intermediate structure in the form of a polymeric chain of equidistant P atoms in zigzag fashion is formed along $[010]_{A17}$ . Isostructural to a $-(CH_2)_n-$ polymer, the $-(PP_2)_n-$ chain is formed at the interface between PI and PV phases. It is associated with a Peierls instability that facilitates the transition between two types of pairing P atoms in PI and PV. . . . .	101

# Motivation

*"It was like a huge wall!," said a blind man.  
"Oh, no! It was like a big tree," said another blind man.  
"You are both wrong! It was like a large fan!," said another.  
After listening to the blind people, the Lord said,  
"Alas! None of you have seen the elephant!"*

From East-Indian folklore

In nature and in laboratory experiments, structural phase transitions are common phenomena that can be induced by pressure or temperature. In the solid state, they play an important role in the discovery of new phases with different chemical and physical properties. While high temperature usually causes amorphization, disorder, and melting of materials, transformations on increasing pressure often leads to crystalline polymorphs with a defined symmetry because they are volume restricted. With the recent progress in diamond-anvil-cell and shock-wave techniques, the study of solids under several hundred GPa is made possible. Under such conditions, properties like mechanical stability, ferroelectric response, conductivity switching, magnetic ordering, mass and electronic transport, differ from those studied and observed at normal conditions. Nonetheless, acquiring a firm and precise understanding of atomistic mechanisms of structural changes accompanying phase formation at high-pressure remains a challenging problem.

Dividing structural phase transformations into first and second order transitions implies considering the Gibbs free energy derivatives. If the first derivative is discontinuous, the transition is called reconstructive, and it involves bond breaking, large volume change, latent heat exchange, and hysteresis effects. If the second derivative is discontinuous, the transition is called displacive, and on the contrary to reconstructive transitions, bonds and volume are preserved along transformation with typically small atomic displacements. The continuous change of observables during second order transformations is at the basis of many approaches for studying transitions.

The construction of an analytical free energy function, then minimizing it over a predefined order parameter in function of temperature or pressure, represent the basic idea of Landau theory of phase transitions which has been successfully applied to continuous second-order transformations. Phenomenological in nature, nothing is *a priori* known about the form of the free energy function. Whereas this is a strong point in order to highlight universal features, it is clear that any useful assumption

## 2 Motivation

about the free energy form requires a fair understanding of the transition beforehand.

The efforts to generalize the success of Landau theory to include first-order transitions take advantage of special cases of existence of group-subgroup relationships between the transforming phases for the definition of an order parameter. However, for most reconstructive transformations, such a relationship is missing. Consequently, the choice of an order parameter is no longer unique and defining it is not a trivial task.

To approach the problem of a missing symmetry relationships in first-order transitions, theories based on common subgroup paradigm have been developed. Lowering the symmetry of the transforming structures into a common cell enables for a mapping of atomic positions from one structure into the other. The transition is described using the set of degrees of freedom allowed in the common subgroup. Many symmetry paths may exist, and the choice of the appropriate common cell decides which are the degrees of freedom to consider, or to freeze. This assumption typically results into biased transition mechanisms.

Reconstructive transitions proceed by nucleation and subsequent growth of the new phase within the initial one. Such a critical phenomena are accounted for in classical nucleation theory. Therein, the thermodynamics of the process of nucleation is expressed in terms of a competition between a volume term that favors formation and growth of nucleus, and a surface term that favor its dissolution. The theory allows for a good estimation of transition rates. However, the dependence of some constants in the formulation of free energy on external parameters like temperature, and the unknown basic form of the nuclei, have limited the application of nucleation theory to the elucidation of atomistic mechanisms of reconstructive transformations.

The success of different theories in capturing a given aspect of first-order transitions does not help guessing other relevant aspects and effect on different properties. Gathering evidence for an atomistic mechanism of pressure induced structural reconstruction in the solid state entails working out an atomistic landscape that allows for detailed understanding of local structural rearrangement in the phase coexistence regime.

The main purpose of this work is to mark the departure of reconstructive transitions investigation from the static, geometric, concerted, and mean field approaches. The mechanistic elucidation of transformation mechanisms are given with fair account to nucleation and growth phenomena. Phase coexistence is simulated by means of molecular dynamics simulations and using an advanced method, transition path sampling, which is devised for the study of critical events with first-order thermodynamics.

A variety of compounds (GaN, ZnO, CaF<sub>2</sub>, and AgI) and elemental phosphorus are selected and investigated in order to cover different problematics raised by both theory and experiments in the field of high-pressure induced phase transitions. This collection of compounds allows for studying the behavior of different types of properties and bonding in the solid state.

Apart of the search for atomistic description of transition mechanisms, symmetry and chemical reactivity in the solid state are recast into a new perspective, where a structural transformation is regarded as a chemical reaction.

---

# 1

# Introduction

---

## 1.1 Types of Phase Transitions

The early attempts to classify phase transitions in the solid state were based on the monitoring of the rate at which the transition was achieved. Later, several approaches have been used to describe phase transformations in general, based on different aspects of the transition: kinetic, thermodynamic, and structural [Figure 1.1 (adapted from Ref. [1])].

- **The kinetic approach** considers the transition rate and the activation energy between polymorphs of a given compound. Phase transitions are divided into two main categories: sluggish and rapid. In the first category, the activation energy is very high and the transition is very slow with a large hysteresis and quenchable. If the activation energy decreases under reduction of hysteresis and quenchability, the transition belongs to the second category. In this respect, different behaviors are possible: enantiotropic, if the transition is reversible, or monotropic, if the transition proceeds in only one direction and is irreversible.

However, after recent advances in the field of high-pressure experiments, the limit of the quenchability has become very flexible. Moreover, no property of either phases is treated. In this respect, the kinetic approach appears to be limited.

- **The thermodynamic approach** examines the change in the Gibbs free energy,  $G$ , as a function of a parameter  $Z$ , such as temperature, pressure, magnetic field, or electric field. According to Ehrenfest [2], a phase transition is said to be of  $n^{th}$  order, where  $n$  is the smallest number for which at least one of the free energy derivatives with respect to  $Z$  is discontinuous. Under this scheme, first-order phase transitions exhibit a discontinuity in the first derivative of the free energy with a thermodynamic variable. The various solid/liquid/gas transitions are classified as first-order transitions because they involve a discontinuous change in density (which is the first derivative of the free energy with respect to chemical potential). Second-order phase transitions are continuous in the first derivative but exhibit discontinuity in a second derivative of the free energy.

Ehrenfest's approach has proven very useful for classifying phase transitions.

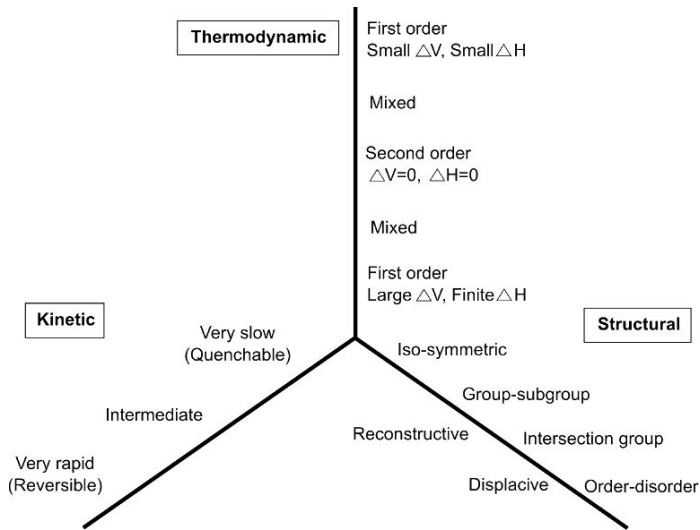


**Figure 1.1:** Different approaches of phase transitions classifications.

However, limitations have arisen because of the divergence of the derivative of free energy at continuous transformations, not known at the time of theory formulation. For instance, in some ferromagnetic transitions, the heat capacity diverges to infinity [3].

- **The structural approach** compares the structures of the polymorphic phases before and after the transformation. According to Buerger [4], there are two types of phase transformation in the solid states: displacive and reconstructive. If a transition does not involve breakage of primary bonds in order to interconvert crystal structures, the transition is called displacive. The crystal structures are often related in terms of group-subgroup relationship and the required activation energy is low. In contrast, if bonds are broken and the atoms are rearranged, the transition is termed reconstructive. The corresponding activation energies are quite high.

Displacive transitions are topotactic, i.e. the crystallographic axes of the two limiting structures show well-defined orientation relationships. The atomic migration paths are often derived from such relationships. The degree of topotaxy decreases as more bonds are being broken during the transformation. The atomic migration paths show an increasing deviation from any modeling based on cell orientation relations.

Thermodynamically, reconstructive phase transitions show discontinuities in the first-order free energy derivatives (entropy and volume) as a result of the change in the atomic environment at the transition. Whereas, displacive transitions can be second-order in character.

Sometimes, displacive transitions can be thermodynamically first-order if close



relationship exists between symmetries of the structures involved. The first-order character arises in fact because the intermediate states are higher in energy than the structures of polymorphic phases at the transition.

Martensitic and related transformations [5], despite their diffusionless and continuous character, display large structural distortions and coordination changes [6]. Therefore, in the literature, they are classified as displacive, or as reconstructive [7]. In general, the distinction between transformation types is by no means unambiguous, and is related to a phenomenological rather than an atomistic understanding of the transition.

The exceptions incurred by the limitations of the approaches described above can be avoided by considering the latent heat. In this case, transitions can be divided into two broad categories similar to the Ehrenfest classes [8–10]. If a transition involves a variation in the latent heat [11], then it is of first-order character. The system either absorbs or releases a fixed, and typically large, amount of energy during the process of the transition without variation in the temperature of the system.

Because energy cannot be instantaneously transferred between the system and its environment, first-order transitions are associated with *phase coexistence* regimes in which some parts of the system have completed the transition and others have not. Such a transformation scenario is known to involve a *nucleation and growth* process. Many important phase transitions belong to this category, including the pressure-induced phase transitions in the solid state. If no latent heat is associated with the transition, and the transformation can be well described using a continuous model, it is a second-order phase transition.

Phase fluctuations occur as random events due to the thermal vibration of atoms that can be influenced on varying temperature or pressure. An individual fluctuation may be associated with a reduction in free energy, but it can only survive and grow if there is a reduction. The cost associated with the creation of a new phase within another one, the interface energy, is a penalty which becomes smaller as the particle surface to volume ratio decreases. In a metastable system, this leads to the critical size of fluctuation beyond which growth is favored. If the nucleation is not taking place at an impurity or initiated by a foreign element to the system, then it is called homogeneous. Theoretically, homogeneous nucleation is described by classical nucleation theory (CNT) [12].

## 1.2 Theories of Phase Transitions

### 1.2.1 Classical Nucleation Theory

At the end of the 19<sup>th</sup> century, the attempt of J. W. Gibbs to theoretically describe the formation of new phase [12, 13] constitutes the basic idea of what was later formulated as classical nucleation theory, after different stages of development and modification [14].

Let us consider a metastable state that evolves toward a stable equilibrium state under formation of localized droplet fluctuating around a critical size. The critical energy for the formation of a droplet is determined by a competition between a volume

## 6 1. Introduction

(bulk) term, that favors creation of the droplet, and a surface term, that favors its dissolution. The critical radius  $R_c$  results from this competition: droplets of size  $R > R_c$  will grow, while droplets with  $R < R_c$  will shrink. The difference in free energy can be stated for a general case of phase  $\alpha$  being nucleated within phase  $\beta$ <sup>1</sup>:

$$\Delta G = G^{\text{II}} - G^{\text{I}} = (p_{\beta}^{\text{II}} - p_{\alpha}^{\text{II}})V_{\alpha}^{\text{II}} + \gamma A + (\mu_{\alpha}^{\text{II}} - \mu_{\beta}^{\text{II}})N_{\alpha}^{\text{II}} \quad (1.1)$$

where  $A$  is a term accounting for geometric factors related to volume or surface. Assuming a nucleus with a spherical shape with radius  $R$ , Eq. (1.1) can be rewritten as:

$$\Delta G = 4\pi R^2 \gamma + \frac{4}{3}\pi R^3 \rho_{\alpha} \Delta \mu \quad (1.2)$$

The critical radius that maximizes  $\Delta G$  is given by the derivative with respect to  $R$ :

$$R^* = \frac{2\gamma}{\rho_{\alpha} |\Delta \mu|} \rightarrow \Delta G^* = \frac{16\pi \gamma^3}{3\rho_{\alpha}^2 \Delta \mu^2} \quad (1.3)$$

Eq. (1.1) can be rewritten as function of the number of particles in the nucleus  $n = 4\pi R^3 \rho_{\alpha} / 3$ :

$$\Delta G = 4\pi \gamma \left( \frac{3n}{4\pi \rho_{\alpha}} \right)^{2/3} + n \Delta \mu \quad (1.4)$$

which gives a critical size

$$n^* = \frac{32\pi \gamma^3}{3\rho_{\alpha}^2 |\Delta \mu|^3} \quad (1.5)$$

The frequency of fluctuation scales with  $e^{(-\text{free energy cost}/kT)}$  and CNT predicts the nucleation rate to be proportional to  $e^{-\Delta G^*/kT}$ , where  $\Delta G^* = \Delta G(n^*)$  is the maximum of free energy of Eq. (1.2).

Although the success of CNT in the estimation of the nucleation rate, the theory suffers from inconsistencies [15]. It is only valid for not too large values of  $|\Delta \mu/kT|$ , otherwise, the assumption that the nucleus consists of bulk core plus interface does not hold. Furthermore, the basic form of the nuclei is not known, and therefore  $A$  remains a general geometric term and any shape can be in principle accommodated to it.

### 1.2.2 Landau Theory for Continuous Phase Transitions

Another free energy based theory devoted to the investigation of phase transitions in the solid state has been developed by L. D. Landau [16, 17] for displacive transformations. Later, the approach was extended to cover first-order transitions [18].

In the Landau approach, an order parameter  $\eta$  can be associated with a phase transition. This variable is supposed to contains all the information about the degree of order or extent of deformation in the parent phase.

The free energy can be Taylor-expanded into terms that couple  $\eta$  with other physical quantities (such as strain). The expansion is truncated at the lowest order and

---

<sup>1</sup> $p$ : pressure,  $V$ : volume,  $\gamma$ : surface free energy density,  $A$ : interface area,  $\mu$ : chemical potential,  $N$ : number of particles,  $\rho = N/V$ , I: pure  $\beta$  phase, II: coexistence regime  $\beta/\alpha$ .

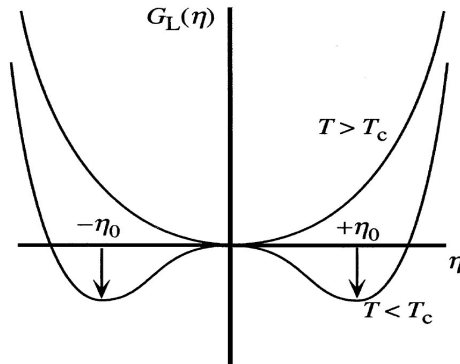


**Figure 1.2:** Plot of Landau free energy for temperatures above and below the transition temperature. The equilibrium value of the order parameter  $\eta$  is given by the minimum of the free energy. At high temperatures ( $T \geq T_c$ ) there is a single minimum at  $\eta = 0$ . At low temperatures ( $T \ll T_c$ ) the free energy has a maximum at  $\eta = 0$  and minima at non-zero values of  $\eta = \pm\eta_0$ .

the behavior of  $\eta$  and the coupled quantities can be obtained from the free energy using standard thermodynamic relations. It is in this sense that Landau theory has proven to be so powerful: a wide range of fundamental relationships can be derived, with coefficients that are usually obtained by fitting experimental data [19].

The pertinence of Landau theory relies on the appropriate definition of the order parameter. Once  $\eta$  is defined, the Landau free energy can be written as:

$$G(\eta) = G_0 + A\eta^2 + B\eta^4 + \dots \quad (1.6)$$

where  $A$  and  $B$  are constants, and  $G_0$  is the free energy of the system for  $\eta = 0$ . The shape of the Landau free energy changes as function of  $\eta$ , like it is displayed in Figure 1.2 for a temperature-induced phase transition.

For solid-solid phase transitions, the form of  $\eta$  reflects the symmetries of the system. In combination with representation theory [20], a precise form of  $\eta$  can be given based on group-subgroup relationships. The concept applies to second-order continuous transformations that can be successfully described. Accounting for first-order transitions, however, requires considering the general form of the Landau free energy including odd terms:

$$G(\eta) = G_0 + \alpha\eta + A\eta^2 + \beta\eta^3 + B\eta^4 + \dots \quad (1.7)$$

This causes the appearance of secondary minima that become the global minimum on lowering the the critical value of the coupling parameter, e. g., temperature. The order parameter discontinuously jumps from zero to a non-zero value, accounting for phase coexistence.

The mean-field character of Landau theory, that flattens local fluctuations into averages, and the unfulfilled condition on the vanishing of  $\eta$  at the critical point,

represent a major drawback in the study of first-order transformations. Although the remarkable success in the field of continuous transformations, nucleation and growth phenomena are not accounted for.

Attempts to tackle the difficult problem of the mechanism of first-order phase transitions have resulted into several modeling approaches. They can be organized as the following:

- **The common subgroup paradigm** offers a method to workaround the difficulty incurred by the absence of a direct group-subgroup relationship. Therein, a common subgroup is used to describe the space groups of the limiting structures. Lowering the symmetry of the transforming phases into a common cell enables for a mapping of atomic positions from one structure into the other. The transition is then described using the set of degrees of freedom allowed in the common subgroup. The choice of such group, which is not unique, determines the transformation path and as such represents a prejudice on the resulting mechanism. Particularly, nucleation phenomena are beyond the scope of such an approach. The approach developed by H. T. Stokes and D. M. Hatch [21] belongs to this class of methods.
- **The common lattice complex principle** relies on point configurations that may be generated within one type of Wyckoff set forming a lattice complex [22]. The transition may be described as a deformation of a homogeneous sphere packing with a given number of contacts per sphere. In a similar way to the subgroup paradigm, the deformation is achieved within a lattice complex which allows for lowering the number of contacts per sphere. Because of the continuous character of the mechanistic model obtained using this method, it suffers from the same limitations as the previous paradigm.
- **The adiabatic approximation** suggests the investigation of transformations using periodic least-enthalpy calculations [23, 24]. The method is based on the exploration of the adiabatic potential energy hypersurface of the transformation configuration space. The search for energetically favored intermediate states is performed assuming conservation of translational symmetry. To characterize the kinetics of the transition, activation volumes are determined and analyzed with respect to variations in pressure. However, the use of systems as small as unit cells and the resulting concerted mechanisms is not enough to capture phase coexistence and nucleation and growth processes.
- **The Free energy surface approaches** use advanced algorithms combined with molecular dynamics simulations perform efficient free energy scan. A recently developed method called *metadynamics* [25] uses the system box as a variable to monitor the evolution of the system bypassing the direct treatment of large number of single degrees of freedom. In order to avoid revisiting the same spot on the free energy surface or falling back to the same minimum, forces are recalculated at each step of metadynamics to create a history track of the simulation. Figure 1.3<sup>2</sup> illustrates the evolution of metadynamics run. The scan

---

<sup>2</sup>Figure taken from Ref. [25]

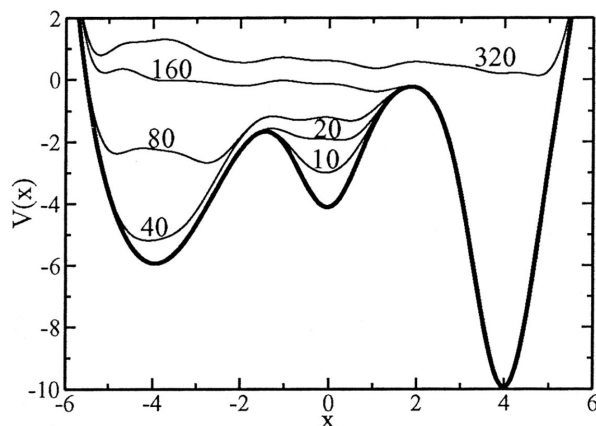


**Figure 1.3:** The dynamic evolution (thin lines) labeled by the number of dynamical iterations of free energy minima flooding using metadynamics method.

proceeds by flooding free energy minima until the surface is flat enough to cross over to another local minimum.

Jansen and Schön [26] developed a method based on scanning the free energy surface as a way to reconstruct the landscape surrounding a given minimum. Metastable configurations are derived as a function of coupling parameters depending on the system. The method is meant as guide for chemical synthesis.

Capturing the first-order character, either in the classification or the investigation of transitions, has been a long-standing challenge. The success of mean-field methods in the description of continuous transformations cannot be extended to the study of discontinuous transitions. Models featuring collective and concerted mapping of atomic positions are useful in relating structures before and after transition. However, the mechanistic details of nucleation and growth processes are beyond their scope. Additionally, the definition of a reaction coordinate that describes the transformation is not trivial because many relevant degrees of freedom are involved and usually unknown.

The progress achieved by free energy surface scanning methods helped to determine relevant traits of the energy landscape at the background of the transition. However, the visited local minima, although real, may not represent a necessary step along the transformation path. Moreover, the resulting mechanisms do not reflect a real time evolution of atomic displacements. Unlike in continuous diffusionless transformations, atomic motion in first-order transitions may exhibit very long diffusive paths that cannot be traced using free energy scanning approaches.

The appropriate approach to study first-order transformations should account for nucleation and growth processes without relying on a preconceived knowledge of mechanism or transition states. In this spirit, we use a methodology that combines three levels of modeling. The first is geometrical-topological for the derivation of first tran-

sition pathways. At the second level, molecular dynamics simulations are used to account for the time evolution of system along the transition. At last level, a Monte Carlo sampling of transition pathways is used to ensure convergence toward the real transformation mechanism. The combination of the two last steps is known as transition path sampling method (TPS). In the next chapter we shall describe in details the TPS simulation scheme.

---

# 2 Phase Transition Simulations

---

In this chapter, we review the theory and methodology of transition path sampling in details. We start with the definition of rare event in complex systems and problems thereof associated, then we provide a quick historical review of theoretical methods devoted to study of phase transitions considering their advantages and limitations. The core of this chapter is concerned with the description of different steps of the transition path sampling method and its adaptation and further development to study pressure-induced phase transitions in the solid state.

## 2.1 Rare Events in Complex Systems

Computer simulation methods, such as Molecular Dynamics (MD) use a numerical integration time step roughly in the order of 1 Femto second (fs) in order to capture properties of fast atomic motions like molecular oscillations. However, for example, timescales for small proteins folding are in the range of microseconds to milliseconds. Actually, even with the available sophisticated hardware we need about 100 seconds (s) of computer time to mimic 1 Pico second (ps) of reality. Therefore, to simulate a phenomenon that occurs once a millisecond we need over 3 years of computer time to observe it. This disparity of timescale is caused by the existence of high energy barriers or entropic bottlenecks separating long-lived states. These states, stable or metastable, can be either different chemical species like reactants and products of a chemical reaction, or different polymorphs or phases of a condensed material (e. g. B1 and B2 phases of NaCl), or even conformations of a polymer.

We mean by *rare event* every dynamical phenomenon occurring with a too low frequency to be observed on a computer simulation timescale. This definition includes many chemical and physical processes like protein folding, enzymatic reactions, chemical reactions in solution, crystal nucleation, and reconstructive pressure-induced phase transitions, the subject of this thesis.

To capture the timescale problem in activated processes, let's consider the situation depicted on Figure 2.1. A phase space of a prototypical system is made up of two basins *A* and *B* corresponding to distinct regions of long-lived states. The system will spend the majority of its time to *blindly* wander and switch between microstates forming the basin *A* before acquiring enough kinetic energy to climb over the energy

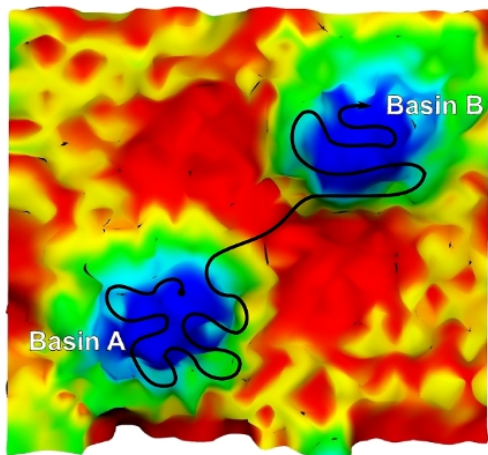


**Figure 2.1:** Schematic representation of a dynamical trajectory of a system crossing between two basins of long-lived states A and B (blue regions). The system spends the majority of the time wandering within basins A and B, while the crossing is fleeting. Colors: blue, green, yellow, and red reflect an ascending energy scale.

barrier and reach region  $B$ . For equilibrium statistics, only regions  $A$  and  $B$  are relevant. For  $A \rightarrow B$  dynamics, however, it's the buffer region separating  $A$  from  $B$  that has the most importance. Once the threshold is crossed, the system has a large kinetic energy compared to  $k_B T$ . The energy is transferred to different degrees of freedom causing a very fast relaxation into the second basin. Therein, the system starts again fluctuating within microstates forming the basin  $B$ .

Energy transfer between different degrees of freedom plays an important role in barrier crossing dynamics [27]. The periods of time spent within each basin,  $A$  and  $B$ , are different but distinctly longer than the time needed to cross over (Figure 2.2). This implies that transitions occur only rarely. For a condensed material, the bottlenecks are associated with phases nucleation. The hopping of an atom from one interstitial site to another in a solid is another physical example of a rare event. The nature of the bottleneck in this case depends upon the energy required to distort the local lattice structure and thereby opens possible pathways between interstitial sites.

Phase transitions investigations like they are performed in this work, consist in understanding the transition details by identifying:

- the transition mechanism, by the determination of atomic movements associated with phase nucleation and growth
- intermediate states, consequence of local deformations or the formation of low dimensional structures interfacing the coexistent phases
- kinetics of the transition (e. g. rate constants)

For this, it is necessary to identify the relevant degrees of freedom, or reaction



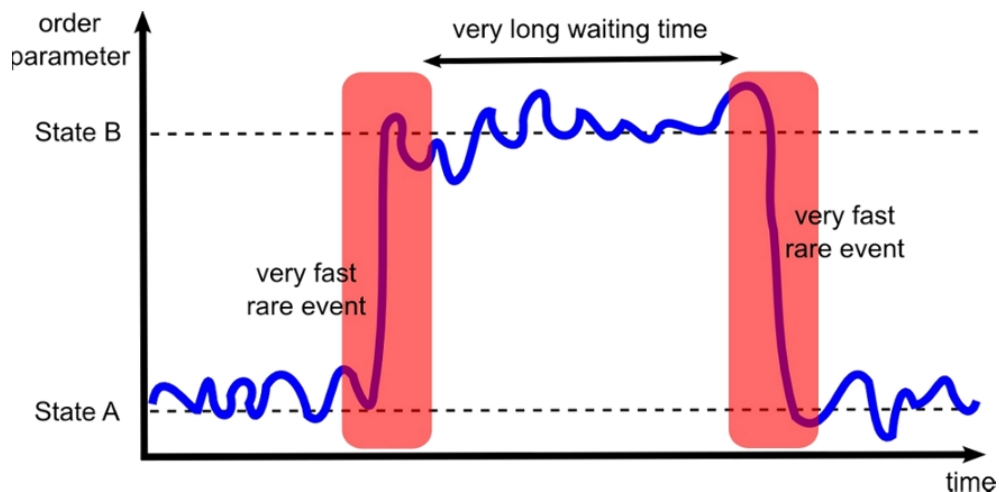


**Figure 2.2:** Time evolution of a dynamical trajectory of system crossing from state A to state B. Residence times spent in the states are very long compared to the time needed to switch between states. A and B can be distinguished using an order parameter like the coordination number of an atom.

coordinates, and distinguish them from orthogonal variables, whose fluctuations may be regarded as random noise.

The simplest approach to collect such kinetical informations and acquire an atomistic description of the dynamical process is the use of straightforward Molecular Dynamics. However, the very long waiting times consumed during the system fluctuation within stable basins may get exponentially aggravated if the height of energetic barriers increases. Even if we didn't try to probe the magnitude of such waiting periods, such calculations are far beyond the reach of current fastest computers. Obviously, in order to overcome the *rare event* problem, special methods are required. Therein, the focus is entirely set on the rare event, while skipping the tedious long waiting times.

## 2.2 Transition State Theory

Since we are interested in transitions between two stable states, a traditional way to tackle such problem is to search for dynamical bottlenecks the system passes through during the transition. Along this line, the classical transition state theory (TST) has been developed [28, 29].

The basic idea of TST is the assumption of a *dividing surface* in configuration space between stable states which are defined as adjacent sets separated by this surface. The validity of the method relies on the choice of such a surface. Crossings correspond to transitions and are only allowed once at a time. If the dynamics is reversible, each crossing point corresponding to a trajectory  $A \rightarrow B$ , should result into a trajectory

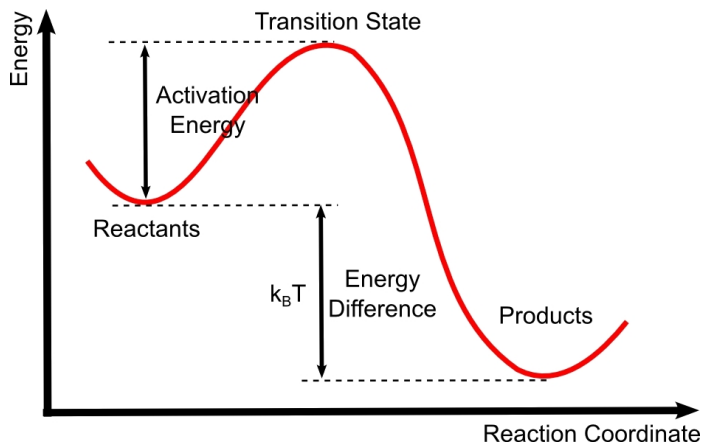


**Figure 2.3:** Schematic illustrating the crossover between two different states in the framework of the transition state theory.

$B \rightarrow A$  on reversing the momenta. Consequently, each point on the TST dividing surface has equal probability of ending in either  $A$  or  $B$ .

The dynamical information is retrieved from the free energy  $F$  as a function of a reaction coordinate that is supposed to describe the progress of the process.

If the dynamics of the system is dominated by energetic effects (as opposed to entropic effects), transition state surface can be identified using algorithms considering gradients of the potential energy surface (PES). Saddle points are then systematically determined by the enumeration of stationary points on the PES. Local minima exemplify attraction basins while saddle points indicates transition states. Different minima can be accessed from saddle points via small fluctuations [30,31].

If the location of the surface is known, one may construct a scheme where the system is first moved reversibly to the transition state surface. Many fleeting trajectories are then initiated. The first step consists in determining the reversible work and thus the probability of reaching the transition state surface. In the second, however, one can use the set of subsequent trajectories to determine the probability to successfully cross the threshold. These two steps give the rare event rate constant [32] that can be directly compared to experimental observables. To complete the transition picture, the mechanism is inferred by comparing stable states to the transition states.

This approach was pioneered by Anderson [33], Bennett [34], and Chandler [35]. Since then, TST was employed and systematically improved in order to get the best approximation of the dynamical process statistics. The theory served as a development background for many other methods that can be listed as follows:

### 2.2.1 Open-end Methods

Instead of trying to describe the crossing between two stable states, the focus of this category of methods is set on how to live the initial state  $A$  without making any as-

sumption on the final state  $B$ . This can be realized by, for instance, introducing energy into the system to escape the basin of the minimum in which the system is initially prepared. This idea is at the basis of conformational flooding [36], the Laio-Parrinello method [37, 38], and the enhanced sampling of a given reaction coordinate [39].

Another strategy consists in exploring the full potential energy surface through all its minima and saddle points like in the activation-relaxation technique [40], the dimer method [41], the kinetic Monte Carlo (MC) approach [42–44], and the discrete path sampling of Wales [45].

Finally, a different flavor of procedures consists in artificially enhancing the frequency of the rare event in a controlled way like in the hyperdynamics approach developed by Voter *et al.* [46, 47]. The procedure is based on lowering the energy between the saddle point and the initial minimum. Temperature accelerated dynamics is another method that increases the frequency of an event on raising temperature [48]. It is also possible to extend the molecular simulation timescale scope by the use of parallel processing as in the parallel replica method [49]. Therein, several simulations are performed in parallel in different thermodynamic states, e. g., at different temperatures. While systems with sufficiently high-temperature pass over the potential bottlenecks, those with low-temperature mainly probe the local free energy minima. A stepwise system swap is used to reproduce the transition event.

### 2.2.2 Two-end Methods

This class of methods usually requires an initial path to start the procedure. Paths created by one of the open-end methods can be used. Sometimes, simple interpolation schemes are helpful to devise a first path by creating a discretized chain of configurations linking  $A$  to  $B$ .

On the potential energy surface, transition pathways can be defined as minimum energy paths (MEP). The dividing surface is taken to be the hyperplane going through the saddle point with a normal given by the displacement vector of the unstable mode of the relevant saddle [50]. The concept of minimal energy path was used in the Nudged Elastic Band method [51] as well in the zero-temperature string method [52].

Another way to study the rare event problem is based on the minimization of a suitably defined discretized action [53], or to use modified stochastic equations of motion to drive the system from  $A$  to  $B$  [54, 55]. We finish our list with the topological method of Tănase-Nicola and Kurchan in which the use of transition path sampling in combination with saddle point searching vector walkers was suggested [56].

### 2.2.3 Limitations

We pointed out in the description of the rare-event problem that the study of transitions aims at the elucidation of the transition mechanism including the identification of relevant transition states. The validity of TST and the methods mentioned above mainly relies in the first step; that is the choice of a reaction coordinate. In other terms, the *a priori* knowledge of the true transition path is required. One can count on the guidance of chemical or physical intuition to guess which degree of freedom may be the most relevant. Unfortunately, in complex systems such a choice is far from

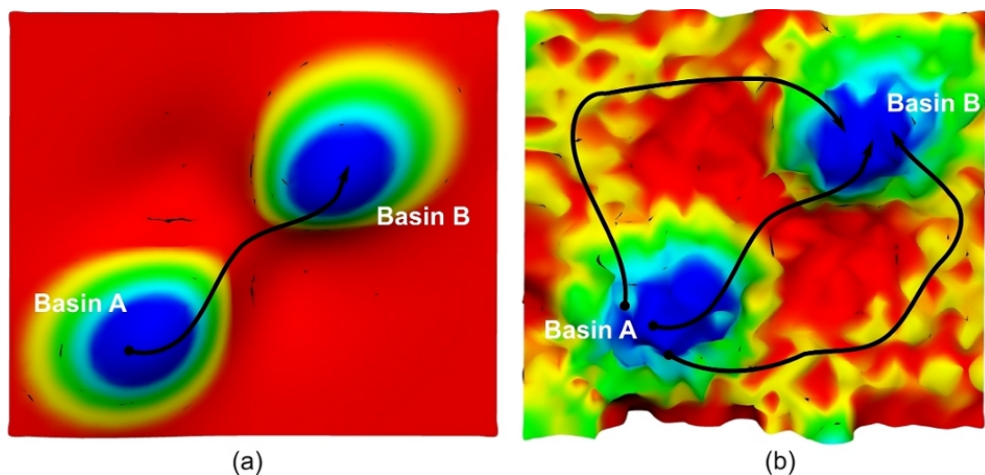


**Figure 2.4:** Schematic illustration of two types of potential energy surface topologies as controlled by (a) energetic effects (2<sup>nd</sup> order phase transitions) and (b) entropic effects (1<sup>st</sup> order phase transitions). Color scale distinguishes between low energy (blue) and high energy (red) regions.

trivial. Actually, even if the reaction coordinate looks fine, some important aspects of the transition may have been disregarded. The kinetic information may be obtained using one of the methods listed above. However, the mechanistic picture may still be strongly biased by the *a priori* choice of the reaction coordinate. Consequently, if the selected degrees of freedom do not capture the essence of the mechanism under study, such biasing schemes are doomed to failure.

An method is thus needed to accurately determine the reaction coordinate to use, or a theory that simply does not rely on a reaction coordinate to study the rare event. Along this line, a different method, transition path sampling, has been developed and successfully applied to study rare event in different complex systems.

## 2.3 Transition Path Sampling

In the last section, it was shown that transition state theory and its modern variants can be very successful in simple and small systems with smooth topography of potential energy landscapes (Figure 2.4, left panel). The efficiency of such methods relies on the correctness of the choice of reaction coordinate which describes the progress of the process. For numerous problems, reaction coordinates are not known and very difficult to anticipate.

The situation is further complicated because the energy surface can exhibit a large number of local minima, maxima and saddle points. In this case, saddle points cease to be characteristic points of the free energy barrier.

For small systems involving a few atoms, transition states can be numerically

located using algorithms that systematically search for saddle points in PES. For higher-dimensional systems, however, PES contains many saddle points as illustrated in Figure 2.4 [right panel]. The explicit enumeration of saddle points in PES (configuration space) can be done for system of ten or fewer atoms. However, one can by no means distinguish those which are dynamically relevant for the transition process. For systems containing large number of atoms, PES topologies are rough on the scale of thermal energies,  $k_B T$ , and dense in saddle points. Therefore, there is generally an uncountable number of transition states. The accurate determination of relevant points is not possible. Instead, one wants to locate and sample an ensemble of transition states. Transition path sampling accomplishes this task [32, 57–60].

### 2.3.1 Importance Sampling of Trajectory Space

The basic idea of TPS is a generalization of standard Monte Carlo procedures [61, 62]. The focus is set on the chains of states (dynamical trajectory) rather than on individual states [63].

In standard procedures, Monte Carlo calculations perform a random walk in configuration space. In order to ensure that the most important regions of this space are adequately sampled, the walk is biased such that a configuration  $x$  is visited in proportion to its probability  $p(x)$ . The walk can be initiated from different configurations including atypical ones, i. e. with low probability  $p(x)$ . After equilibration moves, the bias drives the system to the most relevant regions of configuration space. This important feature for the success of the Monte Carlo Sampling is called *Importance Sampling*, and can be generalized to trajectory space as well.

In an ergodic system<sup>1</sup>, every possible trajectory that connects  $A$  to  $B$  in a given time  $t$  occurs with a unique probability. This property can be used to construct a distribution functional for dynamical paths, upon which the statistical mechanics of trajectories is based. Such a functional can be helpful in the construction of partition functions for ensembles of trajectories satisfying given constraints.

This change in perspective allows for a direct access to a set of markedly different pathways that may be relevant for the process. Such a set of reactive trajectories is termed the *transition pathway ensemble*. The identification of this ensemble does not require prior knowledge of the transition mechanism or reaction coordinates. Rather than requiring such information as an input, transition path sampling can help in finding it.

Since the pathways collected by TPS are fully dynamical trajectories, it is possible to extract kinetic information from sampling simulations. The first step in the application of the TPS consists in the definition of an appropriate path ensemble. A set which contains reactive paths that begin in a particular stable state,  $A$ , and end in a different stable state  $B$ .

In the next sections, two main ideas are discussed:

- the theoretical basis of the transition path sampling, namely the statistical

---

<sup>1</sup>If the ensemble average of a dynamical system is obtained by time averaging, it is called ergodic. In other word, we can study the average behavior of a many-particle system simply by computing the natural time evolution of that system numerically and averaging the quantity of interest over a sufficiently long time.

mechanics of trajectories

- the efficient sampling and analysis of reactive trajectories

Applications of the method to the investigation of pressure induced phase transformations in the solid state are presented and discussed in next chapters. Different aspects of the simulation procedure are explained by application to real examples. New perspectives are introduced by widening the scope of the main TPS methodology to include chemical substitution.

### 2.3.2 Defining the Transition Path Ensemble

#### Defining the Initial and Final Regions

While transition path sampling does not require *a priori* knowledge of the transition mechanism (no reaction coordinate), it is mandatory that the initial and final regions are correctly characterized. An easy-to-use way is the consideration of a low dimensional *order parameter*  $q$ . The identification of an order parameter that truly discriminates between  $A$  and  $B$  is sometimes not trivial.

A successful order parameter must fulfill a two criteria:

- it should be able to tolerate typical equilibrium fluctuations within basins of attraction. Otherwise, many important transition pathways might be missing in the transition path ensemble.
- region  $A$  and  $B$  (spanned by  $h_A$  and  $h_B$ , respectively) should not extend off basins of corresponding basins of attraction (no overlap between  $A$  and  $B$ ). Otherwise, the transition path sampling would wrongly collect  $A \rightarrow A$  and  $B \rightarrow B$  as reactive pathways.

#### Dynamical Path Probability

While in principle the time evolution of the system is continuous, it is more convenient to discretize the time evolution of the system and view a trajectory of length  $T$  as an ordered sequence of states:

$$x(T) \equiv \{x_0, x_{\Delta t}, x_{2\Delta t}, \dots, x_T\}. \quad (2.1)$$

Consecutive states or time slices are separated by a small time increment  $\Delta t$  and  $x_{i\Delta t}$  is a complete snapshot of the system at time  $i\Delta t$ . Therefore, the representation of the trajectory consists of  $L = T/\Delta t + 1$  states. For a molecular system evolving according to Newton's equations of motion, each state  $x \equiv \{r, p\}$  consists of positions  $r$  and momenta  $p$  of all particles.

The statistical weight,  $P[x(T)]$  indicates the probability to observe a given path  $x(T)$ . It depends on the probability of its initial conditions and on the specific propagation rules describing the time evolution of the system. If the process is Markovian, i. e. the probability to move from  $x_t$  to  $x_{t+\Delta t}$  after one time step  $\Delta t$  depends only

on  $x_t$  and not on the history of the system prior to  $t$ , the total path probability can be written as the product of single time step transition probabilities  $p(x_t \rightarrow x_{t+\Delta t})$ ,

$$P[x(T)] = \rho(x_0) \prod_{i=0}^{T/\Delta t - 1} p(x_{i\Delta t} \rightarrow x_{(i+1)\Delta t}). \quad (2.2)$$

The first factor on the right hand side of the above equation,  $\rho(x_0)$ , is the probability distribution of the initial conditions. These distribution can be defined according to the ensemble of the system to study. It depends on atomic positions and momenta and other conditions of temperature and pressure.

### Reactive Path Probability

We restrict our interest to reactive pathways connecting  $A$  to  $B$ , i. e. trajectories starting at time zero in region  $A$  and ending in region  $B$  at time  $T$ ,

$$P_{AB}[x(T)] \equiv h_A(x_0)P[x(T)]h_B(x_T). \quad (2.3)$$

Here,  $h_A(x)$  and  $h_B(x)$  are characteristic population functions of regions  $A$  and  $B$ , respectively. These functions are used to decide whether a given state  $x$  is inside  $A$  (or  $B$ ) or off basins:

$$h_{A,B}(x) = \begin{cases} 1 & \text{if } x \in A, B \\ 0 & \text{if } x \notin A, B \end{cases} \quad (2.4)$$

Due to the restriction applied to the pathways in the transition path probability (Eq. (2.3)), a non-reactive path (not beginning in  $A$  or not ending in  $B$ ) has a statistical weight of zero. A path connecting  $A$  to  $B$ , however, has a non-zero weight that depends on the unrestricted path probability  $P[x(T)]$ . The transition path ensemble is, hence, a selection of reactive trajectories from the ensemble of all possible pathways without changing trajectories relative probabilities.

The transition path ensemble, weighted and filtered via the probability functional in Eq. (2.3), is a set of true dynamical trajectories free of any bias by unphysical forces or constraints. The sampling of such pathways yields informations about the mechanism and the transition kinetics. The definition of this ensemble is very general and valid for all Markovian processes<sup>2</sup>, and can be applied for different types of dynamics (deterministic, stochastic, Brownian, etc ...).

### Deterministic Dynamics

We assume that the time evolution of the system can be described by a set of ordinary homogeneous differential equations

$$\dot{x} = \Gamma(x) \quad (2.5)$$

---

<sup>2</sup>One for which the likelihood of a given future state, at any given moment, depends only on its present state, and not on any past states. This memorylessness property is required for sampling ergodic systems.

Since the time evolution of the system is deterministic, the state of the system  $x_t$  at time  $t$  is completely determined by the state  $x_0$  at time 0,

$$x_t = \phi_t(x_0). \quad (2.6)$$

The time dependent function  $\phi_t(x_0)$  is the propagator of the system. In the standard Hamiltonian picture, Eq. (2.5) is derived from a Hamiltonian  $H(x) = H(r,p)$  according to  $\Gamma(r,p) = \{\partial H/\partial p, -\partial H/\partial r\}$ . For such deterministic dynamics the short time transition probability can be expressed as a Dirac delta function:

$$p(x_t \rightarrow x_{t+\Delta t}) = \delta[x_{t+\Delta t} - \phi_{\Delta t}(x_t)]. \quad (2.7)$$

This gives the probability of being in  $x_{t+\Delta t}$  at time  $t + \Delta t$  provided that you were in  $x_t$  at time  $t$ .

Accordingly, the path probability is given as follows,

$$P_{AB}[x(T)] = \rho(x_0)h_A(x_0) \prod_{i=0}^{T/\Delta t-1} \delta[x_{(i+1)\Delta t} - \phi_{\Delta t}(x_{i\Delta t})]h_B(x_T) \quad (2.8)$$

The definitions mentioned above apply for different dynamics, such as extended Lagrangian dynamics of Car and Parrinello [64], and in different ensembles [61].

### 2.3.3 Sampling the Transition Path Ensemble

#### Monte Carlo in Path Space

In analogy with standard Monte Carlo techniques, transition path sampling is an importance sampling of trajectories akin to the importance sampling of configurations.

The random walk in the trajectory space is biased such that each pathway is visited in proportion to its weight in the transition path ensemble. The focus is entirely set on reactive pathways by excluding zero weight trajectories, i. e. those not exhibiting the transition.

The methodology of sampling transition pathways in trajectory space is similar to probability distribution sampling in Monte Carlo procedures [65]. The random walk in trajectory space is accomplished in two main steps:

- starting from a trajectory  $x^{(o)}(T)$  ("o" stands for "old") with a weight  $P_{AB}[x^{(o)}(T)] \neq 0$ , a new trajectory  $x^{(n)}(T)$  is generated. This step is termed *trial move*.
- the newly generated path is accepted with an acceptance probability balanced by the frequency of the reverse move. This step is termed *detailed balance*.

The detailed balance condition implies the following:

$$P_{AB}[x^{(o)}(T)]\pi[x^{(o)}(T) \rightarrow x^{(n)}(T)] = P_{AB}[x^{(n)}(T)]\pi[x^{(n)}(T) \rightarrow x^{(o)}(T)] \quad (2.9)$$

where,  $\pi[x(T) \rightarrow x'(T)]$  is the probability to move from the old to the new path. It is expressed as product of generation probability  $P_{gen}$  and acceptance probability  $P_{acc}$ :

$$\pi[x(T) \rightarrow x'(T)] = P_{gen}[x(T) \rightarrow x'(T)] \times P_{acc}[x(T) \rightarrow x'(T)]. \quad (2.10)$$



From (2.9) the following condition is obtained:

$$\frac{P_{acc}[x^{(o)}(T) \rightarrow x^{(n)}(T)]}{P_{acc}[x^{(n)}(T) \rightarrow x^{(o)}(T)]} = \frac{P_{AB}[x^{(n)}(T)]P_{gen}[x^{(n)}(T) \rightarrow x^{(o)}(T)]}{P_{AB}[x^{(o)}(T)]P_{gen}[x^{(o)}(T) \rightarrow x^{(n)}(T)]}. \quad (2.11)$$

To satisfy this condition and considering that  $P_{acc}[x^{(o)}(T) \rightarrow x^{(n)}(T)]$  cannot exceed 1, we can use the Metropolis rule [66]:

$$P_{acc}[x^{(o)}(T) \rightarrow x^{(n)}(T)] = \min \left[ 1, \frac{P_{AB}[x^{(n)}(T)]P_{gen}[x^{(n)}(T) \rightarrow x^{(o)}(T)]}{P_{AB}[x^{(o)}(T)]P_{gen}[x^{(o)}(T) \rightarrow x^{(n)}(T)]} \right]. \quad (2.12)$$

Since the old trajectory  $x^{(o)}$  is reactive, i. e.  $h_A[x_0^{(o)}] = 1$  and  $h_B[x_T^{(o)}] = 1$ , the acceptance probability can be written as:

$$P_{acc}[x^{(o)}(T) \rightarrow x^{(n)}(T)] = h_A[x_0^{(n)}]h_B[x_T^{(n)}] \times \min \left[ 1, \frac{P[x^{(n)}(T)]}{P[x^{(o)}(T)]} \frac{P_{gen}[x^{(n)}(T) \rightarrow x^{(o)}(T)]}{P_{gen}[x^{(o)}(T) \rightarrow x^{(n)}(T)]} \right], \quad (2.13)$$

Accordingly, only trajectories that connect  $A$  to  $B$  are accepted.

So far, we have described TPS as a realization of two processes. The core process is the system dynamics, that takes place in the phase space  $x$  of the system. The outer process is the path sampling that is built as a Markov process (Section 2.3.2) in the transition path space  $x(T)$ . We move now on to see how this Monte Carlo random walk in path space is realized in practice.

### Shooting Moves for Deterministic Dynamics

The crucial step TPS is the generation of new trajectories starting from an existing one. While many schemes can be considered [67], the shooting algorithm is practically the most efficient method.

In a shooting move, we randomly select a phase space point  $x_{t'}^{(o)}$  along an existing (old) pathway,  $x^{(o)}(T)$ . This single state can be modified by slightly changing the atomic momenta. From the yielding state  $x^{(n)}(T)$ , two trajectory segments are *shot off* in both directions of time ( $+t$  and  $-t$ ), forward to time  $T$  and backward to time 0. Together, these two segments form the new pathway as represented in Figure 2.5a. The corresponding generation probabilities are:

$$P_{gen}^f[x^{(o)}(T) \rightarrow x^{(n)}(T)] = \prod_{i=t'/\Delta t}^{T/\Delta t-1} p \left( x_{i\Delta t}^{(n)} \rightarrow x_{(i+1)\Delta t}^{(n)} \right) \quad (2.14)$$

$$P_{gen}^b[x^{(o)}(T) \rightarrow x^{(n)}(T)] = \prod_{i=1}^{t'/\Delta t} \bar{p} \left( x_{i\Delta t}^{(n)} \rightarrow x_{(i-1)\Delta t}^{(n)} \right). \quad (2.15)$$

Eq (2.14) represents the dynamical path weight for the forward trajectory. The generation probability of the backward segment of trajectory is expressed using the

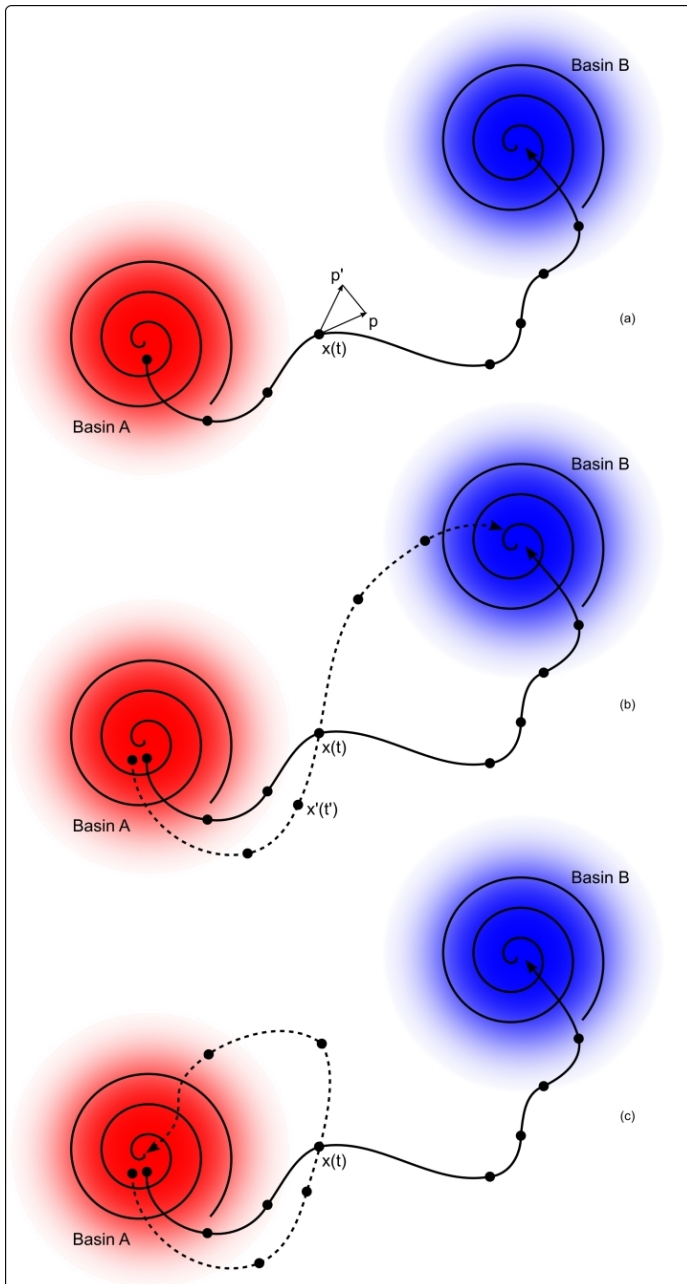


**Figure 2.5:** Schematic illustrating (a) a shooting move and (b) a shifting move, two essential steps in the transition path sampling method. (a) The atomic momenta of randomly chosen time slice  $x(t)$  from an existing trajectory are slightly modified (a). (b) Propagating the modified state forward and backward in time is accepted if transition is observed. Otherwise (c) the failed trajectory is rejected.

the inverted probability  $\bar{p}(x \rightarrow x')$ . The generation probability of the new trajectory is the combination of (1) the probability to obtain the modified state, or the *shooting point*  $x_{t'}^{(n)}$  and (2) the generation probabilities of the forward and backward segments of the new trajectory:

$$P_{gen}[x^{(o)}(T) \rightarrow x^{(n)}(T)] = p_{gen}[x_{t'}^{(o)}] \prod_{i=t'/\Delta t}^{T/\Delta t-1} p\left(x_{i\Delta t}^{(n)} \rightarrow x_{(i+1)\Delta t}^{(n)}\right) \times \prod_{i=1}^{t'/\Delta t} \bar{p}\left(x_{i\Delta t}^{(n)} \rightarrow x_{(i-1)\Delta t}^{(n)}\right) \quad (2.16)$$

This formula is a general expression of the shooting algorithm. In order to simplify it we make two assumptions and focus more on deterministic dynamics: microscopic reversibility ( $\bar{p}(x \rightarrow y) = p(\bar{x} \rightarrow \bar{y})$ )<sup>3</sup> and symmetric slice modification ( $p_{gen}(x_t^{(o)} \rightarrow x_t^{(n)}) = p_{gen}(x_t^{(n)} \rightarrow x_t^{(o)})$ ). If the stationary distribution of the modified state includes conserved quantities such as total linear and angular momentum, a consistent generating algorithm reduces further the acceptance rule into

$$P_{acc}[x^{(o)}(T) \rightarrow x^{(n)}(T)] = h_A[x_0^{(n)}]h_B[x_T^{(n)}] \quad (2.17)$$

The simplicity of the acceptance probability in Eq. (2.17) entails an algorithmic simplicity for shooting moves. The evaluation of  $P_{acc}$  requires the calculation of relative weights of old and new phase space points and the determination whether the new pathway begins in  $A$  and ends in  $B$ . The acceptance criterion in Eq. (2.17) holds even when the dynamics is non Hamiltonian.

The construction of a symmetrical algorithm that modifies a state  $x_{t'}^{(o)}$  into  $x_{t'}^{(n)}$  deserves a particular attention. The modification has to be consistent with the initial conditions distribution  $\rho(x)$ , that might contain additional constraints. In the case of linear constraints, such as total momentum and angular momentum, we can construct the following algorithm. In this procedure we assume that only momenta are changed. We consider the space point  $x_{t'}^{(o)} = \{r_{t'}^{(o)}, p_{t'}^{(o)}, \xi_{t'}^{(o)}\}$ , where  $\xi_{t'}^{(o)}$  represents additional variables of generalized dynamics,

1. Randomly select a time slice  $x_{t'}^{(o)}$  from an existing path  $x^{(o)}(T)$
2. Modify the selected time slice momenta by adding a random displacement  $\delta p$  from a one dimensional Gaussian distribution according to  $p' = p_{t'}^{(o)} + \delta p$ . The random displacement must be symmetric with respect to reverse move
3. Impose linear constraints such as vanishing total linear and angular momentum
4. Accept the new shooting point with probability  $\min[1, \rho(x_{t'}^{(n)})/\rho(x_{t'}^{(o)})]$ . If rejected, restart from 2

---

<sup>3</sup> $\bar{x}$  denotes the transformation of  $x$  under time-reversal. If  $x = \{r, p\}$ , then  $\bar{x} = \{r, -p\}$ . Not all integration schemes have a simple way to reverse the time evolution of the system, such as simply inverting the momenta. For this reason, Verlet derived algorithms are definitively preferable.

5. If accepted, rescale the momenta in order to obtain the desired total energy
6. Integrate backward and forward in time
7. If the path is reactive (starts from  $A$  and ends in  $B$ ) accept and the new trajectory is used, otherwise reject and restart from 1

The shooting algorithm is a server of new trajectories for the random walk in trajectory space. The serving is achieved through perturbation of an old path. The magnitude of phase space displacement  $\delta x$ ,  $\delta p$  in our case, affects the acceptance of the move. If  $\delta x \rightarrow 0$ , the old path is simply reproduced with an acceptance equal to 1. Very low displacements lead to the sampling of the same path as well, and the harvested pathways are correlated. If  $\delta x \rightarrow 0$  is very large, however, the collected pathways are different but the acceptance rate will be very low because of the instability of reactive trajectories  $A \rightarrow B$ . We mean by unstable the easiness to generate  $A \rightarrow A$  and  $B \rightarrow B$  trajectories. The production of decorrelated trajectories using as less as possible Monte Carlo cycles is at the aim of any efficient sampling algorithm. An acceptance of 40 – 60% indicates an efficient sampling [68].

### Shifting Moves for Deterministic Dynamics

The collected trajectories during TPS start in  $A$  and end in  $B$ . The ending parts can be shifted forward and backward in time using the propagation rules of the dynamics. Growing and deleting parts of the trajectory inside stable basins keep the path reactive (Figure 2.5). This *reptile* translation is the basis of the second part of TPS algorithm. In this case the generation of acceptance rules is realized by considering the dynamical weight of the newly created segments of the path. The generation probabilities for forward and backward shift can be written:

$$P_{gen}^f[x^{(o)}(T) \rightarrow x^{(n)}(T)] = \prod_{i=(T-\delta t)/\Delta t}^{T/\Delta t-1} p(x_{i\Delta t}^{(n)} \rightarrow x_{(i+1)\Delta t}^{(n)}) \quad (2.18a)$$

$$P_{gen}^b[x^{(o)}(T) \rightarrow x^{(n)}(T)] = \prod_{i=1}^{\delta T/\Delta t} \bar{p}(x_{i\Delta t}^{(n)} \rightarrow x_{(i-1)\Delta t}^{(n)}) \quad (2.18b)$$

From the detailed balance in Eq. (2.9) the criteria of acceptance can be written as:

$$P_{acc}^f[x^{(o)}(T) \rightarrow x^{(n)}(T)] = h_A[x_0^{(n)}]h_B[x_T^{(n)}] \quad (2.19a)$$

$$P_{acc}^b[x^{(n)}(T) \rightarrow x^{(o)}(T)] = h_A[x_0^{(o)}]h_B[x_T^{(o)}] \quad (2.19b)$$

From this, the shifting move is accepted or refused according to the reactivity of the trial path  $x^{(n)}(T)$ . The average acceptance probability can be controlled by changing the magnitude of the time interval.

Shifting moves contribute to the improvement of the sampling of the transition ensemble [59]. In practice, they can be performed without cost for deterministic dynamics because the time evolution of new trajectory segments is already known and

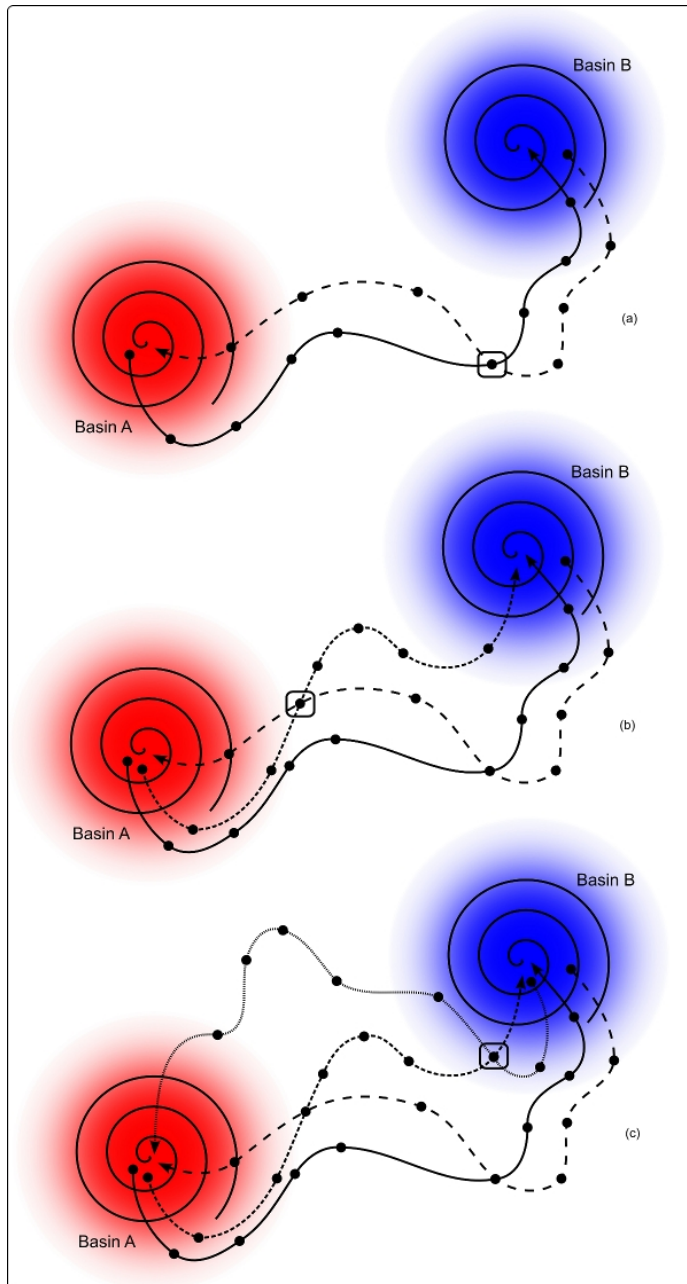


**Figure 2.6:** Transition path sampling iterations at work: (a) a state (black square) is randomly chosen from an existing  $A \rightarrow B$  trajectory and a new trajectory is shot off in direction of  $A$ . If successful, trajectory is retained, and another shooting point is chosen from it. (b)-(c) The shooting step is repeated in both directions,  $A \rightarrow B$  and  $B \rightarrow A$ , shifting both limits of the shooting window until trajectory decorrelation is achieved.

stored. However, such moves are not ergodic and do not change trajectory parts of interest, i.e. transition region. Therefore, shifting moves alone do not offer an ergodic sampling of trajectory space and should be used in combination with shooting moves.

### Generating an Initial Path

TPS requires the generation of an initial path already belonging to the transition path ensemble. Its weight can be very low but not zero. However, the rarity of the transition phenomenon makes the production of such a trajectory from an MD run unlikely to succeed. An artificial modeling of the initial trajectory represent a useful strategy. In this case, the use of interpolation schemes between the limiting stable states is possible. Doing so, one can have a good approximation for a transition state that can be used for shooting moves forward and backward in time in order to end in both  $A$  and  $B$ . Another option consists in the use of enhanced MD simulation. The use of very high-temperature or very high-pressure (compared to the experimental conditions) can enhance the phenomenon frequency. In this case, the system is systematically cooled, or the pressure is slowly released, in order to equilibrate the initial regime for TPS.

It is also possible to play with the concept of the reaction coordinate that drives the system from  $A$  into  $B$ . Many points can be generated forming a chain of states that can be used as shooting points. However, there is no general recipe to create a first path [67]. Rather, custom schemes must be developed for this purpose considering the nature of the transition and the system involved.

## 2.4 Methodology Development

So far, transition path sampling was introduced as a computational methodology based on statistical mechanics of trajectories. A combination of two different walks. One in configuration space, for growing pathways according to system dynamics, and the other in path space, for harvesting the reactive ones (Figure 2.7).

The Monte Carlo random walk is biased to ensure that the most important regions of trajectory space are adequately sampled. For this, a probability, or weight, is assigned to every pathway. This probability is a statistical description of all possible reactive trajectories, the transition path ensemble. The ensemble sampling is biased by path weight to converge to the most favorable transition regime. The analysis of the harvested trajectories yields detailed mechanistic informations on the transition mechanism.

Because of the Markovian nature of the Monte Carlo walk in the path space, TPS iterations can be started from different initial pathways. The sampling implements a two-step process, shooting and shifting. Small perturbations are added to the atomic momenta of a randomly chosen configuration from an existing reactive path. The perturbed state is shot off forward and backward in time to create a new path. Due to the chaoticity of the equations of motion, the new trajectory quickly diverges from the old one leading to rapid progress in the random walk through path space and, hence, to efficient sampling.

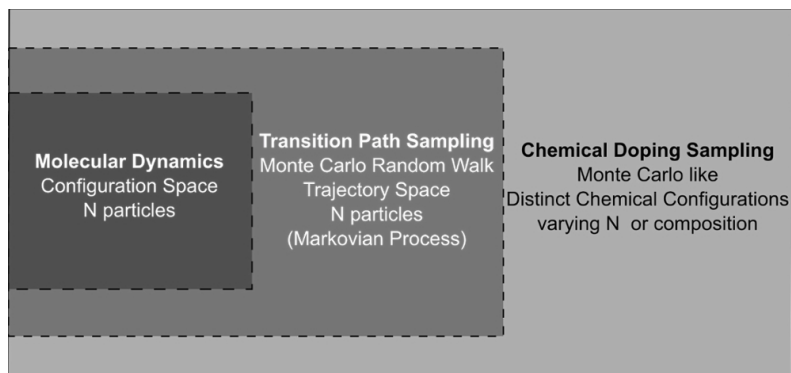


**Figure 2.7:** Different simulation levels of the chemical doping procedure. The core simulation (Inner layer) describes the time evolution of the system in configuration space to produce dynamical trajectories. The latter are sampled by (Monte Carlo) random walk in trajectory space (Middle layer). Chemical composition of the system is systematically modified using a stepwise Monte Carlo procedure (outer layer). Doping moves are separated by intervals of TPS iterations to relax the modified system to its favorable transition regime.

Depending on system dynamics, deterministic or stochastic, the perturbation applied to the system can be realized by changing atomic momenta or by shifting some atomic positions. This move is legitimate in both configuration and trajectory spaces as long as dynamics constraints are respected, e. g, conserved linear and angular total momenta. This premise can be used to incorporate defects or dopants as an additional perturbation to a system undergoing a phase transition.

On the top of TPS iterations, a Monte Carlo procedure is added to create sets of sampling of chemically different systems (Figure 2.7). Atoms are randomly removed or substituted. Then, the modified configuration is propagated forward and backward in time. The move is only accepted if the new path is reactive (connects  $A$  to  $B$ ).

Acceptance of a shooting move is biased by reactivity and weight of the generated trajectory. Because such a move does not ensure the generation of a high-weight path, the modified system is immediately submitted to TPS iterations. Therein, pathways are sampled and most probable transition regime obtained.

The procedure is described as a stepwise walk through different compositions of a gradually modified system. The walk is biased to only visit favorable transition regimes.

The practice of chemical doping and vacancies incorporation to transition simulations is discussed in details in the next section.

### 2.4.1 Chemical Substitution and Defects Incorporation

Let us consider a binary system  $AB$  undergoing a phase transition  $\alpha \rightarrow \beta$ . The simulation box counts  $N$  particles ( $N = N_A + N_B$ ). We are interested in studying the mixed system  $AB_{1-x}C_x$  starting from the pure phase  $AB$  where  $N_C$  is initially equal

to zero. The only prerequisite is a trajectory connecting  $\alpha$  to  $\beta$ . We acquire it from a transition path sampling simulation, i. e. decorrelated from initial path mechanism and converged to the most probable regime.

The different steps of the procedure are shown on Figure 2.8 and more details are given in the following:

1. Choose a time slice  $x(t)$  from an existing trajectory connecting phase  $\alpha$  to phase  $\beta$  for a system with  $N_{total}$  particles ( $N_{total} = N_A + N_B + N_C$ )
2. Select an atom  $i$  of type B randomly and replace it by one atom type C
3. Calculate the change in energy  $\Delta E$ 
  - (a) If  $\Delta E < 0$ , accept the modified configuration  $x'(t)$
  - (b) If  $\Delta E > 0$ , select a random number R within  $[0,1]$ ,
    - i. If  $\exp -\frac{\Delta E}{K_B T} < R$ , the modified configuration  $x'(t)$  is accepted
    - ii. If  $\exp -\frac{\Delta E}{K_B T} > R$ , go to step 2 and start again
4. Rescale to the desired temperature and rescale the atomic momenta to keep the energy and angular momentum conserved
5. Propagate the new configuration  $x'(t)$  in both directions of time ( $-t, +t$ ) using the MD integrator
  - (a) If the  $\alpha \rightarrow \beta$  transition is observed, keep the new trajectory for the next path sampling
  - (b) If the  $\alpha \rightarrow \beta$  transition is *not* observed, go to step 2 and start again
6. The new trajectory of the chemical composition  $N_{total} = N_A + N'_B + N'_C$  ( $N'_B = N_B - 1$  and  $N'_C = N_C + 1$ ) is used to start a new path sampling iterations

The overall procedure is a chain of TPS simulations linked via chemical substitution steps in the form: TPS( $N_p$ T)  $\rightarrow$  Chem. Substit.  $\rightarrow$  TPS( $N'$ pT)  $\rightarrow$  Chem. Substit.  $\rightarrow$  TPS( $N''$ pT)  $\rightarrow$  Chem. Substit.  $\rightarrow$  TPS( $N'''$ pT)  $\rightarrow$  ...

Separating substitution steps with TPS iterations is mandatory. The modified system is equilibrated and the effect of the perturbation caused by doping is propagated. Before next substitution step is performed, the trajectory ensemble of the modified system is converged to the favorable transition regime. Converging trajectory regime of the perturbed system before the next change in chemical composition. The modified system is converged path sampling of modified systems before proceeding with the next shooting on chemical composition to the real mechanism of the corresponding new chemical composition.

The substitution can be done one atom at once, or many sites can be replaced simultaneously. However, systematically introducing atoms, one-by-one, keeps the system perturbation minimal and increases the probability to obtain reactive pathways.

Easily accommodated by the system, early steps of substitution are mostly successful and any site is likely replaceable. The progressive variation of system composition ( $N' \rightarrow N'' \rightarrow N''' \rightarrow \dots$ ) is accompanied with either a loss or a gain in the total



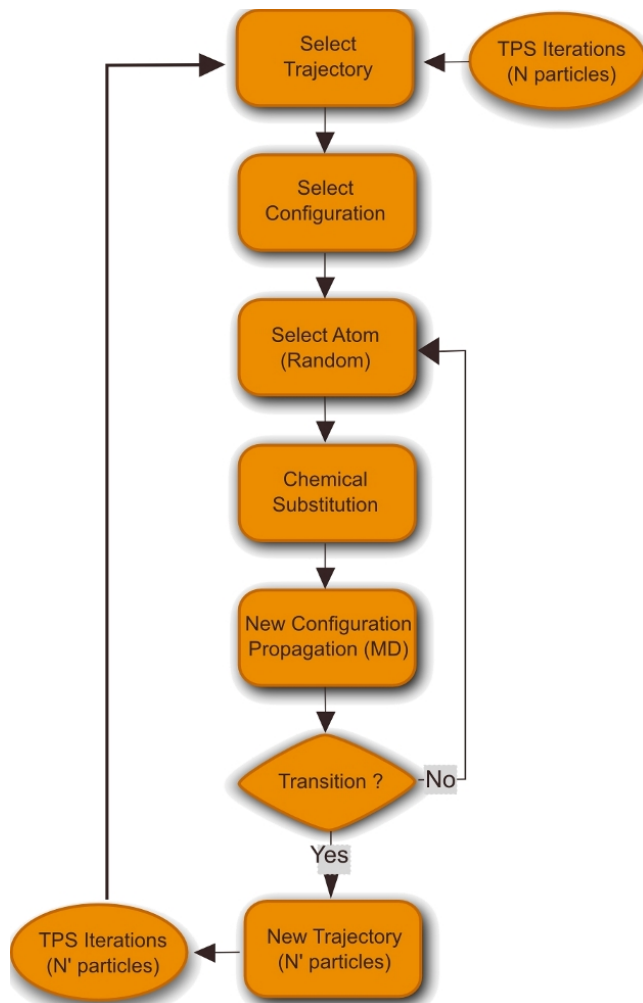


**Figure 2.8:** Diagram summarizing different steps of chemical doping procedure. Starting point is a reactive trajectory taken from TPS simulation. Substitution of atoms is only depending on the reactivity of the generated trajectory. The perturbation caused by substitution is accommodated by immediate sampling of the modified system.

mass ( $m'_{tot} \rightarrow m''_{tot} \rightarrow m'''_{tot} \rightarrow \dots$ ). Therefore, rescaling atomic momenta is required in order to keep total momentum conserved. For this, we act on pairs of positions according to:

$$P = \sum_{i=1}^{j-1} m_i v_i + m_j v_j + m_{j+1} v_{j+1} + \sum_{k=j+2}^N m_k v_k \quad (2.20)$$

$$P = \sum_{i=1}^{j-1} m_i v_i + m_j v_j + m_{j+1} \left( v_{j+1} - \frac{\delta m_j v_j}{m_{j+1}} \right) + \sum_{k=j+2}^N m_k v_k \quad (2.21)$$

The overall substitution procedure is an augmentation of TPS scheme by Monte Carlo like simulation. Therein, a walk in *chemical composition space* is performed by only visiting most probable transition regimes of different systems. Only starting and end points are defined ( $x = 0$  and  $x = 1$ ). Atom replacement is biased by the reactivity of trajectories of modified configurations.

Finding the favorable transition regime using TPS simulations is realized by identification of relevant bottlenecks in complex energy landscape. Introducing different chemical species into the system is done systematically, i. e. one atom at once. Therefore, small changes are incorporated in topology of both attraction basins and energy bottlenecks (Figure 2.9, (a)-(c)). The reactivity and weight of trajectories are slowly altered until decorrelation from the initial regime is observed (Figure 2.9, (c)-(d)). The change in transition regime is accompanied with appearance of different intermediate states, change in nucleation and growth mechanisms, and modification of limiting structures (stacking faults, superstructures, defects, etc ...).

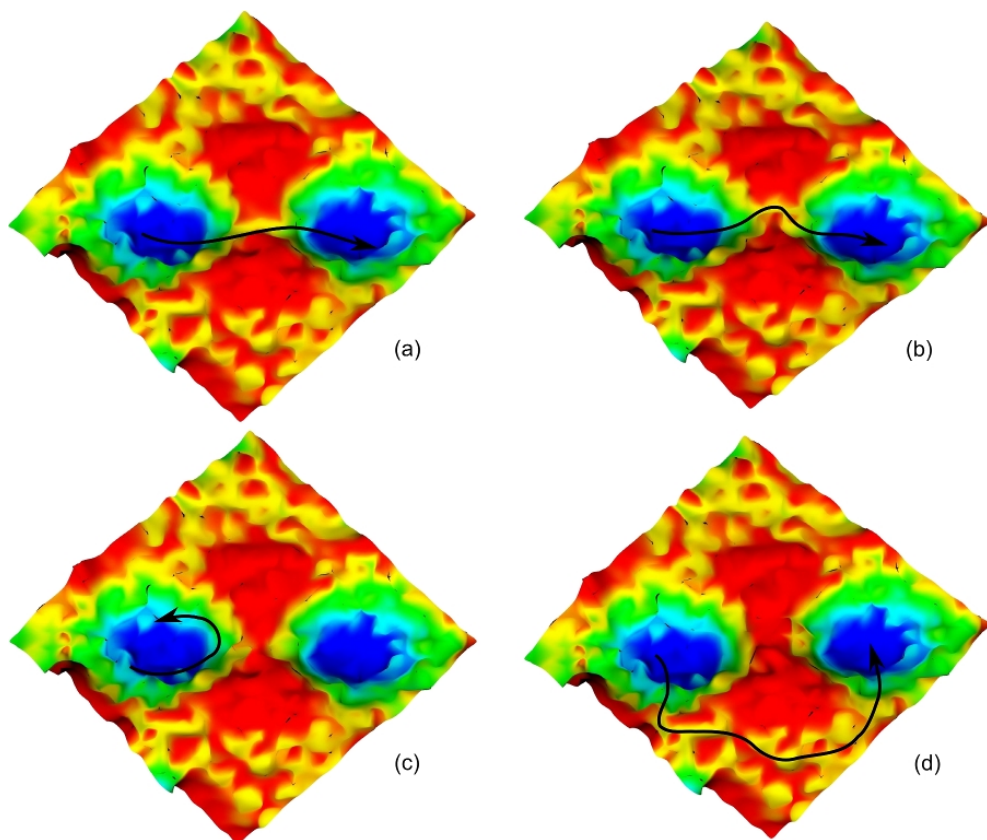


**Figure 2.9:** Schematic illustration of small and local changes in energy landscape resulting from chemical substitution. (a) Complex energy landscape corresponding to initial transition regime is systematically perturbed by small changes, (b) and (c). The topology and location of energy bottlenecks is changed lowering probability and reactivity of actual transition pathway. At the same time, other energy bottlenecks appear, compelling the system to another transition route (d). The change in transition regime is a direct result of stepwise substitution. Colors: blue, green, yellow, and red reflect an ascending energy scale.

---

# 3

## Phase Transitions in Semiconducting Materials

---

### 3.1 Gallium Nitride, GaN

Gallium nitride (GaN) is one of the most important semiconductor materials. Used in bright Light Emitting Diodes (LED) since the 1990s [69], the compound holds substantial technological potential in the field of electronics, optoelectronics, high-power transistors, and high-frequency devices capable of operating at high temperatures [70, 71]. Its particularly low sensitivity to ionizing radiation makes it a suitable material for solar cell arrays for satellites [72].

As the uses for GaN have become increasingly more sophisticated, a more in-depth knowledge is needed of its properties especially under conditions that are more and more extreme. The study of GaN response under pressure helps to understand part of these properties and to theoretically predict others that may be relevant for the synthetic efforts and improve technological uses.

#### 3.1.1 Polymorphism

Under ambient conditions, GaN crystallizes in the wurtzite (WZ) type structure in the space group  $P6_3mc$  (No. 186 –  $C_{6v}^4$ ) with Ga in  $2(b)$  ( $\frac{1}{3}, \frac{2}{3}, 0.0$ ) and N in  $2(b)$  ( $\frac{1}{3}, \frac{2}{3}, 0.375$ ), (Figure 3.1, left). Using epitaxial techniques, it is possible to grow another variety that adopts the zincblende (ZB) type structure [73, 74] in the space group  $F\bar{4}3m$  (No. 216 –  $T_d^2$ ) where Ga is located on  $4(a)$  (0,0,0) and N on  $4(c)$  ( $\frac{1}{4}, \frac{1}{4}, \frac{1}{4}$ ) (Figure 3.1, middle).

Despite the very tiny energy difference between the wurtzite and the zincblende forms (LDA: 8.4 meV/GaN pair, GGA: 11.6 meV/GaN pair [75]), the latter phase is metastable as confirmed by first-principles calculations [76].

Compared to most of isostructural compounds of IIIA-VA and IIB-VIA compounds, GaN has a rather higher ionicity [77–79]. First-principles phonon calculations predicted the rocksalt (RS) type structure ( $Fm\bar{3}m - O_h^5$ , Figure 3.1, right) to be stable at high pressure for GaN, rather than  $\beta$ -Sn type structure which is known for covalent compounds [80].

The occurrence of RS modification of GaN at high pressure was confirmed by both

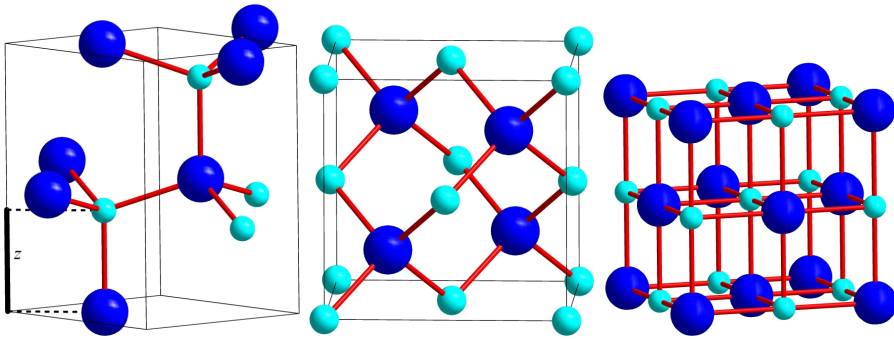


**Figure 3.1:** GaN polymorphs: (left) the wurtzite – B4, (middle) the zincblende – B3, and (right) the rocksalt – B1 type structures.

experiments and theory [81–85]. A spread in values of transition pressure, however, has been reported. Experimentally, values of transition pressure vary within the interval of 35 – 53 GPa [82–87]. Calculations based on the Hartree-Fock (HF) approximation or Density Functional Theory (DFT), yielded even a broader pressure range: 32 – 65 GPa [88–91]. The WZ–RS phase transition is reversible with a rather large hysteresis of about 20 GPa.

The potentially better performance of the rocksalt modification of GaN, due to optical gap reduction, has motivated many efforts to trap this metastable phase at ambient conditions. Some progress has been achieved in the synthesis of RS GaN nanoparticles and in growth experiments on sapphire substrates by epitaxy [92].

It is common for several ionic materials that crystallize in the rocksalt structure to undergo a phase transition to the cesium chloride (B2) structure under pressure. However, further compression of the rocksalt phase of GaN up to 70 GPa, did not reveal any other phase transition.

The formation energies of the two tetrahedral phases (WZ and ZB) are very close. This makes their coexistence possible and the transition between them controlled by temperature as often observed during molecular beam epitaxy (MBE) and metal organic vapor phase epitaxy (MOVPE) experiments [74].

### 3.1.2 Electronic Structure and Equilibrium Properties

In the wurtzite and zincblende polymorphs of GaN the conduction band minima are located at the  $\Gamma$  point in the Brillouin zone, giving rise to a direct band gap. First-principles calculations yielded values of 3.5 eV and 3.1 eV for WZ and ZB, respectively. These results are close to experimental values of 3.5 eV (WZ) and 3.4 eV (ZB) [93]. The structural phase transition B4–B1 does not alter the semiconducting nature of GaN. However, the type of the band gap is indirect. The valence band maximum is located along the  $\Gamma - K$  line in the Brillouin zone. The next highest valence band maxima manifest at  $L$  and  $\Gamma$ . DFT calculations estimated the indirect band gap between 1.80–1.70 eV lower than that in WZ and ZB phases [92].

Among the families of III–V, II–VI, and IV–VI semiconductors, GaN possesses

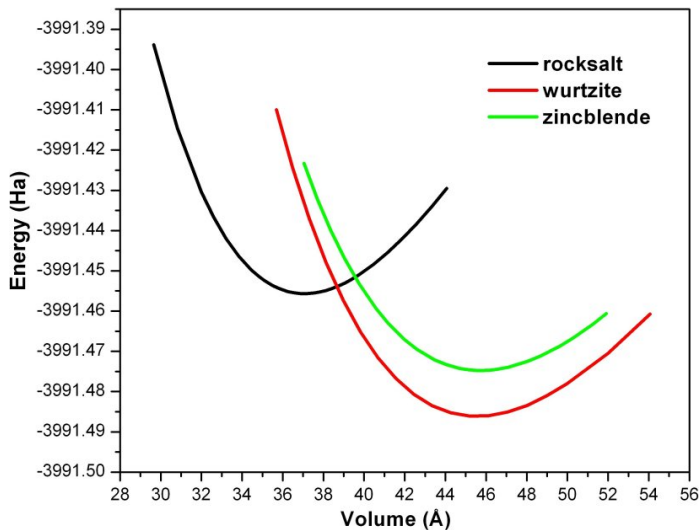


**Figure 3.2:** Total energy vs volume for GaN polymorphs

one of the most extreme physical properties, measured and calculated [94]: very short bond length, high ionicity, small equilibrium volume, low compressibility, high thermal conductivity, high melting temperature, and large energy band gap. As a consequence, the fabrication of utilizable material is rather difficult, either high quality single crystals growth or layered structure epitaxy.

The ground state WZ phase of GaN has a structure with highest symmetry compatible with both spontaneous polarization and piezoelectric effect, as the three piezoelectric tensors have non-zero independent components [95]. The ionicity of the Ga–N bond, the absence of symmetry restriction on the  $z$  coordinate of nitrogen, and the asymmetry of apical and basal Ga–N contacts within the wurtzite tetrahedra, all these three properties allow for internal displacements of nitrogen atoms along [001] and confer a non vanishing intrinsic spontaneous polarization field along [001]. *Ab initio* calculations have estimated the spontaneous polarization along [001] to be equal to  $-0.029 C/m^2$  and the piezoelectric coefficients  $e_{33} = 0.73 C/m^2$  and  $e_{31} = -0.49 C/m^2$  [95].

For symmetry reasons the polarization field should vanish in the zinblende phase of GaN. However, under shear strain or in a superlattice arrangement of ZB/WZ layers, the macroscopic polarization  $P_{Lz}$  takes a non-zero value [93].

### 3.1.3 Phase Transition Models

The WZ→RS phase transition under pressure is quite common for many binary compounds (AlN, GaN, InN, CdSe, CdS, BeO, AgI, SiC, ZnO, ...). The very fast and destructive character of the transition reflect a first-order thermodynamics that complicates the identification of the real transition pathway from experiments. Conse-

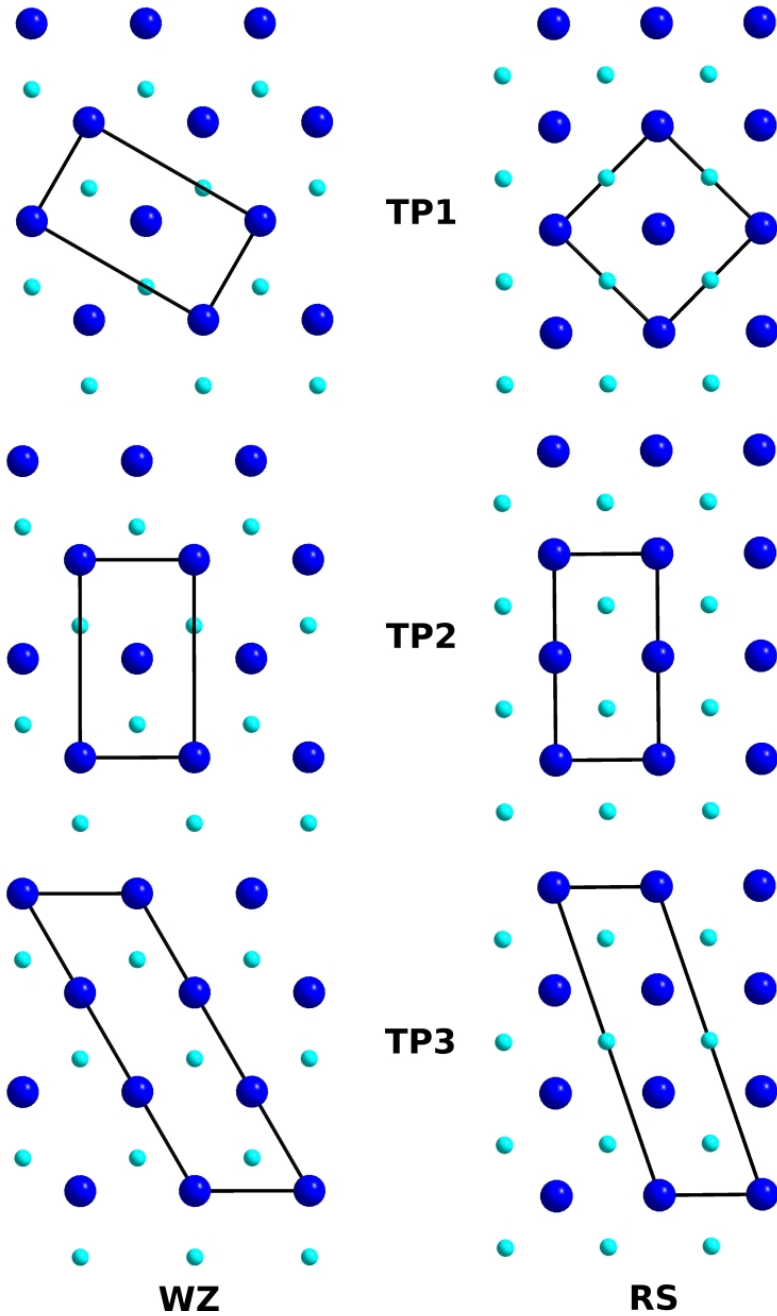


**Figure 3.3:** Three types of common cell orientation for building transition models for the B4–B1 phase transformation in GaN. TP1, TP2, and TP3 models are described in common subgroups  $Cmc2_1$ ,  $Pna2_1$ , and  $P2_1$ , respectively

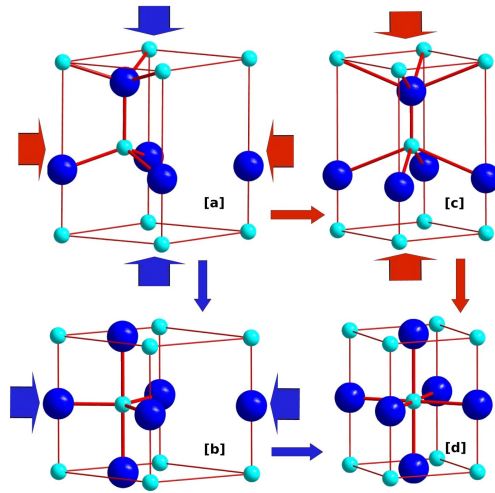


**Figure 3.4:** Two transition models for B4-to-B1 phase transformation in semiconducting materials (GaN, AlN, InN, ZnO, CdSe, etc ...). The blue path is achieved through a hexagonal intermediate structure ( $P6_3/mmc$ ). The red path is realized through a tetragonal intermediate structure ( $I4mm$ ). Both intermediates have fivefold coordinated atoms.

quently, obtaining a reliable scenario for the transformation by the determination of a detailed mechanism on the atomic level has been a challenging problem for several years for both experiments and theory. Experimentally, the first tentative to describe the WZ–RS transition as a continuous deformation was proposed by Croll [96] based on his experiments of ultrasonic pulse-echo measurements of elastic properties. Later, using X-ray diffraction and optical absorption under pressure, Tolbert and Alivisatos [97] proposed a series of models picturing the transition as deformation of chair/boat type patterns into  $2 \times 3$  rectangles. Another transformation path going through a face-centered orthorhombic intermediate configuration was suggested from shock experiments conducted by Sharma and Gupta [98]. The initial stage of the WZ–RS transition has been investigated using picosecond time-resolved electronic spectroscopy leading to a new transformation model where a face-centered tetragonal structure was identified as a necessary step for the transition [99].

On the theoretical side, a manifold of alternatives have been suggested based on *ab initio* calculations, molecular dynamics simulations, as well as geometrical methods based on symmetry arguments.

Limpijumnong and Lambrecht [100] proposed a homogeneous orthorhombic shear strain deformation based on *ab initio* calculations. They identified a fivefold intermediate structure with hexagonal symmetry, isomorphic to the layered material *h*-BN. The suggested transition sequence was  $P6_3mc \rightarrow P6_3/mmc \rightarrow Fm\bar{3}m$ . The first step is realized by changing the  $c/a$  ratio from  $c/a = 1.63$  to  $c/a = 1.2$ . The reduced  $z$  coordinate of N (Figure 3.1, left), corresponding to relative spacing  $u$  of the Ga and N sublattices is increased from  $u = 0.375$  to  $u = 0.5$  (Figure 3.4a-c). The hexagonal



directions [100], [010], and [001] are maintained as well as the  $\gamma$  angle, which remains  $120^\circ$ . The coordination number of Ga (and N) changes from 4 to 5 while WZ tetrahedra are being flattened. The resulting structure differs from layered  $h$ -BN in the interlayer spacing along [001]. In the intermediate structure (Figure 3.4c) the spacing is equal to the (001) in-plane Ga–N contacts while in  $h$ -BN it is longer. The second step leading to the RS structure is achieved on compression along  $[1\bar{1}0]$  parallel to (110) bringing the ration  $c/a$  to  $\sqrt{2}$  (Figure 3.4d).

Using a geometrical heterogeneous sphere packing method [101], an intermediate phase with  $Cmc2_1$  symmetry is identified along the transition. By means of molecular dynamics simulations combined with DFT calculations, Shimojo *et al.* [102] obtained two new transition paths. Later, one of these two new proposals has been clarified by Sowa [103] providing crystallographic description of the transformation based on  $Pna2_1$  symmetry. The concept of maximal symmetry transition paths used by Capillas *et al.* [104] supports the previous findings of  $Pna2_1$  and  $Cmc2_1$  symmetries as possible transition paths. Stokes *et al.* [105] recently summarized these transition paths and described them by means of a bilayer sliding mechanism within  $Cmc2_1$ ,  $Pna2_1$ , and  $P2_1$  space group symmetries as shown on Figure 3.3.

Finally, it is worth mentioning the tentative to unify the description of the WZ–RS phase transition in wide-gap semiconductors conducted by Saitta and Decremps [106] by considering the effect of  $d$  electrons on the elastic properties and phonons during the transition. Besides the path going through a hexagonal intermediate ( $h$ -BN like), another deformation characterized by the passage through a fivefold tetragonal intermediate is proposed (Figure 3.4a→b→d). The first step of the path is described within a common monoclinic cell to allow the  $\gamma$  angle to change from  $120^\circ$  to  $90^\circ$ . Consequently, ions move horizontally towards the center of square pyramids formed by five counter-ions (Figure 3.4 [a]→[b]). On lowering the  $c/a$  ratio, ions reach the center of the pyramids base as a second step leading to the RS structure (Figure 3.4 [b]→[d]). They concluded that compounds with light cations (no  $d$  electrons: AlN and SiC) should follow the first path while heavier cation compounds (GaN, InN, and ZnO) prefer the second one.

The general diversity of the proposed transition mechanisms reflects no fundamental discrepancy but the need to move the transformation path investigation away from static models which are confined to prejudiced mechanistic models. The use a common subgroup to describe the B4–B1 transition is inferred by the absence of a direct group-subgroup relation between the space group symmetries of the WZ and RS structures. In this case, any mechanism emerging from approaches based on such restriction are biased to the chosen specific common orientation of the limiting structures WZ and RS, as well as the size of the common cell where the deformation is described.

The mechanistic challenge imposed by the wurtzite–rocksalt phase transition under pressure requires an articulated answer with a clear distinction between the suggested paths. The investigation of the B4–B1 transformation should focus on the determination of the overall transition mechanism, and the identification of intermediate configurations involved therein.

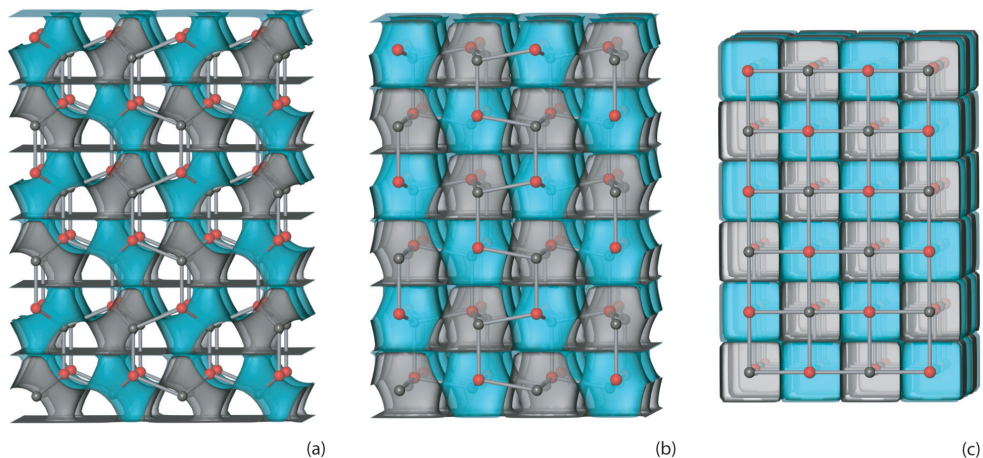


**Figure 3.5:** Model transformation mapping the network of (a) B4 onto the network of (c) B1. The Ga (gray) and N (red) atom sets are separated from each other by a PNS (the corresponding gray/green manifold is displayed). The latter develops perpendicularly with respect to shortest Ga–N connections. Figure 1(b) represents an intermediate between (a) and (c).

### 3.1.4 Wurtzite-to-Rocksalt (B4–B1) Phase Transition

The manifold of transformation paths described in the previous section are based on procedures assuming that the system periodicity is retained along the transition path, thus, implying collective atomic displacements. As it transforms from WZ to RS, the structure is supposed to be described all along the path by the symmetry of a common subgroup. Clearly, due to such assumptions, nucleation and local deformations propagation during the transition process cannot be accounted for. The averaging of atomic displacements makes the corresponding local atomic environment similar along different path and results into similar energy barriers [102, 103].

In a situation characterized by many mechanistic alternatives, fair account of relevant aspects of the WZ–RS transformation can be provided by the use of transition path sampling methodology. The overall iterative simulation approach develops from an initial trajectory connecting B4 and B1 phases. Although many models can be used for the fabrication of the first trajectory, the intelligent design of such a trajectory affects the calculation performance in terms of the number of TPS moves required to achieve trajectory decorrelation from the initial regime. On the other hand, different starting points may give access to different intermediate regimes along the decorrelation process. Therefore, for the B4–B1 transformation, we used a geometric-topological approach based on transforming periodic nodal surfaces (PNS) [107–109].

This method provides a means to extract intermediate configurations between B4–B1 along distinct quasi-orthogonal paths (with respect to the deformation modes coded therein), with a typically concerted nonlinear mapping of atomic positions from the initial (B4) to the final (B1) configurations. This approach has many immediate

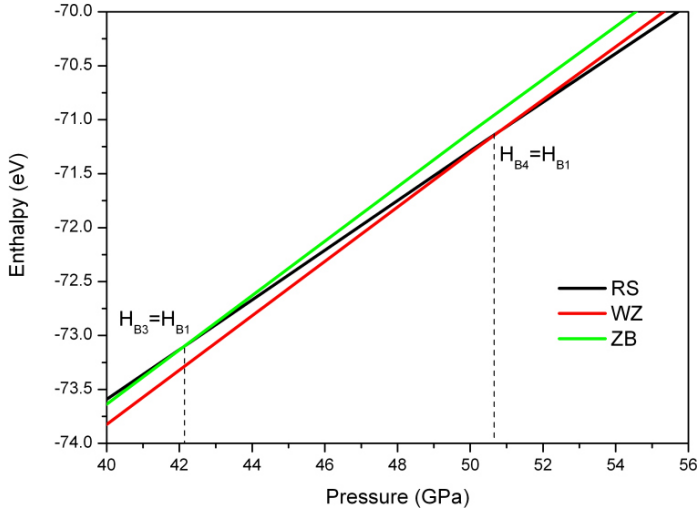


**Figure 3.6:** Enthalpy vs. pressure of GaN polymorphs

advantages:

- Initial very high-energy/high-strain configurations can be avoided,
- Independent TPS runs can be started from distinct initial mechanistic regimes,
- Different features can be coded in the initial path.

Additionally, many initial mechanisms can be checked for their convergence toward the same final mechanistic regime after TPS processing.

The approach of modeling of the first trajectory is illustrated in Figure 3.5. Figures 3.5a and 3.5c show the B4 and B1 networks with a periodic nodal surface wrapped around each one of them. Such a surface is calculated from a short Fourier summation and is chosen such that the zeroth value isosurface develops perpendicular to the shortest Ga–N connections (Figures 3.5a-c). Like this, Ga atoms are placed on the positive side (blue side) of the surface, while the N atoms on the negative one (gray side). This offers a means to code the whole atomic arrangement into a single parametric expression. From the limiting functions (Figures 3.5a and 3.5c) a dense set of intermediates can then be derived by interpolation. The configuration and the surface corresponding to the middle point are given in Figure 3.5. The shown deformation corresponds to vertically shortening a set of Ga–N connections.

The intermediate structures *h*-BN like (*iH*) and *tetragonal* (*iT*) suggested by Saitta and Decremps [106] for phase transitions in wide band-gap semiconductors, in particular GaN, involve different types of strain. They can be artificially combined in a similar way to that proposed by Sowa [101]. Here we have derived the first trajectory in a regime related to the latter. This implies concerted shearing perpendicular to  $[001]_{B_4}$ , cell compression along  $[120]_{B_4}$ , and cell expansion in the  $[100]_{B_4}$  direction, and a shuffling of  $(100)_{B_4}$  layers.

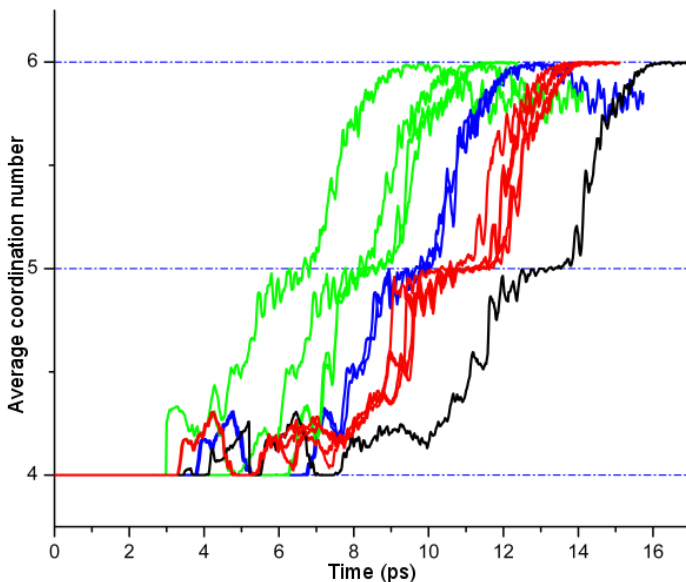


**Figure 3.7:** Time evolution of Ga average coordination number (CN) during the B4–B1 transformation in the course of transition path sampling iterations. Green curves correspond to early trajectories produced during sampling. Blue curves mark local appearance of tetragonal intermediate  $iT$ . Red curves are characterized by predominance of  $iT$  in early stages of transformation and during reconstruction of WZ structure. Black curve is a representative profile of Ga CN variation corresponding to real mechanism. Therein,  $iT$  appears as metastable phase as indicated by the plateau at CN=5.

The geometric-topological modeling enables the construction of several dynamical transition states. Using molecular dynamics integration<sup>1</sup>, the propagation of the corresponding configurations forward and backward in time provides a first dynamical trajectory connecting B4 and B1 to be used in the initialization of the transition path sampling iterations. The latter are performed within the NpT ensemble<sup>2</sup> by applying momentum modifications to snapshots taken from the previous trajectory, keeping total energy, momentum, and angular momentum unchanged. The propagation of the new configuration in both directions of time provides a new trajectory that is examined for the process of interest, and the procedure is iterated. This represents a mean to successively rectify a (more or less good-guessed) initial trajectory, which thus does not need to correspond to a favorable transition route *per se*.

In order to distinguish between WZ and RS during simulations, next-neighbor average coordination number (CN) of the cations (cutoff 2.3 Å) was used as order parameter varying between 4 (B4) and 6 (B1). This of course does not enforce any particular evolution of the coordination number during TPS iterations. The variation

<sup>1</sup>MD simulations were carried out using DLPOLY package [110] with 0.2 ps time step to ensure a good time reversibility

<sup>2</sup>Constant pressure and temperature were ensured using Melchionna/Nose-Hoover algorithm [111]

in the CN is a consequence of pressure application with no bias imposed therein.

The simulation box contained 1176 atoms where interatomic forces were determined using a set of empirical force field parameters developed by Zapol *et al.* [112]. The two-body interatomic potential consists of a long-range Coulombic part and a short-range part. Ewald summation [61] was applied for the treatment of the long-range Coulomb interactions, while short-range interactions were described by an analytical expression of the Buckingham form for atoms  $i$  and  $j$ :  $V_{ij} = A \exp(-r_{ij}/\rho) - Cr_{ij}^{-6}$ . A cut-off radius of 10 Å was used for long-range interactions. For the nitrogen atom, polarization effects were taken into account by the shell model approach [113] in which the electrons are modeled by a massless shell with charge  $Y$  which is coupled with the core by a spring with a constant  $K$ . The polarizability is then given by  $\alpha = Y^2/K$ . The model correctly reproduces the high pressure phase transition from the wurtzite to the rocksalt phase occurring at  $\sim 50$  GPa which corresponds to mid-value of the experimental hysteresis (Figure 3.6).

No artificial enhancing of the transition, such as applying very high temperature or overpressurizing the system, has been used in the simulations. Temperature was set to 300 K and the pressure to 50 GPa, the mean value of experimental results.

Within 10–15 TPS iterations, the mechanistic features inherited from the geometric model disappear allowing to elucidate the reasons of their disfavor.

In the initial regime, sixrings are initially compressed along [120] such that additional Ga–N contacts result. This implies that the [100] direction in rocksalt is parallel to [100] in wurtzite. These tentative nucleation centers regress again and the system is rearranged into a symmetric configuration related to the hexagonal wurtzite structure but slightly compressed along [120]. Such a configuration corresponds to the symmetric intermediate structures prepared via geometric modeling.

In the course of TPS iterations, configurations corresponding to a tendency to stay longer in a coordination number equal to 5 clearly emerge (Figure 3.7, green profile). After full trajectory decorrelation, this tendency becomes a pronounced feature (Figure 3.7, blue→black profile evolution). The visualization and close examination of snapshots around 5 ps (Figure 3.8) allow for the identification of a tetragonal intermediate structure  $iT$  belonging to the  $I4mm$  space group symmetries. This preference rules the hexagonal intermediate  $iH$  out.

The onset of the transition is characterized by the formation of nucleation centers (Figure 3.8, at  $t = 0$  ps, yellow islands). In the puckered  $(001)_{B4}$  layers, the 6-rings are compressed along [120] into 4-rings. Subsequently, the nucleation centers progress and propagate along [200] to form a bidimensional (2D) slab (Figure 3.8, at  $t = 3$  ps). The latter grows perpendicularly to its formation direction (Figure 3.8, at  $t = 4$  ps) until complete conversion of the wurtzite structure into intermediate tetragonal structure  $iT$  (Figure 3.8,  $t = 5$  ps) similar to the high-pressure form of tin phosphide SnP [114] and GeAs [115]. The phase growth is achieved via two fashions (Figure 3.10). Depending on the way adjacent 6-rings are getting deformed into 4-rings, the  $(001)_{B4}$  layer shearing can be achieved via rings compression along [120] or by combining the latter with another compression along [210]. The centers of nucleation as well as the formation of the 2D slab were observed to occur according to the first shearing mode. Further growth however, follows the second pattern. The overall reconstruction of the  $(001)_{B4}$  layers consists of a combination of parallel and

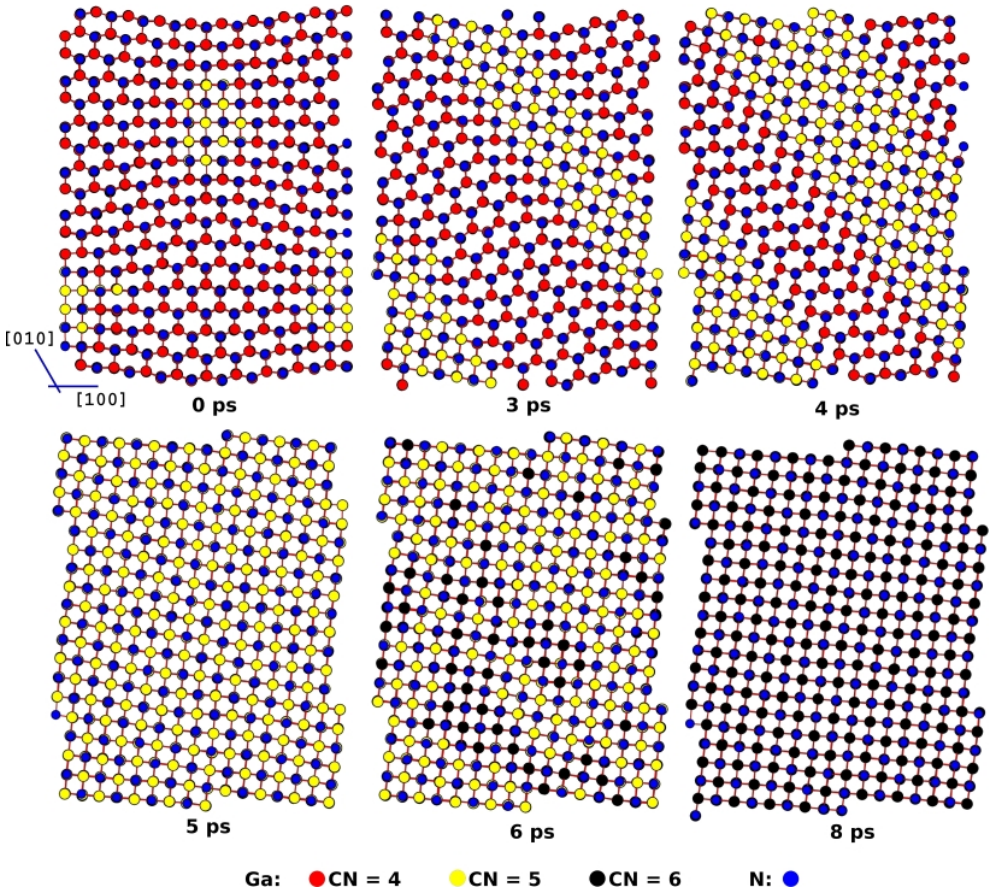


**Figure 3.8:** Snapshots taken from a representative trajectory of B4–B1 transition mechanism in GaN. Front view, parallel to  $(001)_{B4}$ , is shown. Ga atoms are colored according to coordination number. Nucleation centers appeared at  $t = 0$  ps. Interface is created via  $(001)_{B4}$  layers shearing between  $t = 3$  and  $t = 4$  ps. WZ structure is completely transformed into intermediate structure with fivefold coordinated atoms,  $iT$ , at  $t = 5$  ps. Transformation into RS structure is accompanied with CN increase from 5 to 6 between  $t = 5$  to  $t = 8$  ps.

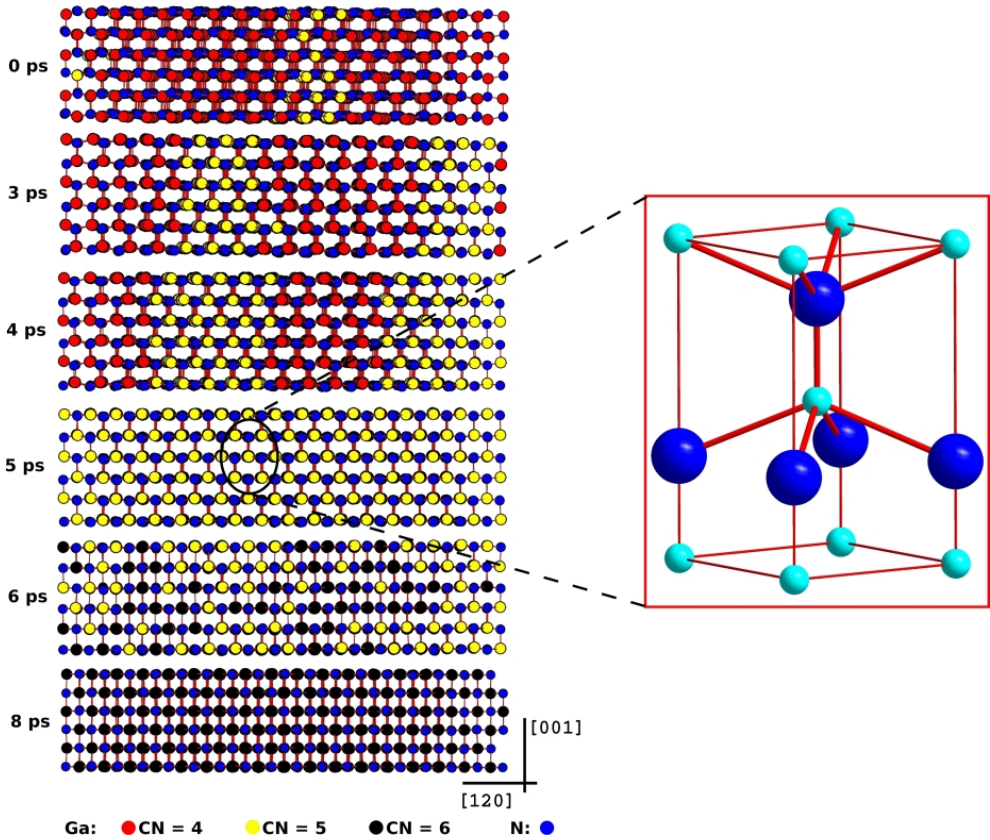


**Figure 3.9:** Snapshots taken from a representative trajectory of B4–B1 real transition mechanism in GaN. Side view, along  $[001]_{B4}$ , is shown. While relative spacing between sublattices in WZ is not changed, intermediate structure with fivefold coordinated atoms is formed because of  $(001)_{B4}$  layers shearing ( $t = 0-5$ ps). Inset on the intermediate metastable structure  $iT$  indicates a pyramidal environment in a tetragonal cell described in space group  $I4mm$ . Transformation into RS structure is realized by  $iT$  structure compression along  $[001]_{iT}$ . The overall B4–B1 transition mechanism is a two-step transformation.

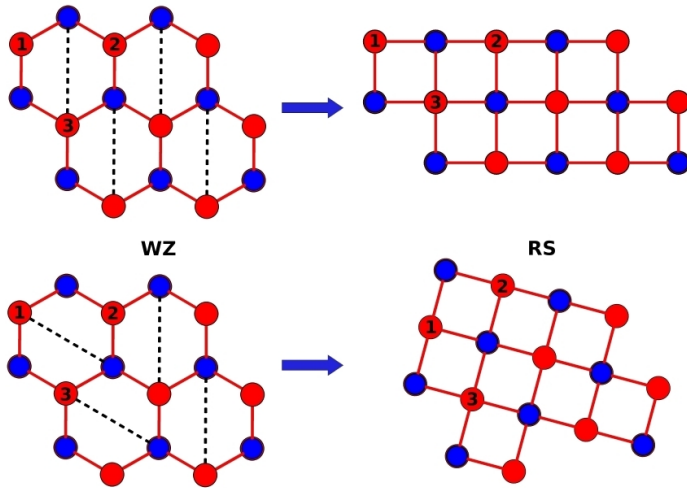


**Figure 3.10:** Two different fashions of  $(001)_{B4}$  6-rings compression into  $(001)_{B1}$  squares

antiparallel displacements of the  $(200)_{B4}$  layers.

The volume collapse accompanying the transition is about 20% from WZ to RS. The broadening of Raman lines on strain reversal suggests that crystals do not transform as a single homogeneous domain. The unbiased mechanism proposed from TPS simulations provides the answer to morphology issue.

The combination of parallel and antiparallel layers shuffling reflects the tendency to avoid excessive strain during the phase transition. Although the onset of the transition is initiated by the first mode of 6-ring compression (Figure 3.10, upper panel), the system prefers combining with the second mode (Figure 3.10, lower panel) splitting the strain into two directions ( $[120]$  and  $[210]$ ) instead of one ( $[120]$ ). Consequently, the RS structure is tilted about  $[001]$  if compared to WZ and the direction  $[100]_{B1}$  is no longer parallel to  $[100]_{B4}$  (Figures 3.8 and 3.10).

After complete transformation of the wurtzite-type structure into the intermediate tetragonal configuration (Figure 3.8, at  $t = 5$  ps), atoms move along  $[001]$  toward the base of the square pyramids (Figure 3.8, at  $t = 6$  ps), locking into the final rocksalt-type structure (Figure 3.8, at  $t = 8$  ps).

The onset of the transition is marked by nucleation and growth of a metastable structure on which the system stays longer than 1 ps (Figure 3.7, black profile). The time resolution of picosecond time-resolved electronic spectroscopy is around 100 ps, and only in particular cases helpful in identifying a possible intermediate, like for CdS in shock wave experiments [99]. One of the main experimental difficulties is the strong overlap of the tetragonal structure peaks with those of wurtzite and rocksalt during X-ray powder diffraction (XRD) data refinement [116]. The time resolution of our simulations on the contrary allows for a clear identification of distinct events on the atomic level. The nucleation and growth sequence, wurtzite–tetragonal then



tetragonal–rocksalt, clearly reflects a two-step transformation mechanism where the tetragonal intermediate  $iT$  does not simply link the limiting structures in a crystallographic way as described by Saitta and Decremps [106] but stands as a metastable one, reflecting a different energetic profile of the transition path. The energy landscape of GaN encompasses, besides WZ, ZB, and RS, a new polymorph with a tetragonal symmetry (space group  $I4mm$ ,  $Z = 2$ ).

Second-order phase transitions are continuous and may imply the softening of phonon modes at the transition point [79]. The study of phonon dispersion curves of semiconducting materials under pressure is a key to understand phase stability and the existence of possible metastable structures in terms of distortion associated with soft acoustic and optic modes [106]. Raman experiments on compressed GaN have identified shear mode softening within the critical pressure range [82]. Besides the  $c_{44}$  and  $c_{66}$  elastic constants, the  $E_2^{low}$  optic phonon mode at  $\Gamma$  point in the Brillouin zone is as well reported to soften. The scenario of nucleation and growth emerging from our simulations makes a direct comparison with *ab initio* calculated phonons rather adventurous, and the time scale of Raman experiments is orders of magnitudes higher than the simulation time window. Nonetheless the experimental evidence of shear modes becoming soft at a higher pressure than the equilibrium transition pressure [82] implies that along the transformation path there is some additional finite barrier to cross. From Figure 3.8, the 2D interface can be seen to not reconstruct directly into the B1 type, as the path still has to overcome a small obstacle before getting to the final rocksalt structure. The manifold of decorrelated trajectories collected after convergence shows no preference for RS nucleation during the second step tetragonal–rocksalt (Figure 3.8,  $t = 5 - 8$  ps).

The  $n$ -type conductivity in GaN is attributed to intrinsic defects, dominated by Schottky disorder [112]. We investigated the effect of defects incorporation on the transition mechanism of the WZ–RS transformation.

GaN pair vacancies were randomly introduced and accepted or rejected depending on the success or failure to observe the B4–B1 transition as described in Chapter 2, Section 2.4. This was used as an additional means to achieve trajectory modification, beyond the original simulation scheme [117]. Along this line, the system is driven from one composition to another, which includes transformation of the B4–B1 transition routes. Each incorporation step is followed by at least 30 TPS iterations at constant composition to ensure relaxation. The presence of defects does not change the general mechanistic picture described above and has no noticeable effect on the lifetime of the intermediate configuration. However, it affects the nucleation, which preferentially starts at vacancy positions. The latter lower the coordination number locally and ease the displacement of undercoordinated atoms. Repeated incorporation of defects favors the rocksalt phase over the hexagonal structure.

## 3.2 Al<sub>x</sub>Ga<sub>(1-x)</sub>N and In<sub>x</sub>Ga<sub>(1-x)</sub>N Solid Solutions

The isostructural compounds, AlN, GaN, and InN are direct wide band-gap semiconductors (GaN 3.4 eV, AlN 6.3 eV, and InN 1.9 eV) with a gap ranging from the ultraviolet (UV) to the visible regions of the spectrum [75]. The latter property con-

fers important technological potential for either pure or mixed phases in the field of optoelectronic devices operating at a broad range. Consequently, cation substitution allows control over the wavelength of emission in order to fabricate single or multiple quantum well structures which can improve the efficiency of LEDs [118, 119].

AlN and InN crystallize in the wurtzite type structure. They inherit much of the extreme properties of GaN (see Section 3.1.2). Under pressure they undergo a phase transition to the rocksalt type structure the same as GaN but at lower transition pressure [79]. Upon decompression, InN and GaN rocksalt phases revert to the wurtzite-type structure, unlike AlN that stays in the high-pressure phase on releasing pressure back to normal conditions, as one of a few exceptions in semiconductors [79, 120]. This difference of behavior adds to the complexity and difficulty of finding microscopic mechanisms of the first-order transformation in group-III nitrides under pressure. The determination of the role of the cationic moiety ( $\text{Al}^{3+}$ ,  $\text{Ga}^{3+}$ , and  $\text{In}^{3+}$ ) in the transformation process in terms of local events of nucleation and growth contributes to a better understanding of behavior of group-III nitrides under high-pressure and offers valuable hints for the synthetic efforts. These perspectives motivated us to combine the three cations in mixed systems,  $\text{Al}_x\text{Ga}_{1-x}\text{N}$  and  $\text{In}_x\text{Ga}_{1-x}\text{N}$ , and perform simulations on varying the doping within the interval  $0 < x < 0.05$ .

Molecular dynamics simulations combined with TPS approach have been carried out for the heterogeneous system where the mixing was ensured by successively introducing chemical substitutions to the WZ–RS transition in GaN. Starting from converged trajectories from the GaN TPS runs, aluminum and indium cations were progressively incorporated by random substitution of gallium, in the same manner as described for vacancies. To describe the interaction between different species composing the mixed systems, we employed a set of pair potentials developed by Chisholm *et al.* [118] based on the set proposed by Zapol *et al.* [112] for pure GaN.

### 3.2.1 Substitution of Gallium with Indium

Substitution with indium does not affect the overall transition mechanism because the features characterizing trajectories in pure GaN are kept. The system stays in the same regime crossing the tetragonal intermediate  $iT$ . Substitution moves show a high acceptance probability. Up to 90 % of tentatives to substitute a Ga position, randomly chosen, are accepted and the WZ–RS transition is observed. This reflects a compatibility of InN and GaN in terms of energetical preferences during the transformation process.

The presence of In atoms does not hinder the formation of the tetragonal intermediate neither its pronounced metastability. The fingerprint of the pure GaN mechanism is the  $(001)_{\text{B}_4}$  layers shearing. On In doping of GaN, the shearing direction, before (upper panel) and after In incorporation (lower panel), is maintained as shown on Figure 3.11 (blue arrow). From Figure 3.11, a clear tendency to form In islands is observed. Therein, nucleation is preferentially started. Indium clustering reduces the strain caused by the size mismatch in cell parameters between InN and GaN. The higher polarizability of In, due to the presence of d electrons [14], obviously allows for an easier response to local structure modifications.

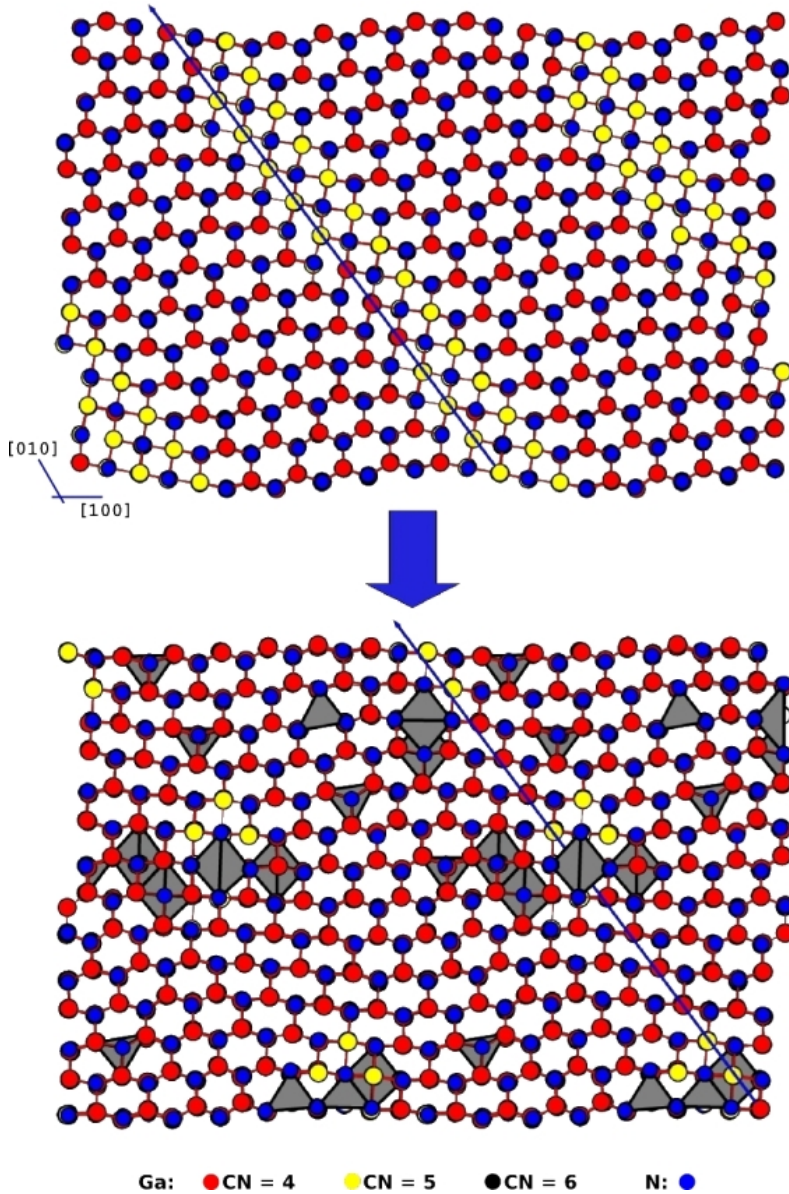


**Figure 3.11:** Early stages of the B4→B1 transformation in pure GaN (upper) and after (lower) doping with In (grey polyhedra). Grouping in small clusters is preferred by In atoms to minimize strain caused by cell parameter difference between GaN and InN. (001)<sub>B4</sub> layers shearing direction, marked by blue long arrow, is maintained after doping. Nucleation of intermediate structure *iT* is preferentially started at In clusters.

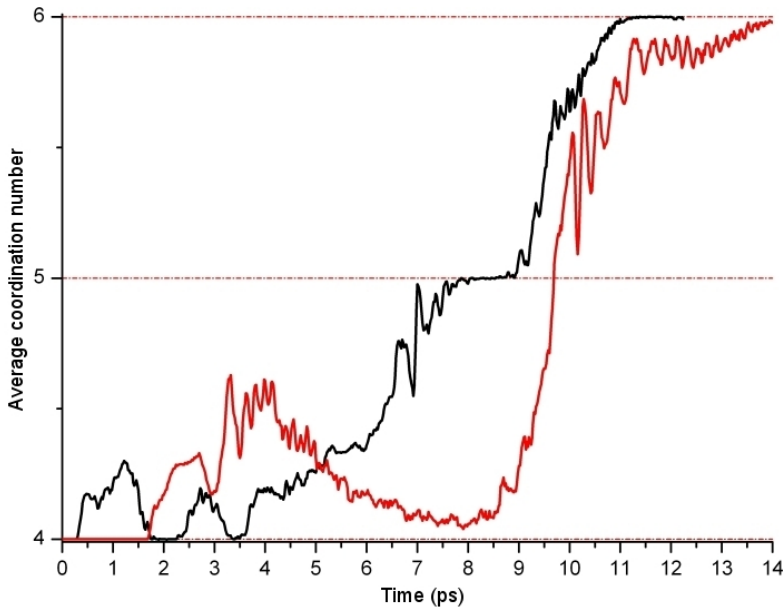


**Figure 3.12:** The variation of coordination number of Ga atoms during B4→B1 transformation in pure GaN (black curve) and after (red curve) doping with Al

### 3.2.2 Substitution of Gallium with Aluminum

The cation substitution of gallium by aluminum has a stronger effect on the transition mechanism. The change in the cation coordination during the transformation (Figure 3.12) implies intrinsic modifications that can be traced back to local events. The two main events characteristic of the transformation in pure GaN and preserved in  $\text{In}_x\text{Ga}_{1-x}\text{N}$  are:

- $(001)_{\text{B}_4}$  layers shuffling mode,
- formation of metastable tetragonal intermediate,  $iT$ .

The correlation between the latter aspects controls the reactivity of the system at the B4/ $iT$ /B1 interface during the nucleation and growth of the high pressure phase.

Unlike doping with In, stepwise substitution of Ga with Al shows rather a preference for spreading the dopant within the simulation box. On increasing the number of Al atoms in the system, nucleation centers avoid Al sites on early stages of transformation. The development of these nucleation centers into a bidimensional slab leading to phase growth involves  $(2\bar{2}0)_{\text{B}_4}$  layers shearing instead of the pristine  $(220)_{\text{B}_4}$  layers as illustrated on Figure 3.13 (the blue arrow indicates the direction of layers shearing). On further simulating, aluminum cations spread over the system progressively quench the pathway through the tetragonal intermediate as they contrast phase growth.

The reorientation of the  $(001)_{\text{B}_4}$  layers shearing direction reflects a different energy profile of the new transition regime. Therein, the energy minimum corresponding to

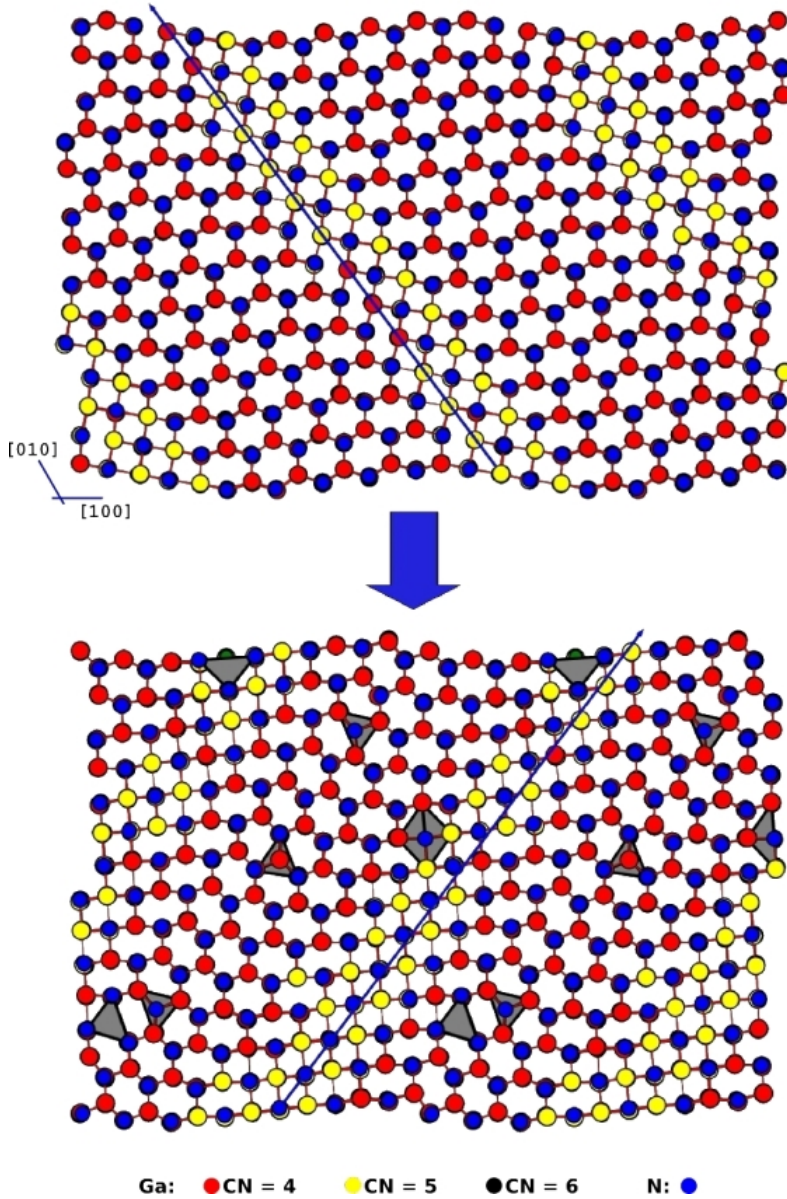


**Figure 3.13:** Early stages of the B4→B1 transformation in pure GaN (upper) and after (lower) doping with Al (grey polyhedra).  $(001)_{B4}$  layers shearing direction, marked by blue long arrow, is modified as a result of transition regime change. Nucleation of intermediate structure  $iT$  is preferentially started off Al sites. The latter are spread in simulation box to avoid quenching the transition path through tetragonal intermediate  $iT$ .

the tetragonal intermediate is no longer accessible nor functional for the transformation, and fivefold tetragonal geometry is no longer observed.

At 5 % of cation substitution, the metastability of the tetragonal phase is drastically altered and the phase growth crosses over directly to the rocksalt phase with the tetragonal structure surviving as an interface between wurtzite-type and rocksalt-type structural motifs. With the removal of the tetragonal intermediate the backward transformation is noticeably modified. The disappearance of the intermediate supports a scenario of lifting soft modes in the high-pressure regime under the influence of Al, measured for AlN.

In summary, the pressure-induced wurtzite-to-rocksalt (B4-B1) phase transition in GaN was studied by means of molecular dynamics simulations combined with transition path sampling method. The overall reconstruction was determined as a two-step mechanism going through a tetragonal intermediate structure ( $iT$ ). The latter is metastable and separates the two stages of transition:  $B4 \rightarrow iT$  and  $iT \rightarrow B1$ . A combination of two fashions of hexagon compression characterized the first step, while the second was realized by atomic movements along  $[001]_{iT}$  ( $// [001]_{B4}$ ) toward the base of  $iT$  pyramids. In both transformation steps, nucleation and growth were observed. However, the shape of nuclei is different at times of formation of  $iT$  structural motifs within wurtzite structure, and rocksalt within  $iT$  structure.

The effect of the presence of chemically different species in GaN on the transition mechanism was explored. Doping via Ga replacement with Al and In was performed using a stepwise procedure built on the top of transition path sampling. Therein, acceptance or rejection of replaced sites is directly connected to the reactivity of the corresponding pathway.

Substitution of Ga with In resulted into a clustering of the dopant in the form of islands where the reconstruction was observed to preferentially begin. The transition scenario was kept similar to that of pure GaN. Substitution of Ga with Al, however, drastically altered the metastability of the tetragonal intermediate  $iT$ . Further Al doping caused the suppression of the latter intermediate structure leading to a complete change of the B4-B1 reconstruction mechanism.

## 3.3 Zinc Oxide, ZnO

Although zinc oxide (ZnO) has been used since 1935 as an additive into numerous materials and products [121,122] (plastics, ceramics, glass, rubber, lubricants, paints, ointments, adhesives, sealants, pigments, foods, batteries, ferrites, fire retardants, etc.), it is revealed a material of top interest [123]. ZnO has found its first electronic application as thin layer for surface acoustic wave devices after the discovery of its good piezoelectric properties in early 1960s. The renewed interest in this material due to the development of growth technologies for the fabrication of high quality single crystals and epitaxial layers, allowing for the realization of ZnO-based electronic and optoelectronic devices [124]. The spectrum of properties of ZnO grows broader and the associated uses vary from food additives to sun screening agents including the semiconductors field. In order to accompany such rapid expansion, the structure/property/function relationship has to be determined and understood.

In this section we undertake a study of structural switching of ZnO polymorphs under pressure by elucidating the transition mechanism at the atomic level of details to attempt answering different issues are left open by experiments.

### 3.3.1 Polymorphism

Zinc oxide naturally occurs as the mineral *zincite* that crystallizes in the hexagonal wurtzite structure (B4 type). The crystal structure was elucidated by Bragg in 1914, shortly after the discovery of X-ray diffraction [125]. The hexagonal lattice, belonging to the space group  $P6_3mc$  with  $a = 3.250 \text{ \AA}$  and  $c = 5.207 \text{ \AA}$ , is characterized by two sublattices of  $\text{Zn}^{2+}$  and  $\text{O}^{2-}$ . Each ion is surrounded by 4 counter-ions in a nearly tetrahedral configuration.

In an ideal hexagonal wurtzite structure, the axial ratio  $c/a$  and the  $u$  parameter ( $z$  coordinate of atom in position 2( $b$ ), corresponds to the cations and anions sublattices spacing) are correlated according to the relationship  $u.c/a = (3/8)^{1/2}$ , where  $c/a = (8/3)^{1/2}$  and  $u = 3/8$  for an ideal structure. The measured ZnO crystal deviates from the latter ideal arrangement in both values. Experimentally, there is an asymmetry in Zn–O bond lengths, the distance along  $[001]_{B4}$  is somewhat smaller ( $d_{\text{Zn-O}}^{\text{apical}} = 1.90 \text{ \AA}$ ) than the three other interionic contacts ( $d_{\text{Zn-O}}^{\text{basal}} = 1.98 \text{ \AA}$ ). The real values of  $u$  and  $c/a$  were determined in the range  $u = 0.3817 - 0.3856$  and  $c/a = 1.593 - 1.6035$  [124–128].

In addition to the wurtzite phase, ZnO can adopt the cubic zincblende structure (B3) as a metastable phase. This phase is only obtained by growth on cubic substrates [129,130].

The polymorphism of ZnO is very similar in many respects to that of GaN and extends under pressure to the cubic rocksalt structure (B1). The first indication of a first-order pressure-induced phase transition to the rocksalt structure was reported by Bates *et al.* at a pressure of  $\sim 10 \text{ GPa}$  (ambient temperature) while the volume decreased by about 17 % of the unit cell volume. The phase boundary between B4 and B1 phases of ZnO has been recently revisited and corrected by Decremps *et al.* [131] with an equilibrium transition pressure near 6 GPa as illustrated on Figure 3.14 <sup>3</sup>.

---

<sup>3</sup>Figure adapted from [131]

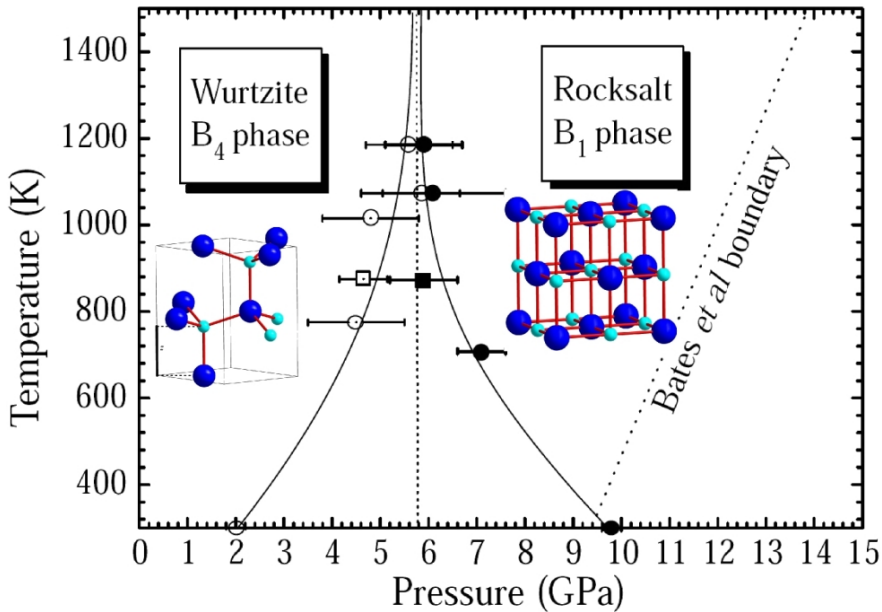


**Figure 3.14:** Phase boundary between wurtzite and rocksalt phases of ZnO.

The B<sub>4</sub>–B<sub>1</sub> transition has been characterized to be fully reversible with a pronounced hysteresis (2–10 GPa) [131–133]. However, other reports have found that a large fraction of the rocksalt B<sub>1</sub> phase persists during decompression and can be partially quenched at ambient conditions [126, 134, 135]. Nonetheless, the size of the nanoscale grains plays a major role in the delay of the B<sub>1</sub>–B<sub>4</sub> phase transition and could be the key to full quenching of the B<sub>1</sub> phase of ZnO [136, 137]. In a recent study [138], transmission electron microscopy (TEM) revealed that quenched nanoscale sample has predominantly the B<sub>4</sub> structure, while some particles were in the B<sub>1</sub> structure after the compact sample was pulverized for the TEM study. Furthermore, electron irradiation was found to promote the B<sub>1</sub>–B<sub>4</sub> transformation.

Like for binary semiconductors exhibiting the B<sub>4</sub>–B<sub>1</sub> phase transition, theoretical calculations suggest another cubic polymorph for ZnO as a result of a not yet experimentally observed phase transition from rocksalt phase B<sub>1</sub> to a cesium chloride B<sub>2</sub> structure [139, 140]. A high-pressure X-ray diffraction study found that the B<sub>1</sub> phase of ZnO is stable at least up to 202 GPa [141].

Using first-principles molecular-dynamics simulations, a possible phase transition of ZnO from wurtzite to zinc blende structures has been predicted. At 300 K, the phase transition is expected to occur at a pressure lower than 30 GPa with an activation energy barrier of 0.386 eV/atom.



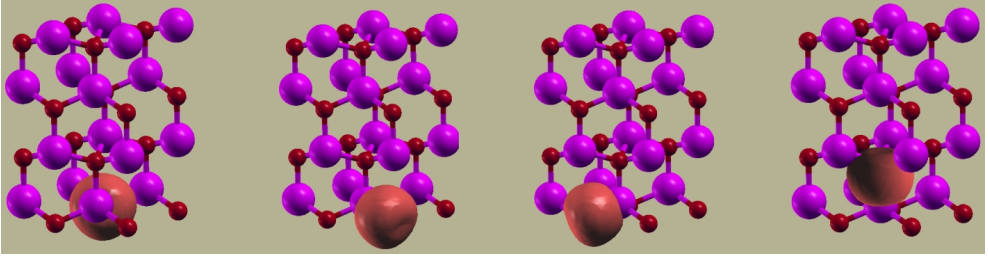


**Figure 3.15:** The  $sp^3$  hybridization in the WZ structure of ZnO represented by maximally localized Wannier functions.

### 3.3.2 Electronic Structure and Equilibrium Properties

In the hexagonal lattice of ZnO, the tetrahedral coordination gives rise to polar symmetry. This polarity is responsible for a number of the properties of ZnO, including piezoelectricity and spontaneous polarization, and is also a key factor in crystal growth, etching and defect generation [124,125]. While the absolute value of the spontaneous polarization in a non ferroelectric material has not been directly measured, theoretical calculations indicates a polarization between  $-0.047$  and  $-0.057$  C/m<sup>2</sup> [142]. Cation doping of ZnO has been reported to induce ferroelectric behavior, e. g., Li doping on ZnO [143]. The existence of spontaneous polarization in ZnO allows coupling with external electric fields, which adds a new degree of freedom to tune physical and/or chemical properties. It is worth noting that ZnO displays the largest electromechanical  $d_{33}$  response among known wurtzite semiconductors ( $d_{33} = 9.9$  pC/N for the bulk and  $d_{33} = 12.4$  pC/N for an oriented film [144]), where the  $d_{33}$  coefficient characterizes the  $c$  axis length change upon application of an electric field along the polar axis [145].

Aside from causing the inherent polarity in the ZnO crystal, the tetrahedral coordination is a common indicator of  $sp^3$  covalent bonding as represented on Figure 3.15 from the projection of the maximally localized Wannier functions [146] (MLWF) based on first-principles calculations. However, the Zn–O bond possesses a very strong ionic character, placing it on the borderline between covalent and ionic classifications, with an ionicity of  $f_i = 0.616$  on the Phillips ionicity scale [147]. A quite recent study of bonding mechanism of ZnO from first-principles methods demonstrated that the charge transfer between Zn and O increases under isotropic pressure resulting into higher ionicity for the RS polymorph [148].

A major driving force of research on ZnO as semiconductor material is its prospective use as a wide band gap  $n$ -type semiconductor for light emitting devices and for high temperature electronics [124,125]. In this respect, an accurate knowledge about its band structure becomes essential. Despite the significant interest in ZnO fundamental electronic properties, few spectroscopic studies of the full band structure exist [142]. Very recently, soft X-ray emission and absorption spectroscopy of the O K-edge were employed to investigate the electronic structure of wurtzite ZnO [149]. Sensitive measurements of the ZnO shallow core level and valence-band dispersion

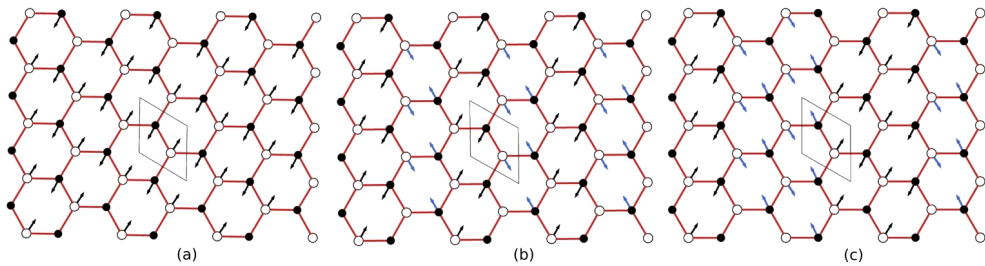


**Figure 3.16:** Hexagons deformation in the hexagonal network in WZ ZnO parallel to (001) according to (left)  $Cmc2_1$ , (middle)  $Pna2_1$ , and (right) the simplest combination of both.

have been performed in order to overcome the difficulty imposed by the close proximity of the  $3d$  levels to the O  $2p$ -derived valence band, which represent a computational challenge for band calculations [142].

On the theoretical side, band gap estimation problem is common for semiconductors and in particular for ZnO where the DFT–LDA gives a poor estimation of 0.8 eV compared to an experimental value of 3.4 eV [140, 142, 149–151]. The electronic structure of ZnO using DFT–GGA method only marginally differs from that of DFT–LDA [75, 140]. In order to circumvent the shortcomings of the DFT–LDA (and LDA–GGA) approach, different types of methods like quasiparticle calculations [150] in the  $GW$  approximation, hybrid functionals [140], DFT–LDA+U scheme [151], and different strategies for pseudopotential generation have been employed in order to gain more accuracy in the determination of the band gap and its nature.

The band structure of the wurtzite ZnO reproduced within the  $GW$  approximation indicate a direct band gap of 3.15 eV, in good agreement with experiments (3.4 eV) [149, 150]. The high pressure phase B1, however, has an indirect band gap between the point on the high symmetric line  $\Sigma$  and the bottom of the conduction band. The direct band gap at  $\Gamma$  is about 4.74 eV and the indirect one is about 4.51 eV. Using *ab initio* correlated Hartree–Fock method, Jaffe *et al.* [152] reported the values of 6.54 eV and 5.54 eV for the latter band gaps respectively. The indirect band gap of RS ZnO may make it suitable for  $p$ -type doping [134]. So far, in the absence of experimental data for the band gap of the RS ZnO, theoretical values have to be verified. The non-metallic behavior is the only indirect indication provided [153]. The calculated direct band gap of ZB ZnO is 3.75 eV, about 0.35 eV higher than the experimental value [154].

### 3.3.3 Phase Transition Models

Because of the similarities between the polymorphism in ZnO and GaN, the transition models that have served as frameworks to study the WZ–RS transition are the same for both compounds, namely, the *tetragonal* ( $iT$ ) and *hexagonal* ( $iH$ ) paths.

For ZnO, three fundamentally distinct mechanisms have been proposed by Sowa [101, 103, 155] for the B4–B1 transition as a deformation of a heterogeneous sphere packing

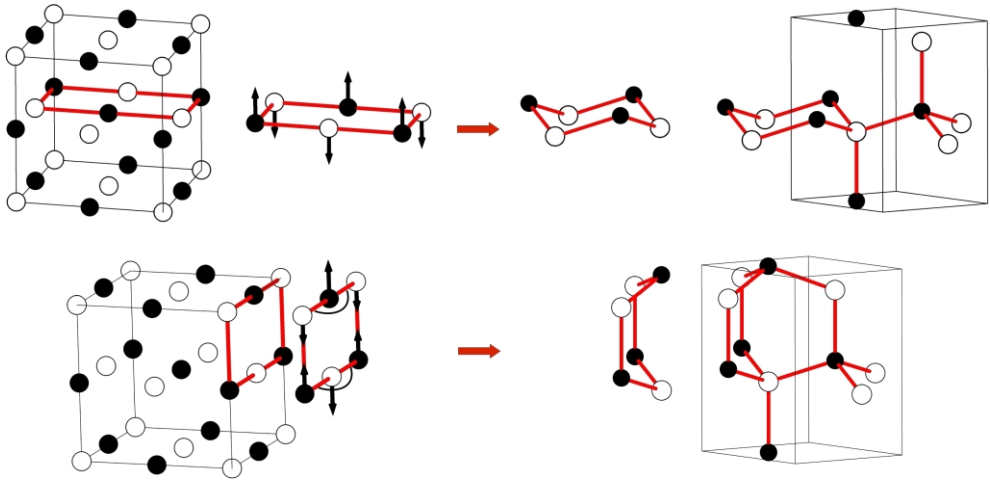


**Figure 3.17:** Schematic drawing of two possible Peierls distortions: chair-type (upper) and boat-type (lower) for the RS (left)  $\rightarrow$  WZ (right) transformation.

using symmetry arguments deduced from orientation relations between WZ and RS phases. The first model implies atomic positions mapping through space group  $Cmc2_1$  (Figure 3.16a), while the second is modeled according to  $Pna2_1$  (Figure 3.16b). By combining these two transition mechanisms, several further pathways can be derived like the one displayed on Figure 3.16c.

Along the line of symmetry-based methods, Capillas *et al.* [104] tried to mimic the strain by imposing symmetry and structural conditions to define maximal symmetry transition paths for the WZ–RS transformation. This yielded a large set of possible pathways classified orthorhombic ( $Cmc2_1$ ,  $Pna2_1$ ,  $Pmn2_1$ , and  $Pmc2_1$ ) and monoclinic ( $Cm$  and  $Pc$ ). Unfortunately, the method can not distinguish between paths through  $Cmc2_1$ ,  $Pna2_1$ , and  $Pc$ .

Using a first-principles pseudopotential method, the transformation enthalpy barrier at the phase equilibrium transition pressure has been calculated for the  $Cmc2_1$  path [156]. No direct comparison to the two other mechanisms was provided, though. By means of molecular dynamics simulations, Shimojo *et al.* [102] investigated the same 3 models proposed by Sowa [101, 103, 155]. The calculated transition barriers, however, turned to be equal in all three mechanisms.

The opening of a band gap under pressure suggested the use a Peierls distortion to describe the WZ–RS transformation in ZnO nanoparticles in terms of chair/boat–type distortion [138] as illustrated in Figure 3.17. However, electronic aspects of the two speculated deformation modes were not clearly determined.

Elastic, acoustic, and optic properties of ZnO have been subject of intense investigation in both experiments and theory [106, 157–162]. Precisely, the softening of these properties under pressure was used to determine vibrational distortions that would eventually lead to continuous transformation models with least costly cross-

ing of the transition enthalpy barrier. The knowledge of elastic, acoustic, and optic properties behavior is necessary to make correct predictions about the stability of different phases under given conditions of temperature and pressure [80, 163, 164]. Such analysis is, however, rigorously justified only for second order transformations. The reconstructive nature of first order transition in ZnO makes the nucleation and growth of the RS within WZ phase difficult to explain and justify from such an approach.

### 3.3.4 Wurtzite-to-Rocksalt (B4-B1) Phase Transition

In order to fully account for the relevant aspects of the reconstructive phase transformation in ZnO under pressure, we employ the simulation strategy as described in Chapter 2 and Section 3.1.4 for GaN.

The only prerequisite of the simulation strategy is at least one initial trajectory connecting both phases, WZ and RS. We derived such trajectory using putative intermediate structures obtained from geometric-topological modeling based on transforming periodic nodal surfaces (see Section 3.1.4).

The mechanistic elucidation of the WZ–RS transformation in ZnO develops along the investigation of the relevance of intermediate configurations, referred to as  $iT$  and  $iH$ . The ability of starting the TPS iterations from different initial regimes is ensured by the modeling approach. Bypassing intermediate structures,  $iT$  and  $iH$ , enables reliable identification of relevant stages of the transformation without biasing the mechanism analysis.

TPS simulations have been performed on ZnO box of 1536 atoms interacting according to the empirical force field parameterized by Binks and Grimes [165] based on Lewis and Catlow model [166]. While temperature was kept equal to 300 K, different pressure values ranging from 9 to 15 GPa have been used for different sets of TPS runs in order to explore the effect of pressure on the transition mechanism and the stability of different intermediates and atomic patterns during the transformation.

The collective atomic motion characterizing the initial regime is very quickly lifted in favor of a different regime dominated by coexistence of structural motifs (Figure 3.18). The first indication of decorrelation in the trajectory regime from the geometric modeling is the setup of a layer shearing mechanism (Figure 3.18a-c). Within  $(001)_{B4}$  layers, adjacent hexagons are deformed into squares. Locally, hexagons can be compressed either along  $[120]$  or  $[210]$ . On a larger scale, the combination of these two fashions pins  $(001)_{B4}$  layer shearing direction along  $[110]$ . The high pressure phase B1 sets in as a slab (Figure 3.18, at  $t = 2$  ps). Further growth is achieved perpendicularly to the direction of the shearing (Figure 3.18, at  $t = 8$  ps). Therein, the intermediate tetragonal structure  $iT$  (space group  $I4mm$ ) appears at the interface between the RS phase and the rest of the transforming WZ phase. The transition sequence can be written as  $B4-iT-B1$ .

The overall reconstruction of  $(001)_{B4}$  layers consists of a combination of parallel and antiparallel layer displacements along  $[110]$  in a zigzag fashion. This mechanistic feature is presented on Figure 3.18a-c, therein, the shearing direction is highlighted using long black arrows (Figure 3.18a). Such combination releases excessive strain caused during the phase transition with respect to a mechanism where all hexagons are compressed along a unique direction (either  $[210]$  or  $[120]$ ). Consequently, the  $[100]$

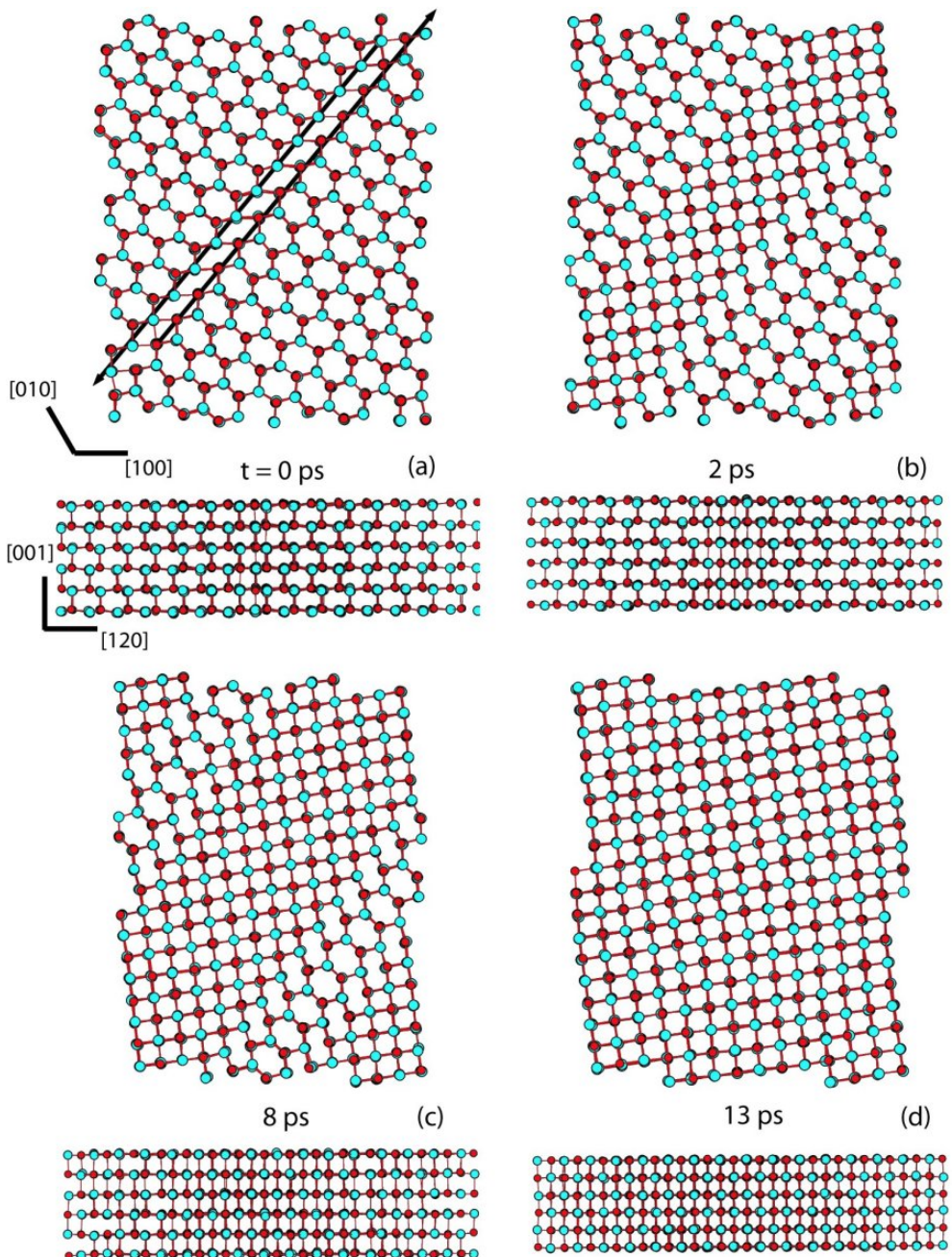


**Figure 3.18:** Snapshots taken from a representative trajectory corresponding to the favorable transition mechanism of WZ-RS transformation in bulk ZnO. Transition is initiated by  $(001)_{B4}$  layers shearing (direction marked by black arrows). Further growth of high pressure modification, RS, is developed perpendicular to shearing direction, until transition is completed.

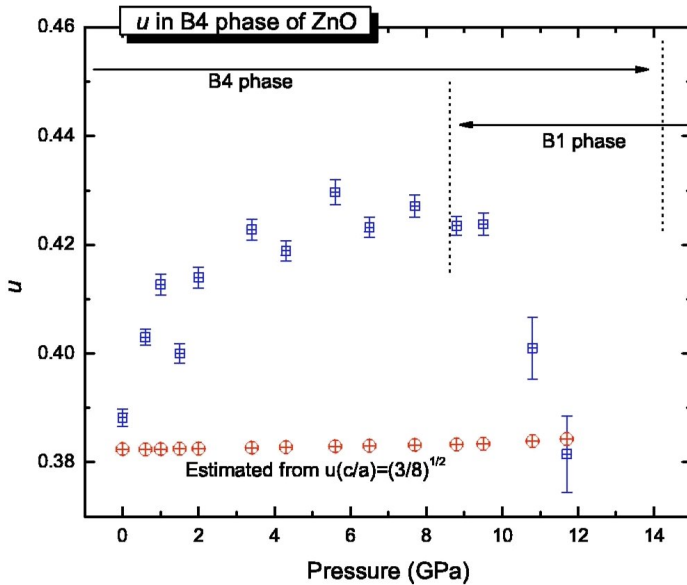


**Figure 3.19:** The internal structural parameter  $u$  of WZ ZnO as a function of pressure. The parameter  $u$  is the  $z$  coordinate of atom in position  $2(b)$  and corresponds to the cations and anions sublattices spacing.

direction in the rocksalt like structure is no longer parallel to  $[100]$  in the wurtzite. The angle spanned by the two directions ( $[100]_{B4}$  and  $[100]_{B1}$ ) after transformation was found to be  $\sim 15^\circ$ .

During high-pressure X-ray investigation of ZnO single crystals conducted by Sowa and Ahsbahs [155], after transition to the RS phase, the single crystals were destroyed and a highly oriented powder was obtained. The observed orientation relations between the unit cells of the WZ and RS phase indicate that one of the fourfold axes of RS of each RS ZnO crystallite is tilted about the  $15^\circ$  against the original  $[001]_{B4}$ . The other two fourfold axes are inclined by about  $5^\circ$  and by about  $15^\circ$  against the original  $(001)_{B4}$ .

Although the accordance between TPS MD simulations and the experiments about the macroscopic change in the morphology of ZnO phases before and after compression, the atomistic details of the mechanism from our simulations differ from those proposed by Sowa and Ahsbahs [155] using orientation relations. Using the space group  $Cmc2_1$ , they derived a continuous, collective, and homogeneous deformation path going through the hexagonal  $iH$  intermediate. This suggestion has been predicted from *ab initio* calculations [100]. Besides, in a recent Rietveld refinement study of WZ ZnO performed by Liu *et al.* [135], on the pressure dependence of the internal parameter  $u$ , the authors are pleading in favor of the following transformation sequence:  $B4-iH-B1$ . Using high-resolution angular dispersive X-ray diffraction up

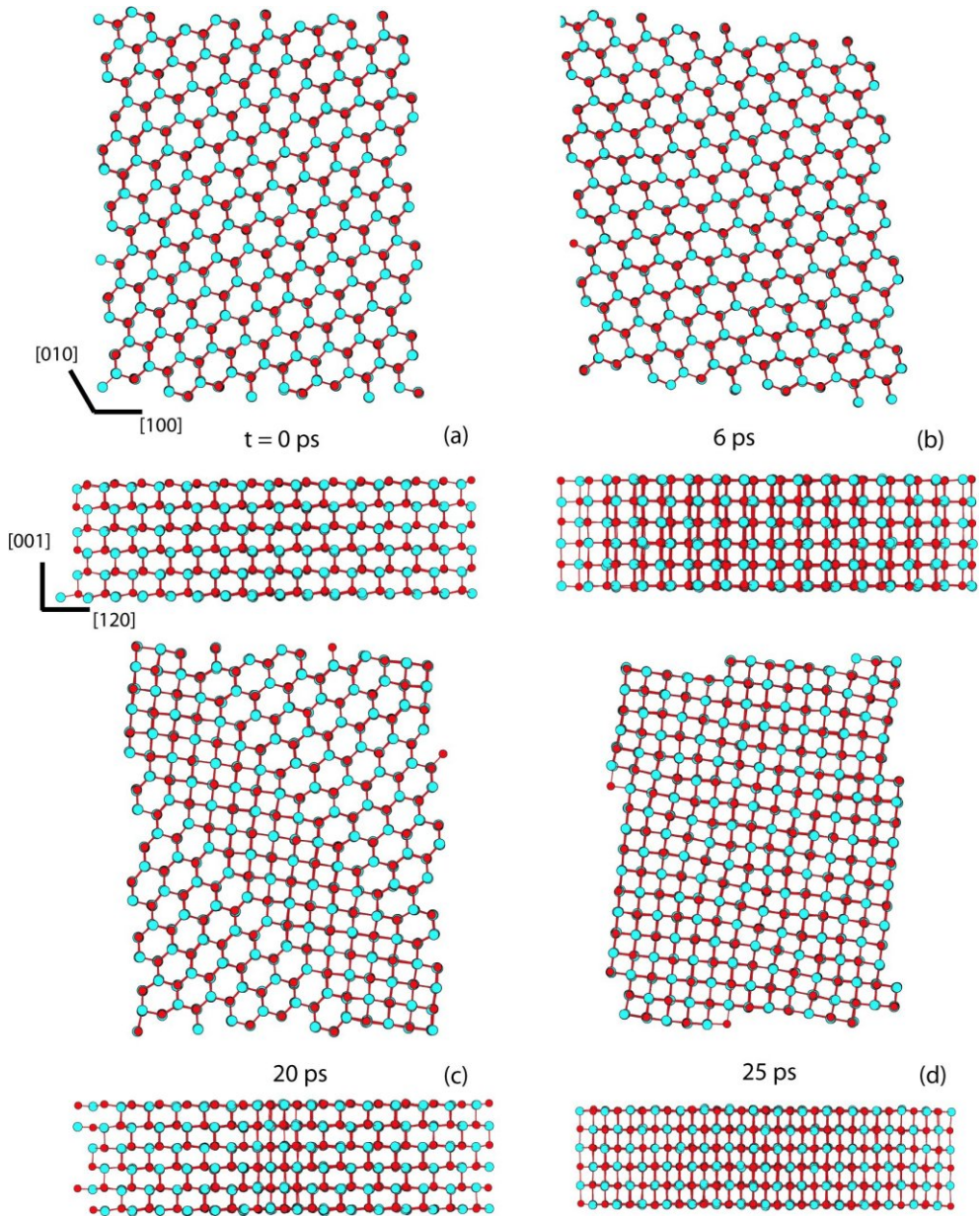


**Figure 3.20:** Snapshots taken from a trajectory corresponding to a less-favored transition path going through hexagonal  $iH$  intermediate (b). Before layers shearing is initiated (c), the system is compressed along  $[001]_{B4}$  and  $iT$  is formed (a)-(b). As soon as WZ reconstruction is started, the system is again relaxed into WZ structure (b)-(c).

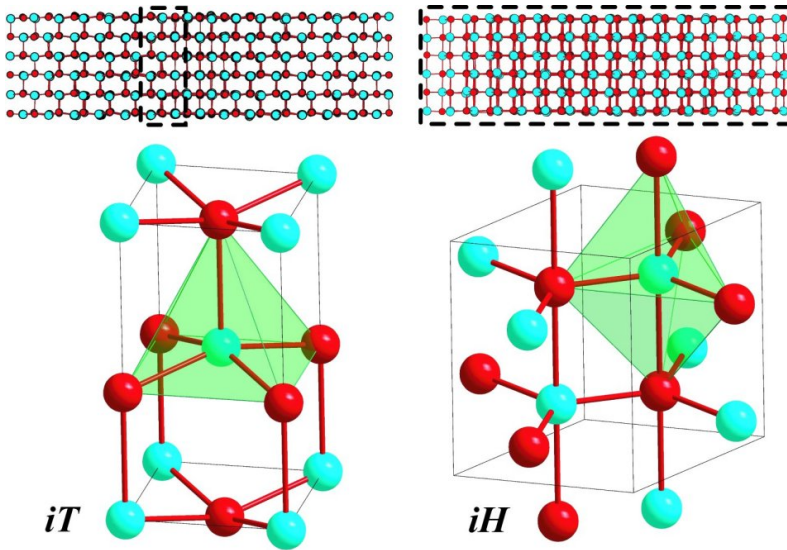


**Figure 3.21:** Intermediate motifs  $iT$  (left) and  $iH$  (right) appearing during distinct TPS simulation runs with corresponding structural extents during the transformation (upper panel).

to 12 GPa (Figure 3.19<sup>4</sup>), the structural parameter  $u$  is found to increase with pressure. The increase in the value of  $u$  is an indicator of the first step in the orthorhombic path going through  $iH$ .

This apparent discrepancy can be resolved considering the complete set of reactive pathways collected in the course of simulations. Therein the relevance of a mechanism is related to the probability of finding corresponding dynamical pathways.

In the course of TPS iterations, transition trajectories cross different regimes before the more probable favorite one sets in. Mechanisms corresponding to the decorrelated trajectory regime share the same  $(001)_{B_4}$  layer shearing features as shown on Figure 3.18. However, different intermediate structures may occur during transformation, depending on the peculiar evolution of independent TPS runs, which started from distinct first trajectories. We recall that both intermediate structures ( $iH$  and  $iT$ ) were bypassed on purpose during the generation of the first trajectory and that their appearance reflects a preference of the system, not an external bias. Therefore, from the collected trajectories, we can learn about the reason of their spontaneous emergence. Either  $iH$  or  $iT$  is formed by a different synchronization of the variation of relative spacing  $u$  between cations and anions sublattices with  $(001)_{B_4}$  layers shearing. If the compression along  $[001]_{B_4}$  occurs during or after the  $(001)_{B_4}$  layers reconstruction, the hexagonal intermediate  $iH$  is ruled out and the system crosses over directly to the tetragonal  $iT$  intermediate; otherwise, a compression along  $c$  axis prior to the shearing leads to the hexagonal intermediate.

<sup>4</sup>Figure taken from Ref. [135]



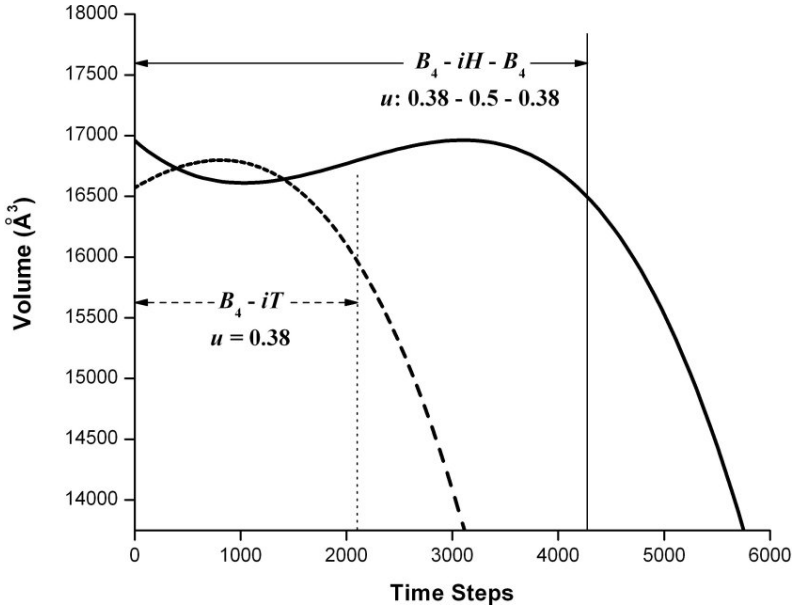


**Figure 3.22:** Volume variation profiles of transition paths visiting the  $iH$  (continuous line) or bypassing it (dashed line).

A representative intermediate regime, appearing during TPS iterations and characterized by  $iH$  crossing, is shown in Figure 3.20. Therein, on the eve of  $(001)_{B_4}$  layers reconstruction, a change in the structure occurs (Figure 3.20a-b). The  $B_4$  phase is compressed along  $c$  axis such that new contacts appear all along. The atoms are *quasicollectively* displaced parallel to  $[001]_{B_4}$  and the whole system is converted into a hexagonal fivefold intermediate structure  $iH$  (Figure 3.21, right, and Figure 3.20b). The internal parameter  $u$  changes from 0.38 to 0.5. However, as soon as the reconstruction of  $(001)_{B_4}$  layers resumes, atoms regain their initial positions within the wurtzite structure under the reversal of the  $B_4 \rightarrow iH$  transformation. The value of  $u$  is again 0.38 when the rocksalt phase starts forming. With respect to the layer shearing modes, which are productive toward lattice reconstruction into RS ( $B_1$ ), the details of the transition are the same as shown in Figure 3.18 and as described above. This discloses a scenario of fluctuation of  $u$  close to the phase transition.

Indeed, Liu *et al.* [135] showed that the increase in the structural internal parameter  $u$  is observed up to  $\sim 9$  GPa with a maximal value  $u = 0.43$  at around 5.6 GPa, well below the critical pressure of 10 GPa and before the appearance of the RS phase. As the latter starts to form, the parameter  $u$  shows a sharp decrease to its value of 0.38. This reversible pretransitional effect reported in experiments is well reproduced in our simulations (Figure 3.20).

The  $B_4$ – $B_1$  phase transition in ZnO is accompanied by a large volume collapse of  $\sim 20\%$  [159]. Considering the profile of the volume evolution associated with paths

containing the  $B4-iH$  pretransitional step (Figure 3.22, continuous line) or directly crossing over to the RS (B1) through the  $iT$  intermediate (Figure 3.22, dashed line), the former allows for a slightly higher maximum. The associated  $[001]_{B4}$  compression implies a comparatively smaller orthogonal expansion. The cell and volume evolution anisotropy, which is difficult to trace in experiments [160], can nonetheless be investigated in the simulations. The occurrence of the  $iH$  structural pattern results into longer transition paths, 25 ps instead of 13 ps. Increasing pressure above 10 GPa shortens the length of trajectories and alters completely the pretransitional step  $B4-iH$  in favor of the  $B4-iT-B1$  path, with an overall volume variation similar to the dashed curve of Figure 3.22. This supports an interpretation of the  $iH$  intermediate as controlled by a fluctuation of the parameter  $u$  close to phase transition and corresponding to different responses of the system to external pressure loadings.

The simulation can access regions of intermediate pressures, where concurring deformation modes can be initiated. Clearly, only one mechanism is productive with respect to transforming the system from B4 to B1. Nonetheless, the intermediate regime is far more complex, due to structural motifs and deformation modes coexistence, which accounts for the richness and apparent contradiction of the experimental data. The difference in the elastic response along  $c$  and perpendicular to it—peculiar to ZnO—can be used to predict novel structural patterns, for example, in ZnO nanorods, if an external tensile load is applied [167].

The shift in trajectories regime from the less-favored ( $B4-iH-B1$ ) to the final mechanism ( $B4-iT-B1$ ) is thus marked by a competition between characteristic intermediate structures, hexagonal  $iH$ , and tetragonal  $iT$ . Accordingly, the response of different regions in the system may lead to irregular arrangements. On the reverse transition  $B1 \rightarrow B4$ , the growth of the wurtzite phase is ensured by  $(001)_{B1}$  layers reconstruction into  $(001)_{B4}$  layers (Figure 3.23a-b). The interplay between deformation modes causes the survival of a small island of cubic rocksalt phase (Figure 3.23c), which evolves into an interface parallel to  $[100]_{B4}$  (Figure 3.23c). Therein, rocksalt structure is formed by, in turn, deforming hexagons along  $[210]_{B4}$ . Interface formation along  $[100]_{B4}$  induces 4- and 8-membered rings and defects, persisting in the wurtzite structure after structural relaxation (Figure 3.23f). Similar defects are common in wurtzite growth experiments where domains settle into low-energy configurations with grain-boundary dislocations [168].

To more clarify the relevance of local deformations elucidated from our simulations, we make comparison with other aspects of the transition as revealed by both, experiments and theory, on the elastic, acoustic, and optic properties under pressure [106, 157–162].

Phase transitions induced by temperature or pressure are often associated with different optic and elastic instabilities. Although the first-order pressure-induced  $B4-B1$  transition cannot be carried by a single mode, becoming soft across the transition, shear modes and phonon modes softening appear as precursors to structural transformation in ZnO [79, 157, 159].

For the ZnO wurtzite phase, at the  $\Gamma$  point of the Brillouin zone, group theory predicts the existence of the following optic modes:  $\Gamma_{opt} = A_1 + 2B_2 + E_1 + 2E_2$  as illustrated on Figure 3.24.  $A_1$ ,  $E_1$ , and  $E_2$  are Raman active. In addition,  $A_1$  and  $E_1$  are active, and therefore split into longitudinal and transverse optical (LO and TO)

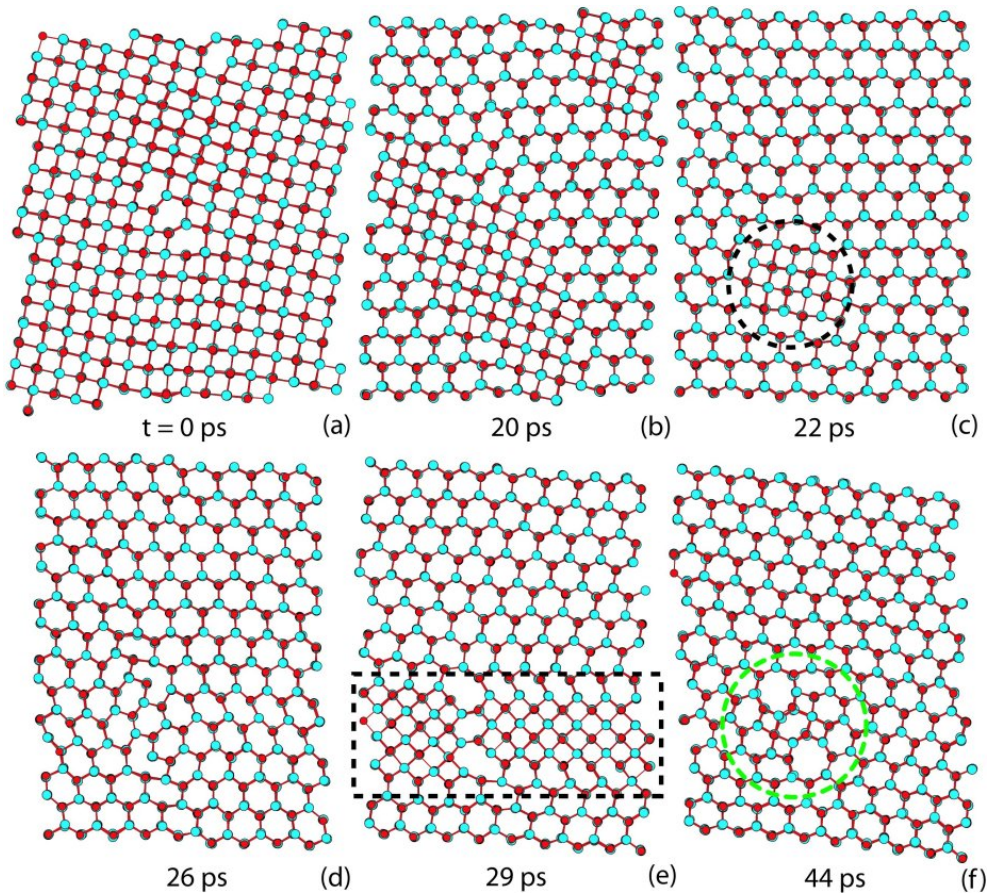


**Figure 3.23:** Defects formation due to intermediates competition during a B1→B4 transition. (a)-(b) The reverse transition, B1→B4, is achieved via layers shearing. Competition between intermediate structures,  $iH$  and  $iT$ , caused the survival of RS island (c). Local resolution of RS fraction resulted into defects (d)-(f).

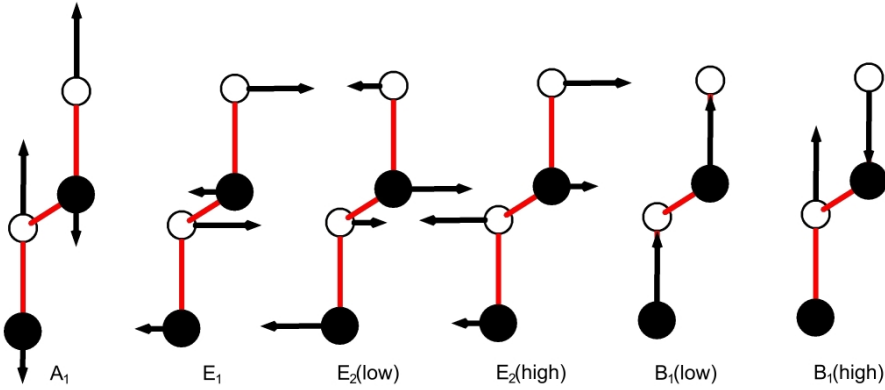


**Figure 3.24:** Scheme of the displacement vectors associated with the six different phonon modes of WZ ZnO at the  $\Gamma$  point.

components [157, 169].

The atomic displacements and structural changes leading to the intermediate structures  $iH$  and  $iT$  can be associated with vibrational modes in WZ ZnO getting soft under the effect of pressure. The  $c_{44}$  and  $c_{66}$  shear modes and  $E_2^{low}$  optic mode are associated with the displacements of the B4- $iT$  branch [106]. While,  $E_2^{high}$  and  $A_1$  modes are supposed to soften in order to allow for the B4- $iH$  deformation [100].

A high-pressure Raman spectroscopy study of WZ ZnO conducted up to 10 GPa shows an increase in frequency shift of  $E_2^{high}$ ,  $A_1$ (TO),  $E_1$ (TO), and  $E_1$ (LO) modes with pressure, with no anomaly detected up to transition pressure [157]. This result invalidate theoretical predictions [100] of instability in the previous modes arising from a WZ  $\rightarrow$   $iH$  transition. This agrees with the conclusions derived from X-ray experiments, where the evaluation of the normalized intensity of the (002) and (101) diffraction lines indicated no deviation of the  $u$  parameter from its ideal value [133]. On the other hand,  $E_2^{low}$  is the only mode which exhibit a negative pressure dependence with a Grüneisen parameter that shows a negative value of  $-1.6$ .

In fact, this instability, together with the softening of shear modes  $c_{44}$  and  $c_{66}$  under pressure, reported from experiments [159] and confirmed using *ab initio* calculations [162], is consistent with the monoclinic deformation allowing for  $\gamma$  angle in WZ ZnO to vary, which leads to the  $iT$  structure.

In summary, we performed molecular-dynamics simulations in combination with transition path sampling on the pressure-induced B4-B1 phase transition of zinc oxide. The transition from the hexagonal wurtzite to cubic rocksalt structures is achieved via layer shearing over a tetragonal intermediate structure appearing at the interface between B4 and B1 structures. In the intermediate region of the transition, a hexagonal intermediate  $iH$ , isostructural to hexagonal  $h$ -BN, may appear before the reconstructive step as a result of stress fluctuations reflected in changes of the parameter  $u$  which corresponds to the cations and anions sublattices spacing. The latter is in very good agreement with an experimental evidence of its evolution under pres-

sure. The details of the mechanism are in accordance with experimental observations on sample orientation as well as spectroscopy evidence of shear and phonon modes softening under pressure. Within a scenario of competing deformation modes close to phase transition, the possible occurrence of different intermediates is explained, reconciling many experimental observations. The coexistence of deformation modes connected with both  $iT$  and  $iH$  intermediates may trap B1 islands within B4 during B1-B4 back transformation and is responsible for the formation of structural defects within B4. An articulated, yet consistent mechanistic elucidation is the overall result of this section about phase transition in ZnO.

---

# 4 Phase Transitions in Superionic Materials

---

## 4.1 Calcium Fluorite, CaF<sub>2</sub>

Transformation processes between liquid and solid phases are phenomena of central importance in nature. The most fundamental transition of this kind is represented by a crystallization from the melt. While this is one of the main synthetic routes in solid state synthesis, a more peculiar phenomenon is reflected by superionic conductors, a fascinating blend of solid and liquid states that arises when only parts of a compound become liquid. In CaF<sub>2</sub>, representative of the class of fluorite-structured fast-ion conductors, the fluoride sublattice is well known to melt on raising temperature, giving rise to a superionic transition. If such phenomenon is observed on varying temperature, how about the effect of high pressure.

In the present part, we aim at demonstrating pressure as an important thermodynamic variable governing sublattice melting in CaF<sub>2</sub>.

### 4.1.1 Polymorphism

CaF<sub>2</sub> or *fluorite*, has one of the basic crystal structure types in the solid state. At ambient conditions, it crystallizes in a face-centered cubic structure that belongs to the space group  $Fm\bar{3}m$ , with four atoms in the unit cell ( $Z = 4$ ) (Figure 4.1, left). The experimental lattice parameter is  $a = 5.463 \text{ \AA}$  [170], with Ca<sup>2+</sup> and F<sup>-</sup> ions located at (4a) (0,0,0) and (8c) ( $\frac{1}{4}, \frac{1}{4}, \frac{1}{4}$ ), respectively.

The cation sublattice is a cubic close-packed (*ccp*) arrangement of edge-sharing tetrahedra. The anion sublattice, however, is made up of edge-sharing cubes. The interpenetration of both sublattices leaves the octahedral voids, centered at ( $\frac{1}{2}, \frac{1}{2}, \frac{1}{2}$ ), empty, as illustrated on Figure 4.1, left side.

Under high pressure, the polymorphism of CaF<sub>2</sub> is extended to encompass another phase, the orthorhombic polymorph (cotunnite, PbCl<sub>2</sub> type, space group  $Pnma$ ,  $Z = 4$ ) [170]. In the high-pressure modification, the array of cations is hexagonal close-packed (*hcp*) with all Ca<sup>2+</sup> ions in nine-coordination with fluorine, in tricapped trigonal prisms. F<sup>-</sup> ions are equally distributed over two interstitial sites offered by the cation sublattice, tetrahedra and square-based pyramids, in fourfold and fivefold

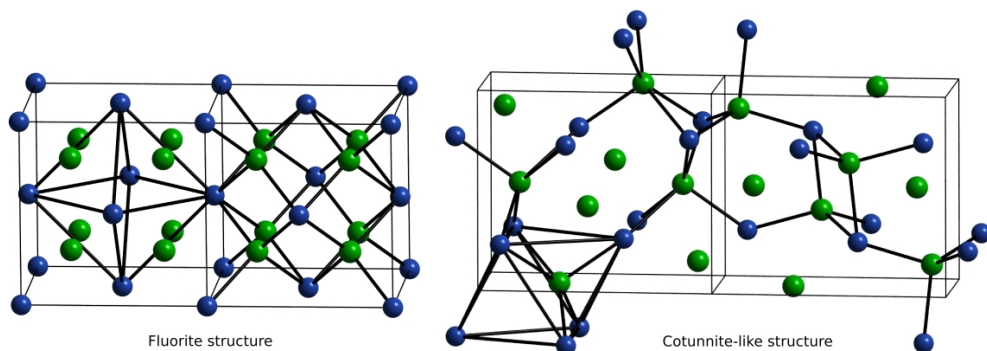


**Figure 4.1:** CaF<sub>2</sub> polymorphs: the ambient conditions fluorite structure (left) and the high-pressure modification PbCl<sub>2</sub>-type structure cotunnite (right). Structures are shown in double unit cells.

coordinations, respectively (Figure 4.1, right).

Crystallographic data determined from experiments give the following values:  $a = 6.018 \text{ \AA}$ ,  $b = 3.614 \text{ \AA}$ , and  $c = 7.023 \text{ \AA}$  as cell parameters, with all ions in positions  $4(c)$   $(x, \frac{1}{4}, z)$ , Ca:0.2539,0.25,0.1094 – F(1):0.8595,0.25,0.0731 – F(2):0.4780,0.25,0.8344 [170].

The pressure-induced fluorite-cotunnite phase transformation in CaF<sub>2</sub> has been reported to occur in the pressure range of 8–10 GPa [171]. This observation was confirmed by many experiments using different techniques, such as X-ray diffraction, Raman spectra and theoretical calculations [172–178]. Recently, the kinetics of the transition in CaF<sub>2</sub>, including initial stages, have been investigated in details by means of the gauge technique under hydrostatic pressure at room temperature, indicating a transition pressure is equal to  $8.01 \pm 0.01 \text{ GPa}$  [177]. The high-pressure phase of CaF<sub>2</sub> has been shown to be stable up to 49 GPa at room temperature using X-ray diffraction and Raman spectra [173, 175]. Upon decompression, however, the transition is reversible and the PbCl<sub>2</sub> type structure is reverted back to the fluorite structure. Morris *et al.* [170] demonstrated the possibility to grow single crystals of cotunnite structure of CaF<sub>2</sub>, at 8.6 GPa and 1100 K in a molten Ca(OH)<sub>2</sub> flux, which are stable at ambient conditions.

The fluorite (CN(Ca)=8) and cotunnite (CN(Ca)=9) structures are also realized by the fluorides of heavier alkaline-earth metals (Sr, Ba). The series of high-pressure structures for AB<sub>2</sub> composition is enriched by a plethora of other phases like EuI<sub>2</sub> and  $\alpha$ -PbO<sub>2</sub>, on varying the halogen moiety, like in CaCl<sub>2</sub>, or in oxide compounds like ZrO<sub>2</sub>. Despite the chemical diversity of these compounds, the analogies in their high-pressure behavior, in particular the appearance of the same atomic pattern among high-pressure polymorphs, hints at common features.

For CaF<sub>2</sub>, three candidate phases are considered for the post-PbCl<sub>2</sub> transition: the Co<sub>2</sub>Si structure ( $Pnam$ , CN=10) [179], the distorted Co<sub>2</sub>Si structure ( $P2_1/a$ , CN=10) for ACl<sub>2</sub> ( $A=\text{Pb, Ba, and Sn}$ ) [180], and the Ni<sub>2</sub>In structure ( $P6_3/mmc$ , CN=11) for AF<sub>2</sub> ( $A=\text{Pb and Ba}$ ) [181].

The high-pressure behavior of  $\text{BaF}_2$  and  $\text{PbF}_2$  has been extrapolated on that of  $\text{CaF}_2$ , namely in the possible occurrence of the  $\text{Ni}_2\text{In}$  structure at extreme pressures. Using *ab initio* calculations, Wu *et al.* [182] predicted the  $Pnma \rightarrow P6_3/mmc$  transition to occur at a pressure in the range 68–72 GPa, with a volume collapse of  $\sim 2.5\%$ . The transition sequence  $Fm\bar{3}m \rightarrow Pnma \rightarrow P6_3/mmc$  was proposed with an increase of the cation coordination number from 8 to 9, then 9 to 11. However, none of the proposed post- $\text{PbCl}_2$  phases of  $\text{CaF}_2$  was characterized in experiments.

### 4.1.2 Electronic Structure and Equilibrium Properties

$\text{CaF}_2$  is an ionic compound that has attracted special attention as a lens material for lithography in the deep ultraviolet region at 157 nm [183]. It offers excellent transmission properties without absorption bands over a wide wavelength range from UV to IR. These optical properties are related to its structural and electronic properties, such as a very large band gap. In addition,  $\text{CaF}_2$  is proposed to have an excellent internal pressure calibration in moderate high-pressure or high-temperature X-ray diffraction experiments [182].

From the experiments, the direct band gap was estimated to 12.1 eV and the indirect gap to 11.8 eV [184, 185]. On the theoretical side, the use of DFT calculations within both, LDA and GGA approximations, leads to an underestimation of the band gaps of  $\text{CaF}_2$  by several eV [183]. The calculated indirect band gap along  $X-\Gamma$  is typically within the range of 6.5–7.5 eV. An error of a factor of 2 is typical. In order to remedy this failure, quasiparticle band structure calculations have been carried out within the GW approximation of the electron self-energy operator [183]. Although computationally demanding, these calculations give a good estimation of the band gap (11.5 eV), in good agreement with experiments.

While the electronic properties of the ambient conditions phase, fluorite, have been studied from both experiments and theory, only a few works have been devoted to investigate the influence of pressure on electronic and optical properties of  $\text{CaF}_2$ . Recent first-principle calculations [176, 178] aiming at the determination of the pressure dependence of the band gap show an increases in its value on increasing pressure.

The fluorite-to-cotunnite phase transition causes a change from indirect to direct band gap. On further compression, the gap was expected to close and a band overlap metallization to occur around 210 GPa [176, 178]. The theoretical calculations conducted by Wu *et al.* [182], however, predicted no metallization up to 218 GPa. The band gap was calculated to change from indirect ( $X-\Gamma$ ) to direct during the first transition ( $Fm\bar{3}m \rightarrow Pnma$ ). Then, again from direct to indirect ( $\Gamma-K$ ) during the second one ( $Pnma \rightarrow P6_3/mmc$ ).

Another interesting property of  $\text{CaF}_2$  is its ionic conductivity. In general, ionic conductors are promising candidates for solid-state electrolytes which can be used in batteries.  $\text{CaF}_2$  is a prototype ionic conductor showing a strong increase of the conductivity with temperature that saturates at 1420 K [186], where it becomes comparable to that of a molten salt; the melting temperature is near 1690 K. [187]. Despite considerable efforts, the origin of the ionic transport is not completely clarified in  $\text{CaF}_2$ . Motional disorder in the fluorine sublattice, hopping over potential barriers, and the formation of various types of defects are certainly essential ingredients for



ionic conduction [188]. Details of the conduction mechanism, however, depend on peculiarities of the structure and dynamics [187].

In order to contribute to the general understanding of ionic conduction and to shed light on difficult aspects of structure reconstruction between the fluorite and the cotunnite phases, we have performed simulations on the corresponding transition, revealing the microscopic details of the atomic motion and local rearrangements and deformations.

### 4.1.3 Crystallographic Aspects of The Phase Transition in CaF<sub>2</sub>

In CaF<sub>2</sub>, as well as many other similar systems (PbF<sub>2</sub>, BaCl<sub>2</sub>, SrF<sub>2</sub>, BaF<sub>2</sub>, CdF<sub>2</sub>, MnF<sub>2</sub>, ZrO<sub>2</sub>, and CeO<sub>2</sub>), the high pressure modification exists in a very narrow range. This is evident from values of axial ratios  $a/b$  and  $c/b$  of the cotunnite ( $1.605 < a/b < 1.689$  and  $1.942 < c/b < 1.998$ ). Compared to those expected for ideal hexagonal close-packing of the Ca<sup>2+</sup> ions ( $a/b \sim 1.633$  and  $c/b \sim 1.732$ ). The  $c/b$  ratio is 10% higher, indicating a distortion as a lengthening along  $c$  relative to  $a$  and  $b$ .

The volume change accompanying the fluorite to cotunnite phase transition as determined from experiments is  $\sim 7\%$  [170]. This is a smaller value than is observed for many high-pressure transitions involving coordination change. This was attributed to the small increase in neighbors number, 8 $\rightarrow$ 9, if compared to other examples where the coordination number increases by 2 (4 $\rightarrow$ 6 and 6 $\rightarrow$ 8).

Both the fluorite and the cotunnite structures are based on a close-packed cation lattice, *ccp* and *hcp* respectively. This apparent simplicity introduces another problematic: why is the PbCl<sub>2</sub>-type phase denser if the cation packing in both phases has the same intrinsic density.

In the cotunnite structure, half of the anions are off centers of octahedral sites (Figure 4.1, right). This causes the *hcp* array distortion around the high-coordinated cations. The presence of fourfold anions does not allow for an isotropical distortion of the *hcp*. The symmetry of the compound is dictated by the anion arrangement in an orthorhombic supercell of the primitive *hcp* cation sublattice.

The magnitude of axial deformations is capable to cause a  $\sim 15\%$  volume collapse. However, due to the opposing sense of the  $c$  axis variation, the volume change is smaller.

Unlike most first-order phase transformations, fluorite and cotunnite structures are related in terms of group-subgroup relations, as illustrated in Figure 4.2.

The latter diagram shows the existence of a manifold of possible paths for atomic displacements through different intermediate structures. This symmetry pathways can be divided into two main branches, tetragonal and orthorhombic (Figure 4.1, right and left, respectively).

In the absence of experimental evidence of any of the group-subgroup possible routes, and because of the lack of theoretical studies along this line, we started our simulations from one of these pathways.

The simulation scheme as it is described in Chapter 2, requires the modeling of a first transition trajectory which is subsequently rectified in the course of transition path sampling iterations. Such an initial pathway can be prepared from a geometric-topological approach, as described in Chapter 3 for GaN and ZnO first trajectories

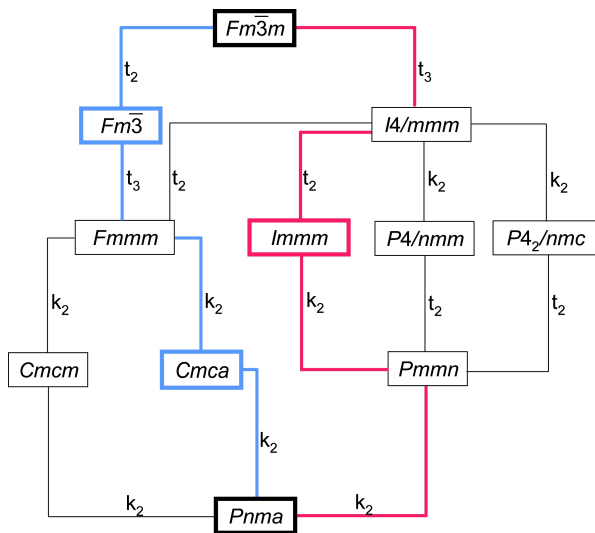


**Figure 4.2:** Group-subgroup relations between the space groups of the fluorite (top) and the cotunnite (bottom) polymorphs of  $\text{CaF}_2$ .

design. In the case of  $\text{CaF}_2$ , we take advantage of the fact that the space group of fluorite ( $Fm\bar{3}m$ ) is connected to the space group of cotunnite ( $Pnma$ ) via several group-subgroups pathways as represented on Figure 4.2.

The distance between the groups allows for several pathways. We have chosen the path from  $Fm\bar{3}m$  to  $Pnma$  over  $Immm$  as a model for the first trajectory. The mapping is associated with the transformation matrix  $[(1 \frac{1}{2} 0)(-1 \frac{1}{2} 0)(0 0 1)]$  with an origin shift  $[\frac{1}{2} 0 \frac{1}{2}]$ .

In a common cell the atomic coordinates were varied between two limiting parameter regions corresponding to the  $\text{CaF}_2$  and  $\text{PbCl}_2$  structural motifs. From these interpolated configurations a dynamical intermediate was derived, and from it a first transition pathway, by propagating in both directions of time. The mechanism we used for preparing the first transition trajectory contained a symmetric intermediate configuration, as it is shown on Figure 4.3b. This intermediate features trigonal prisms of  $\text{Ca}^{2+}$  ions that are formed by the fusion of adjacent tetrahedral on increasing the puckering of the layers of the cubic structure.

While this initial trajectory does not need to be a likely one, more probable routes are more frequently produced, and the trajectory regime quickly departs from the disfavored, symmetric intermediate structure, and shifts towards a preferred mechanistic regime characterized by nucleation and growth. This pathway evolution occurred within 15-20 iterations. From the first dynamical pathway, obtained from the starting model, new trajectories are iteratively produced. A configuration is selected from a previous trajectory, and modified for the next simulation step keeping the total momentum, total energy, and angular momentum unchanged.

Upon propagation of the new configuration in both forward and backward time

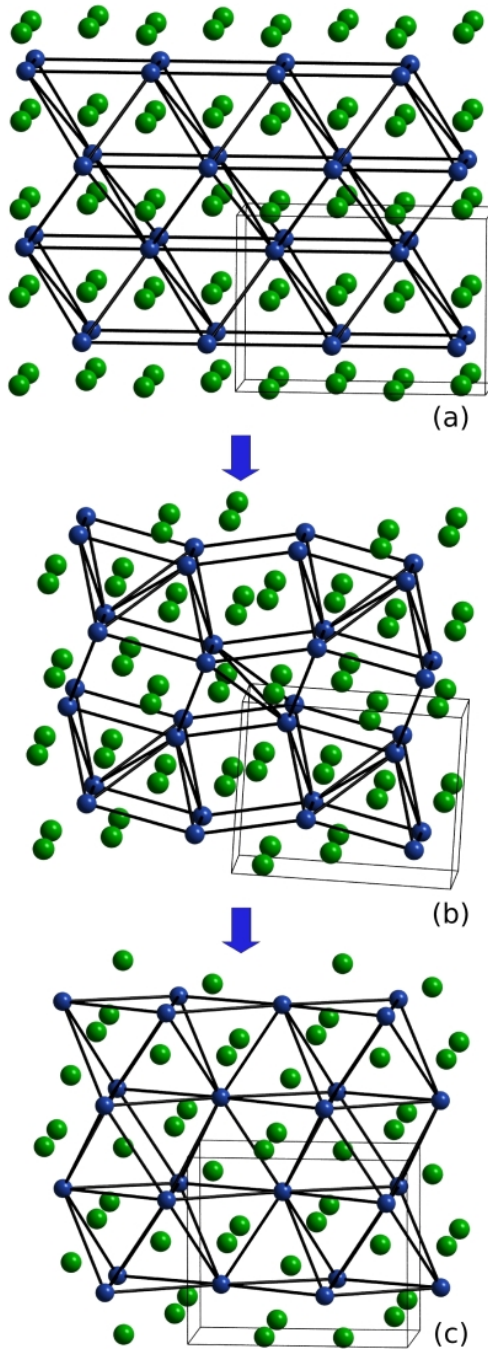


**Figure 4.3:** Geometric model used as a starting transformation route of  $\text{CaF}_2$  from the cubic structure (a) to the orthorhombic (c), over an orthorhombic intermediate structure ( $Immm$ ) (b).

directions, the resulting trajectory is investigated for the fluorite to cotunnite transition.

As a discriminating order parameter between the fluorite and cotunnite structures, the coordination number (CN) of the fluoride ions to the cations is used. A simple statistics of the percentage of anions in coordination 4. The order parameter (OP) should change from 100% in the fluorite to 50% in the cotunnite. To increase the efficiency of the OP we performed another statistics on fivefold fluoride ions. This would change from 0% in the fluorite to 50% in the cotunnite. The simultaneous use of both statistics ensured a good discrimination between  $\text{CaF}_2$  polymorphs.

The simulation box contained 256  $\text{Ca}^{2+}$  ions and twice as many fluoride ions. Inter-ionic interaction were described using a set of empirical force field parameters [189]. For the molecular dynamics simulations, a time step as small as 0.1 fs was chosen, in order to ensure good time reversibility.

The initial simulation pressure was initially chosen as 9.5 GPa, which represents the lower boundary of the hysteresis obtained from experiments [170,171], where the high pressure structure starts forming. Experiments are performed in a temperature range of 300 to 573 K. We performed different sets of simulations at different temperatures (300, 350, 400, 450, 500, and 573 K). The pressure was varied as well between 9 and 12 GPa. Anisotropic shape changes of the simulation box were allowed for not biasing the mechanistic analysis with respect to the experiments. The mechanistic analysis is based on more than 100 transition pathways sampled after decorrelation of the trajectories from the initial, disfavored regime.

#### 4.1.4 Solid-Solid-Solid Regime

The way of reconstructing the cation close-packed hexagonal pattern coded in the starting route (Figure 4.3) disappears during the early iteration steps, and a different mechanism sets in. The latter involves shearing of  $\text{Ca}^{2+}$  (100) layers.

The reconstruction of the Ca sublattice is achieved by shearing of layers along [011] as shown on Figure 4.4, upper panel. In adjacent (100) layers (a  $4^4$  square nets). antiparallel shift of *ladders* of  $\text{Ca}^{2+}$  ions is involved (Figure 4.4, red frames). Consequently, squares are squeezed into triangles, and square nets are rearranged into  $3^3 4^2$  nets with alternation between rows of squares and rows of triangles.

The centers of squares depicted on Figure 4.4, upper panel, coincide with the centers of octahedra. Initially empty in the fluoride structure, as all anions occupy tetrahedral interstitial sites, the situation is different after reconstruction of the cation sublattice. Half of anions are located in square-based pyramids, off centers of octahedral sites.

Cation sublattice reconstruction (Figure 4.4, lower panel) indicates that antiparallel shifts of  $\text{Ca}^{2+}$  *ladders* remove half of the fluorite octahedral voids and generates new ones, with a different orientation in the cotunnite structure (Figure 4.4, blue octahedra). The two new types of octahedral sites are alternating along [0 $\bar{1}$ 1].

The overall reconstruction of the cubic close-packed *ccp* arrangement of cations into a distorted hexagonal close-packed arrangement *hcp* is initiated via a shift of ladders that propagates along [0 $\bar{1}$ 1] in an antiparallel fashion until complete transformation into cotunnite. This *solid* picture of the transition regime, already sufficiently answers to the question: **how** the reconstruction proceeds in  $\text{CaF}_2$ . The important question:

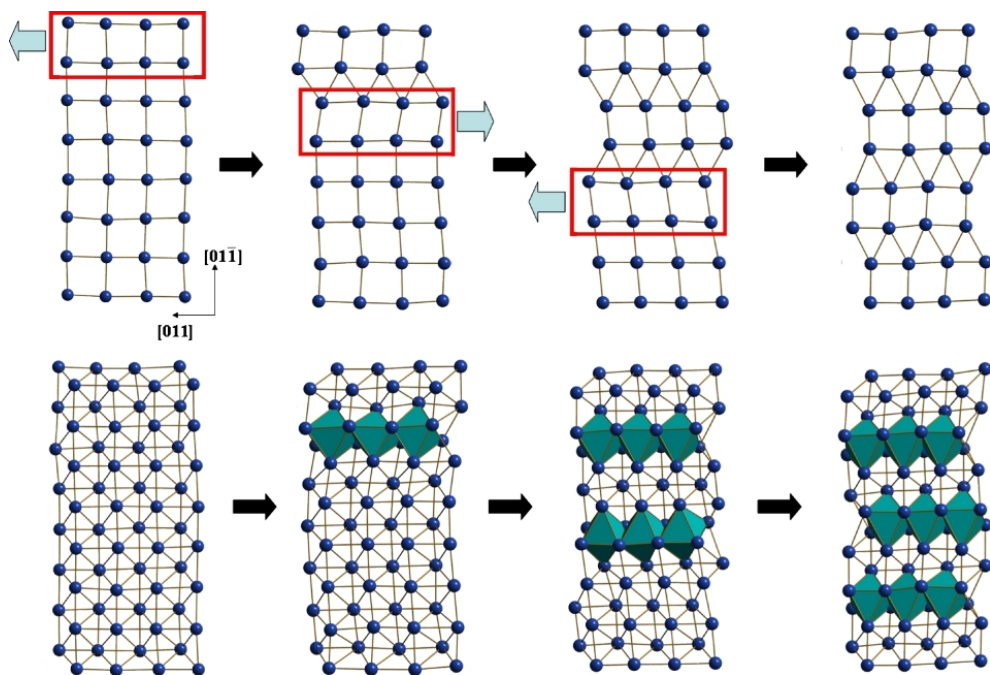


**Figure 4.4:** Reconstruction of the Ca<sup>2+</sup> sublattice via layer shearing along [011]. Antiparallel shifts within adjacent (100) layers in the fluorite causes the reorientation of half octahedral voids highlighted by green polyhedra (lower panel).

**why** the system is being reconstructed according such fashion, remains unanswered. Because the analysis of the cations sublattice reconstruction only provides a part of the mechanism, the anions have to be included, with a focus on early stages of the transition.

#### 4.1.5 Solid-Liquid-Solid Regime

The signature of the onset of the cubic to orthorhombic phase transition in CaF<sub>2</sub> is an enhanced mobility of the fluoride ions (Figure 4.5a-b). While the arrangement of the Ca<sup>2+</sup> ions remains as in the fluorite structure, the F<sup>-</sup> ions can move between different tetrahedral voids, with excursions as long as 650 pm. In the fluorite structure all tetrahedral voids are occupied. Anion mobility is achieved through the creation of a *Frenkel defect*, an episodic occupation of an octahedral void (Figure 4.5a), leaving an empty tetrahedral void behind. The face-sharing arrangement of occupied tetrahedral and octahedral voids represents a less-favored configuration, as it implies local F–F contacts that are shorter ( $d \leq 0.433a$ ,  $a$  = lattice parameter) than in the fluorite structure ( $d = 1/2a$ , Figure 4.5b). This configuration is quickly abandoned by migration of another fluoride ion into an octahedral void, whereby an additional tetrahedral vacancy is formed (Figure 4.5c). In this less dense part of the structure

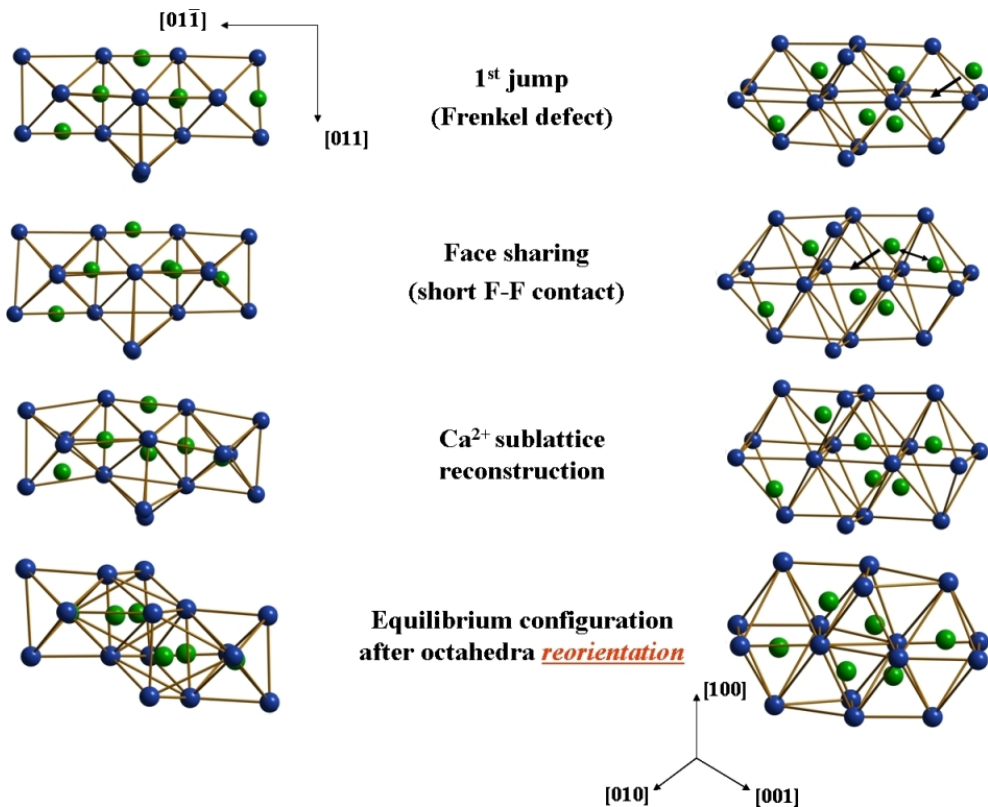


**Figure 4.5:** Local changes in atomic arrangements highlighting the different stages of the cubic-to-orthorhombic transition in  $\text{CaF}_2$ .

the reconstruction of the  $\text{Ca}^{2+}$  sublattice is initiated.

Displacements of portions of (100) Ca layers along [011] with respect to the fluorite structure remove the central octahedral void (Figure 4.5c-d). This is accompanied by the formation of an octahedral void with a different orientation, that shares a face with an adjacent occupied octahedral void. The fluoride ions inside these octahedra move off-center in pyramidal coordination, such that short contacts are avoided. A displacement within an adjacent (100) Ca layer rearranges another octahedron (Figure 4.5d). This second new octahedron shares a face with an octahedron of the pristine cubic structure and an edge with the previously formed new octahedron. Again the fluoride ions occupy the one half of the octahedron (a pyramid) where no short contacts to fluoride ions are formed.

In the cubic close-packed arrangement the centers of the octahedral voids are connected by a single translation, which is reflected in the equal orientation of the octahedra (Figure 4.5a). The overall reconstruction of the  $\text{Ca}^{2+}$  ions sublattice during the phase transition rearranges half of them, which results into two distinct sets of

octahedral voids. This atomic movement is the symmetry-lowering step.

In the overall mechanism distinct directions for the reorganization of the Ca<sup>2+</sup> ions sublattice and for the displacement of F<sup>-</sup> ions appear. In Figure 4.6, upper panel, an early stage of the overall reconstruction is shown. Ca<sup>2+</sup> ions displace along [011], vertically in Figure 4.6. The movement of fluoride ions has been traced by *illuminated* lines [190] over a period of 1.2 ps. This emphasizes the different mobility of fluoride ions in different regions and at different stages of the transforming box. F ions that are still in the fluorite configuration (left) display a short trace, while F ions in the interfacial region (right) exhibit an enhanced mobility reflected by a longer trace. Furthermore, they form chains that propagate diagonally in the box (Figure 4.6, upper panel).

The *jumps* are frequent in the regions where octahedra are reconstructing (red polyhedra) and reach out to neighboring regions, where the reconstruction is about to start. While the overall F ions displacements follows crystallographic directions, the local jumps are uncorrelated, such that this region is *liquid like*. The setup of an interfacial region hence corresponds to a *local melting* of the anions sublattice. Upon propagation of the phase front (Figure 4.6, lower panel). the *liquid like* interface is shifted such that enhanced mobility characterizes this region only. This picture is intrinsically different from a conventional solid-solid transformation. In the latter, the displacement paths of rearranging atoms are well defined in both direction and length.

In terms of symmetry, the initial path over the *Immm* intermediate is quickly abandoned (Figure 4.7, red path), and a different path is found in the course of our molecular dynamics simulation (Figure 4.7, blue path). The important step highlighted in the analysis described above (Figure 4.5) lies in the reorientation of half of the octahedral voids of the fluorite structure. Upon occupation of different octahedral voids by fluoride ions the latter become different in symmetry, because the (centering) vector connecting the octahedra is extinguished. At the same time, the fluoride ions are trapped in their final position, effectively condensating from the liquid like interface into the final cotunnite structure.

The path over the *Cmca* intermediate (Figure 4.7, blue path) allows a splitting of the fluoride positions (crystallographic and dynamic at the same time) and corresponds to the preferred mechanism identified from our simulations. Considering the details of the mechanism, the *translationsgleich* (*t*) branch of the path (*Fm $\bar{3}$ m* – *Fm $\bar{3}$*  – *Fmmm*) corresponds to the superionic region characterizing the interface, while the *klassengleich* *k* segment (*Fmmm* – *Cmca* – *Pnma*) hosts the reconstructive steps, and corresponds to a phase front propagation step (Figure 4.6) involving freezing of the anionic sublattice and formation of structural motifs of the new phase.

In summary, the transition is initiated by fluoride ions switching from tetrahedral sites to octahedral voids in the close-packed cations sublattice. The locally liquid anionic sublattice causes Frenkel defects that enable the modification of an otherwise dense and rigid close-packed atomic arrangement. This occurs by antiparallel Ca<sup>2+</sup> ions layer shearing along [011] and reorganization of half of the pristine octahedral voids. The momentarily occupation of octahedral voids causes short F–F contacts in terms of adjacent face-sharing tetrahedra. This unfavorable configuration is resolved

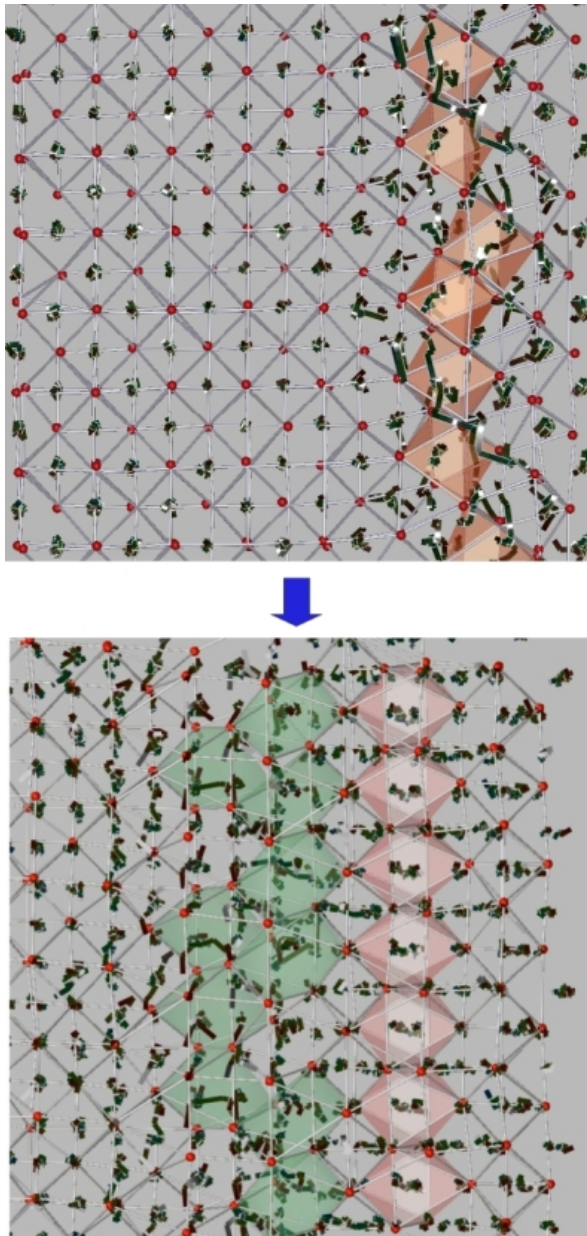


**Figure 4.6:** Fluoride ions mobility highlighted with illuminated lines. (upper panel) Early stage of transformation is marked by high anionic mobility causing the reconstruction of cation sublattice. (lower panel) Percolation of anions via fluorite octahedral voids creates a front of anion sublattice local melt. Octahedra reorientation (red and green polyhedra) solidifies again the  $F^-$  sublattice in the high pressure structure.



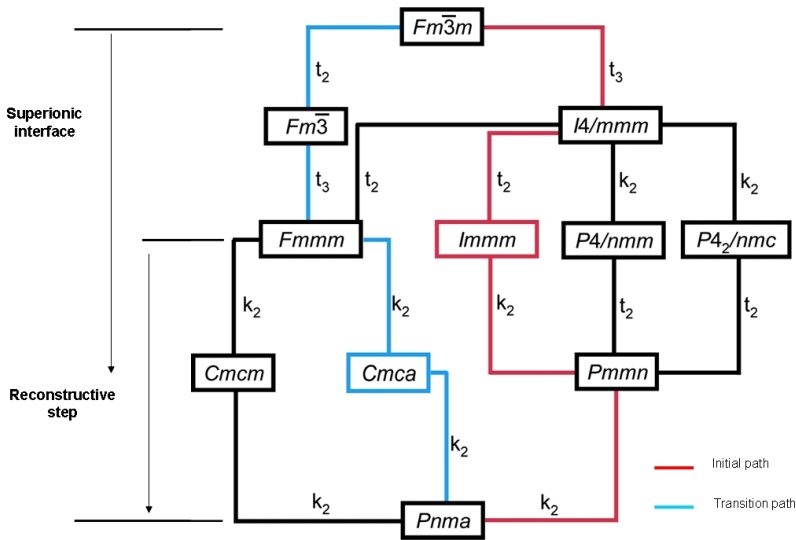


**Figure 4.7:** Two group-subgroup relations reflecting different symmetry aspects of (red path) the geometric model of the initial regime, and (blue path) the different symmetry-lowering steps identified during the simulations.

by a local geometric change that reorients the octahedron. This induces a propagation of the phase interface causing the freezing of the formerly mobile fluoride ions.

Further propagation of the phase front is carried by liquid like fluoride ions that reach out to adjacent layers. The reconstruction of cation sublattice shuts down the pathways of high ionic mobility through octahedral voids. Consequently, the anions freeze again in the high-pressure modified cation arrangement. The nucleation and growth scenario accessible through our simulation resolves different symmetry lowering steps into different regions of the simulation cell. Not only can the global mechanism be identified. The fine granularity of the simulations allow identifying the chemical aspects of symmetry lowering steps: the formation of a liquid like interface, and therein the rules of avoiding face-sharing arrangements that push the fluoride ions in the right adjacent voids, leading to freezing of the fluoride sublattice.

The observation of this phenomenon is closely connected to the applied simulation scheme (TPS combined with MD simulations) which allows the unbiased identification of transformation mechanisms, domain formation, and interface geometries. Nevertheless, interface based ionic mobility was identified in CaF<sub>2</sub>-BaF<sub>2</sub>-CaF<sub>2</sub> sandwich structures [191].

As the identified superionic conduction state only occurs in an interfacial region of the two stable phase domains a direct experimental observation appears rather difficult. However, within the few picoseconds of liquid-like mobility of a single fluorite→cotunnite→fluorite cycle, the fluoride ions diffuse by more than 1 nm. Repeated transitions may hence lead to a percolation of the F<sup>-</sup> ions sublattice of the stable states that should in principle be accessible to the experiment.

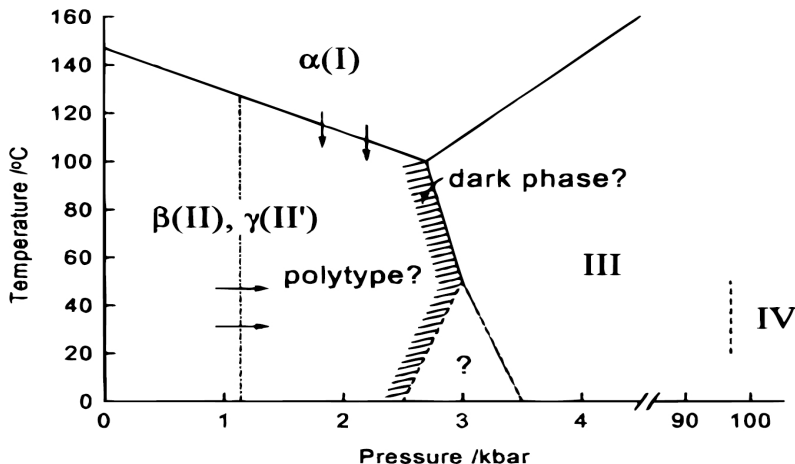


Figure 4.8: Phase diagram of AgI.

## 4.2 Silver Iodide, AgI

Among superionic conductors, *silver iodide* is an archetypal case. Its unique way to combine a variety of interesting forms originates, in part, from its dual bonding character [192], covalent/ionic, and the different polarization effects exhibited by both ions,  $\text{Ag}^+$  and  $\text{I}^-$  [193]. On the other hand, the pronounced polytypism [194–196] and the remarkable ionic conductivity [192, 197] in AgI, combine the properties of a semiconductor and an ionic conductor in one material.

In fact, the polytypism of AgI is closely connected to ion mobility, resulting into several temperature and/or pressure induced phase transitions (Figure 4.8<sup>1</sup>).

In this section, we shall explore the transformation of rocksalt (RS) into wurtzite (WZ) and zincblende (ZB) under the effect of pressure, with a focus on the diffusion paths of  $\text{Ag}^+$  at the WZ/ZB interface.

### 4.2.1 Polymorphism and Properties

The high-temperature modification of silver iodide,  $\alpha\text{-AgI}$  (phase I), is a prototype superionic conductor. Within a *solid* body centered cubic *bcc* sublattice of iodide ions, the *liquid like* state caused by the disorder of silver sublattice, is responsible for the the high ionic conductivity of  $\sim 10^{-1}\Omega^{-1}\text{cm}^{-1}$  at ambient pressure and a temperature equal to 420 K [196]. Cooling down the system induces an abrupt change in conductivity, accompanied by a structural phase transition to WZ/ZB mixed system.

Below 420 K, AgI adopts the wurtzite structure ( $\beta\text{-AgI}$ , phase II). A small amount of silver disorder compared to that of  $\alpha\text{-AgI}$  results into a moderate ionic conductivity at ambient temperature ( $10^{-6} - 10^{-7}\Omega^{-1}\text{cm}^{-1}$ ). Although thermodynamically stable,  $\beta\text{-AgI}$  coexists with another zincblende structured phase,  $\gamma\text{-AgI}$  (phase II'), which

<sup>1</sup>Figure adapted from Ref. [195]

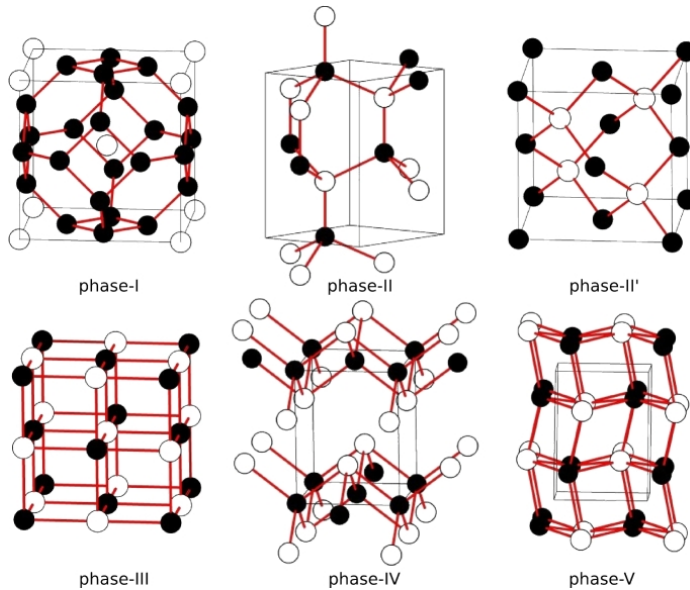


**Figure 4.9:** Polymorphs of AgI. Phases I, II, and II' are also known as  $\alpha$ ,  $\beta$ , and  $\gamma$ , respectively.

has a higher conductivity in the polycrystalline form by about an order of magnitude than that of  $\beta$ -AgI. However,  $\gamma$ -AgI is metastable, as reflected by the irreversible transformation to  $\beta$ -AgI around 363-373 K, and the need to add some amount of copper in order to stabilize it [198].

Both  $\beta$ -AgI and  $\gamma$ -AgI are  $n$ -type semiconductors. The cation transport is promoted by the migration of Frenkel defects with an activation energy equal to 0.41 eV and 0.39 eV for  $\beta$ -AgI and  $\gamma$ -AgI respectively [197].

Like in other polytypical semiconductors, such as SiC and ZnS, the coexistence of wurtzite and zincblende (B4 and B3) phases of AgI at normal conditions results into several polytypes that can be obtained during experiments with different layer stacking orders. For AgI, even-numbered hexagonal polytypes like 4H, 8H, 12H, 16H, etc . . . , have been observed [199], which irreversibly transform into  $\beta$ -AgI (2H) on heating, but well below the  $\alpha$ - $\beta$  superionic transition temperature. The odd-numbered polytype, 7H, was identified in AgI:alumina composite electrolyte [195, 200]. It is responsible for the extremely high conductivity enhancement and the large superionic phase transition hysteresis. Another polytype, 9R, has been observed in same composite electrolyte.

Recently, unusual 7H (ABCBCAC) and 9R (ABCBCACAB) polytype modifications (Figure 4.10<sup>2</sup>, middle and right, respectively) were obtained in nanoplates of AgI resulting into a huge room temperature superionic conductivity and a large hysteresis with respect to the superionic high-temperature phase  $\alpha$ -AgI. The usability

<sup>2</sup>Figure taken from Ref. [196]

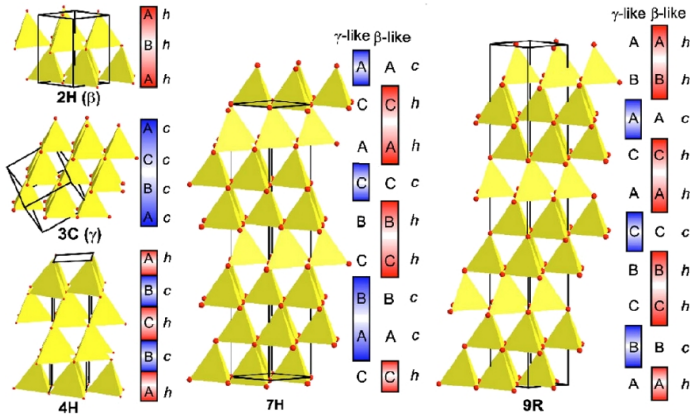


**Figure 4.10:** Different AgI polytypes represented in terms of close-packed iodine tetrahedra occupied by silver ions. The stacking sequences are represented by ABC and  $hc$  notations.

of this material as electrolyte in rechargeable all-solid-state Ag batteries was demonstrated [196].

According to the Phillips scale [147], AgI has the ionicity  $f_i = 0.770$ . This is very close to the critical value  $f_c = 0.785$  which marks the idealized boundary between compounds with fourfold coordinated atoms (like zincblende and wurtzite) and those with sixfold coordination (like rocksalt).

On room-temperature compression, AgI undergoes a structural phase transition from the WZ/ZB mixed phase ( $\beta$ -AgI and  $\gamma$ -AgI) to the rocksalt structure (phase III). Increasing temperature up to 900 K at high pressure less than 4.0 GPa, leads to a distorted rocksalt (phase III') before the compound transforms into liquid [201,202].

The pressure induced phase transition B4/B3 $\rightarrow$ B1 was claimed to proceed via an intermediate phase (IV). In a quite narrow range, 0.3-0.4 GPa at ambient temperature, this phase was determined from powder-neutron diffraction to have the antilitharge-like structure (anti  $\alpha$ -PbO type) described in the  $P4/nmm$  with  $\text{Ag}^+$  ions in Wyckoff position  $2(a)$  (0,0,0) and  $\text{I}^-$  ions located at  $2(c)$  (0,  $\frac{1}{2}$ , 0.292) [203]. However, high-pressure experiments on AgI single crystals revealed that, upon decompression, the antilitharge structure was never obtained [198]. In fact, the existence of this phase is still unclear due to the very limited number of investigations of the pressure-induced phase transitions at low temperature, and the phase diagram of AgI below 200 K has not been fully understood up to now [204]. Raman scattering experiments at low temperature and high pressure showed that  $\beta$ -AgI transforms into rocksalt B1 at 76 K and 0.3 GPa, in a sequence in contrast to that at ambient temperature [205].

The AgI-III phase is a superionic phase as well. The conductivity increases rapidly with temperature attaining a value of  $0.5 \Omega^{-1}\text{cm}^{-1}$ .

At much higher pressures, AgI-III (B1), undergoes another phase transition to a monoclinic KOH-type structure (phase V) [206].

The global structural profile of AgI is characterized by a rich polymorphism and

polytypism. The enhanced  $\text{Ag}^+$  ions mobility is strictly connected to the structure of the immobile sublattice in terms of presence of numerous unoccupied interstitial sites therein, such as the tetrahedral sites in  $\alpha$ -AgI that promote superionic behavior.

In this section we elucidate mechanism of the polymorphic transition, B4/B3–B1, under pressure, with emphasis on two main aspects of the system: (a) ionic mobility and (b) the relation between polytypism and  $\text{Ag}^+$  ions diffusion paths.

### 4.2.2 Transition Models

Considering the nature of AgI as a polytypic and polymorphic material with a high disorder under the influence of both temperature and pressure, the models that have been proposed for the B4–B1 transformation can not be easily extrapolated to transitions between a B4/B3 mixed system and B1.

Recently, cation diffusion paths in cubic  $\alpha$ - $\text{RbAg}_4\text{I}_5$  type superionic conductors have been investigated by means of periodic nodal surfaces [207]. The positions of the mobile cations were suggested to follow a 3D infinite hyperbolic layer.

The few tentatives to describe the transformation in AgI under pressure, provided models for each system separately, B3→B1 and B4→B1. Based on *ab initio* DFT-GGA calculations, Catti [24] described the B3→B1 as a three-step mechanism according to the following sequence:  $F\bar{4}3m \rightarrow Pmm2 \rightarrow P4/nmm \rightarrow Pmm2 \rightarrow Fm\bar{3}m$ . The path is achieved in  $Pm$  space group giving rise to an orthorhombic structure ( $Pmm2$ ) with fivefold-coordinated atoms.

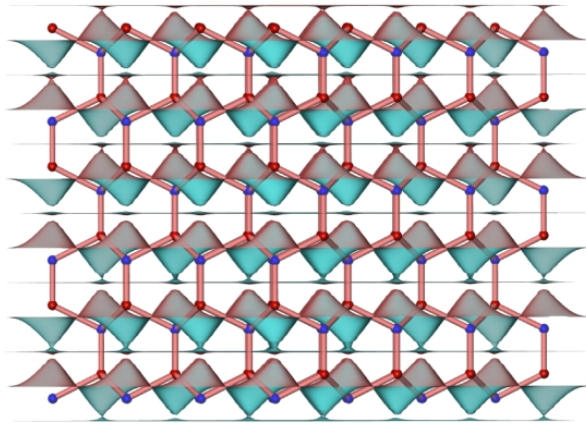
Based on orientation relations between  $\gamma$ -AgI and AgI-III phases deduced from high-pressure experiments on single crystals of AgI, symmetry assumptions have been made concerning the underlying transition mechanism [198]. Two similar paths to those already proposed by Catti [24] have been suggested,  $Pm$  and  $Pmm2$ , but no indication on which one could be the real transformation route.

Besides the fact that the B4→B1 branch was not discussed for AgI, the paths proposed by Catti [24] and Sowa [198] assume the existence of the monoclinic antilitharge-type structure as a mandatory phase during the transition. However, the corresponding paths use another intermediate orthorhombic structure ( $Pmm2$ ) bypassing the monoclinic one.

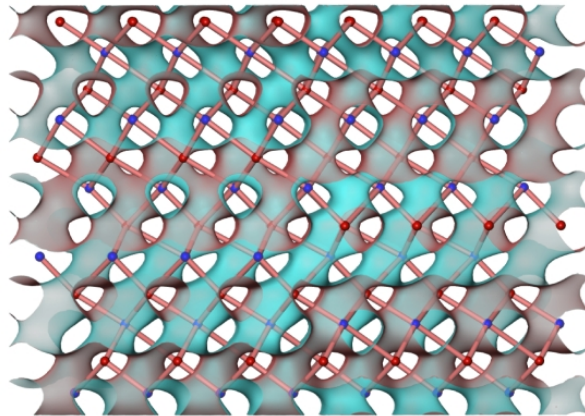
In order to account for relevant aspects of the pressure-induced transitions in AgI without any bias or artificial enhancement of atomic motion, we move now to the results obtained after use of the TPS MD simulation scheme as described in previous sections and chapters.

### 4.2.3 Wurtzite/Zincblende-to-Rocksalt (B4/B3-B1) Phase Transition

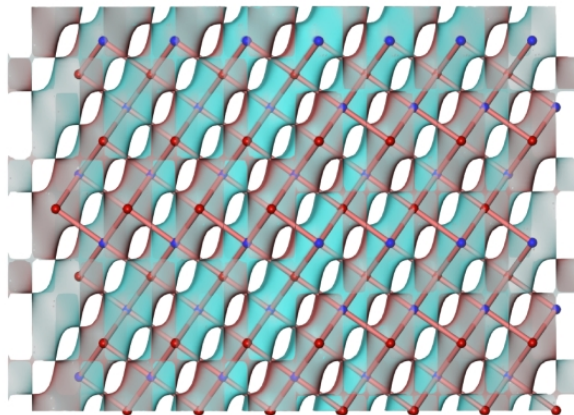
The first challenge imposed by AgI is the dimorphic WZ/ZB nature at ambient conditions. Both structures, WZ and ZB, have been calculated to have almost the same energy at the equilibrium [208]. Since we are simulating at the experimental conditions of pressure and temperature (0.2-0.5 GPa and 300 K), we elucidate the mechanism of the polymorphic back transformation RS→WZ/ZB in order to understand how the interfacing is realized.



WZ (B4)



intermediate



RS (B1)

**Figure 4.11:** Geometric model based on transforming periodic nodal surfaces connecting the WZ structure to the RS structure of AgI over an ordered intermediate configuration.

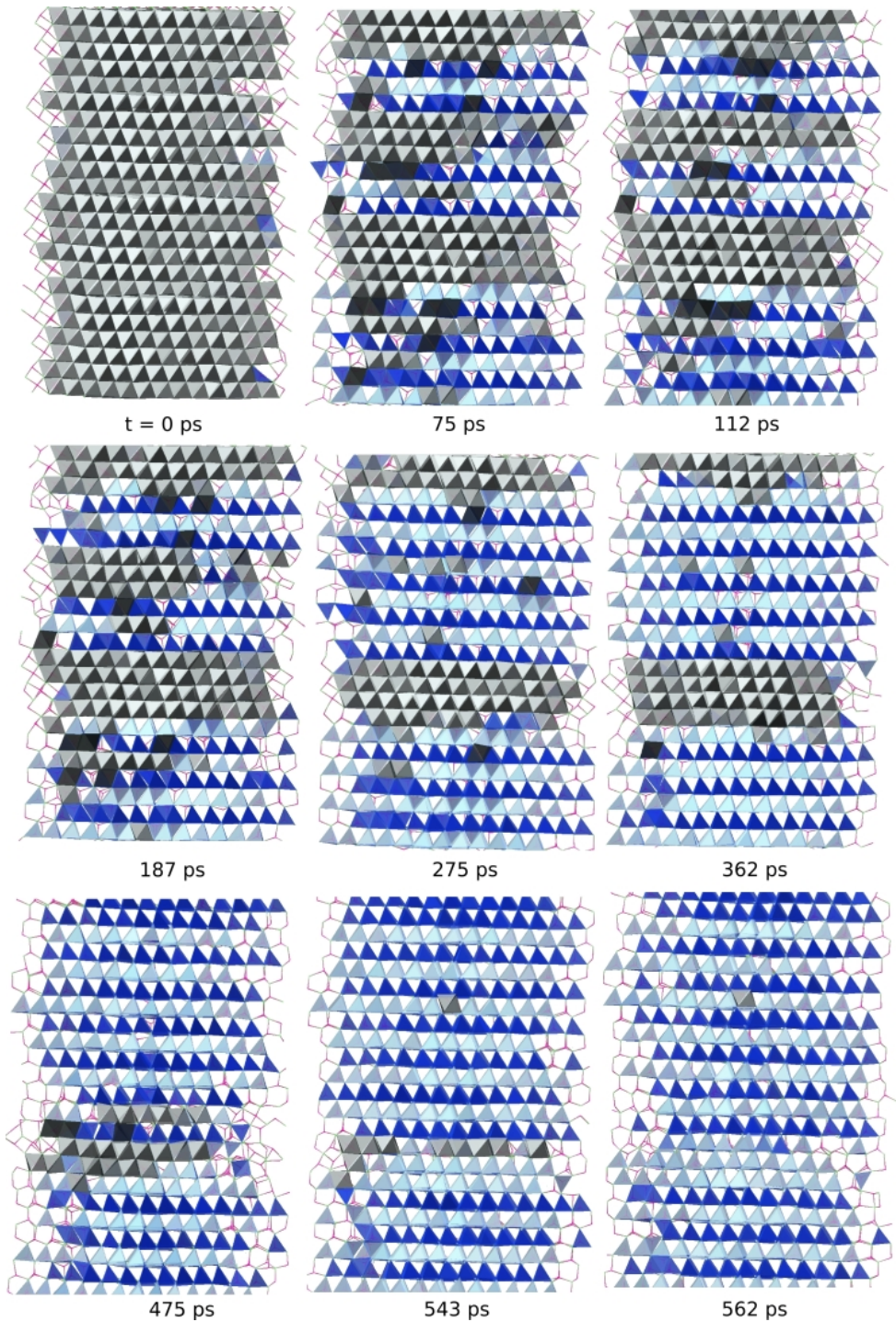


**Figure 4.12:** The RS  $\rightarrow$  WZ/ZB transformation mechanism in AgI. Different phases are identified and colored according to their  $\text{Ag}^+$  ions coordination polyhedra: grey for octahedra, dark and light blue for fourfold coordination to emphasize ABAB and ABC stacking in WZ and ZB respectively.

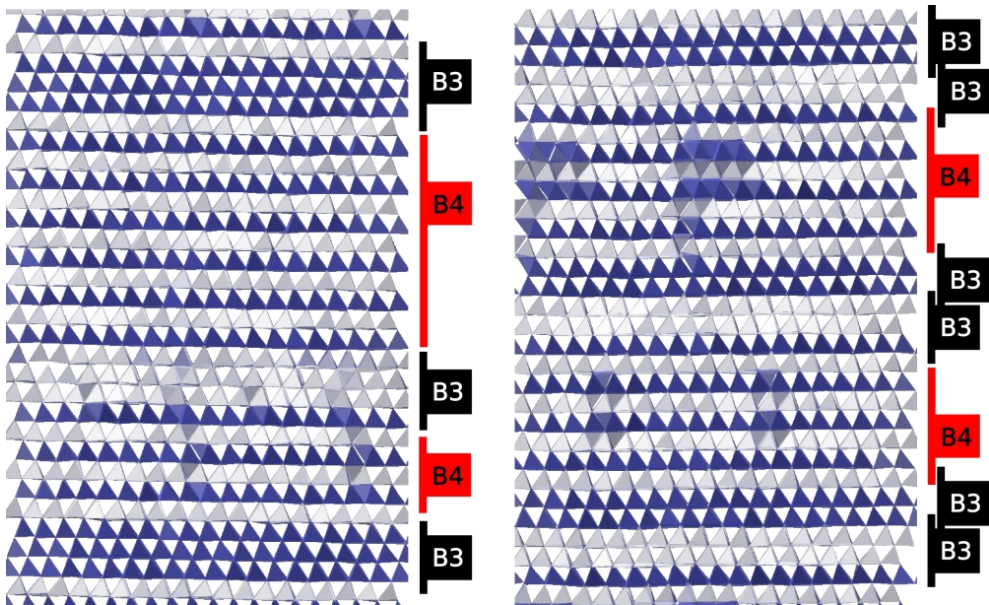


**Figure 4.13:** Two final configurations resulting from the simulations on the RS→WZ/ZB transformation in AgI. Different WZ/ZB stacking sequences are identified and highlighted.

The only prerequisite of the simulation scheme is a first trajectory. We design two separate trajectories, one for the RS→WZ transformation and the other for the RS→ZB. This gives us the advantage to scrutinize the evolution of local configurations at times of nucleation from the RS phase.

We designed first trajectories from transforming periodic nodal surfaces PNS [107–109], as described in sections 3.1.4 and 3.3.4 for GaN and ZnO, and displayed on figures 4.11 and 3.5.

The evolution of the transition regime in two different sets of TPS MD runs, corresponding to each of the mechanisms coded in the previous PNS modeling, shows a shift from a *unimorph – unimorph* transformation toward *unimorph – dimorph*.

Final configurations contain both phases at a predominance of WZ structure. The anions *solid* sublattice is arranged according to the hexagonal stacking sequence ABAB, in alternation with the cubic sequence ABC as shown on the last configuration ( $t = 562$  ps), Figure 4.12.

In the previous section (Sec. 4.1) the transition was characterized by two distinct transformation regimes, *solid-solid-solid* and *solid-liquid-solid*, taking place in low dimensional regions of the system and attributed to cations and anions respectively. The situation in the case of the RS→WZ/ZB transformation in AgI is quite similar. The disorder in the  $\text{Ag}^+$  sublattice is expected to play a major role in determining the atomistic details of the transformation.

The reconstruction of the  $\text{I}^-$  ions sublattice is done in two different stages. First,



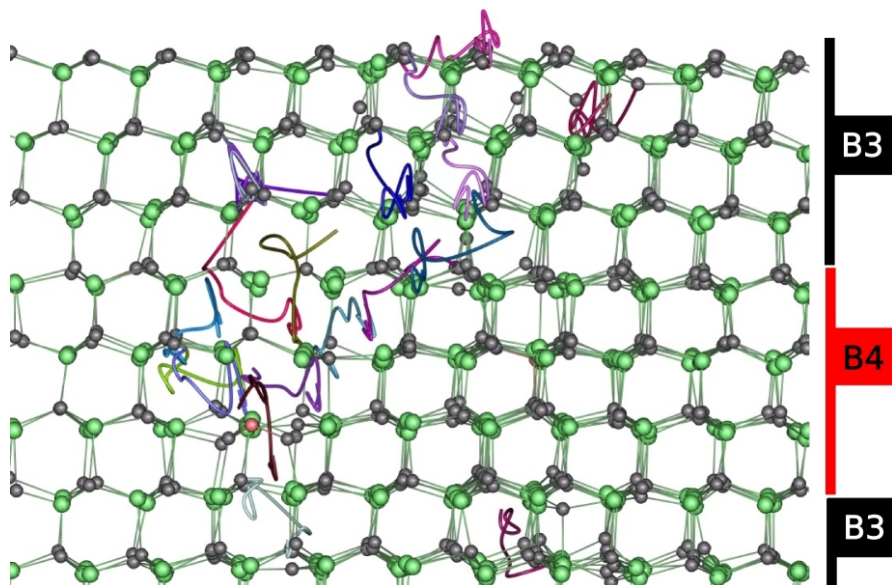


**Figure 4.14:** Traces of longest  $\text{Ag}^+$  movements in the form of a cascade piercing many layers along the mixed WZ/ZB system.

a RS/WZ intermediate is formed (Figure 4.12,  $t = 0 \text{ ps} \rightarrow t = 362 \text{ ps}$ ). Then, in the WZ/RS mixed system (Figure 4.12, at  $t = 562 \text{ ps}$ ), the insets of ZB appear. Both steps are characterized by a straight, shortcoming, and ordered displacements (but not collective) of  $\text{I}^-$  ions in a solid-*solid*-solid regime. The thickness of the ZB region in all runs is very comparable. Three layers of tetrahedra is the common count, although bilayer and four-layer interfaces occur in some runs during the TPS iterations. The WZ phase, however, may be of different thickness in one final configuration as illustrated on Figure 4.13, left structure.

On Figure 4.13, right panel, a particular tetrahedra order was obtained in one of the final configurations obtained from TPS MD simulations. The ZB inset consists of twin bilayers. Such tendency was pointed out in the recent work of Sowa [198] on high-pressure experiments on single crystals of AgI.

The polytypism in AgI was reported in recent studies of Maier [195, 196, 209] on composite systems like  $\text{AgI}:\text{Al}_2\text{O}_3$ . Two polytypes have been identified in the material at ambient conditions, 7H and 9R. They exhibit the following stacking sequence: ABCBCAC and ABCBCACAB, respectively. The odd-numbered periodicity of this polymorph makes it a curious structural issue, only rarely encountered in polycrystalline specimens. The 7H/9R polytype is responsible of the high ionic conductivity in the corresponding AgI nanoplates, in association with a high degree of  $\text{Ag}^+$  ions disorder even at ambient temperature [196].

Enhanced ionic mobility of  $\text{Ag}^+$  ions clearly appeared in the course of the TPS MD simulations performed at high pressure. The occurrence of *Liquid-like* patterns ex-

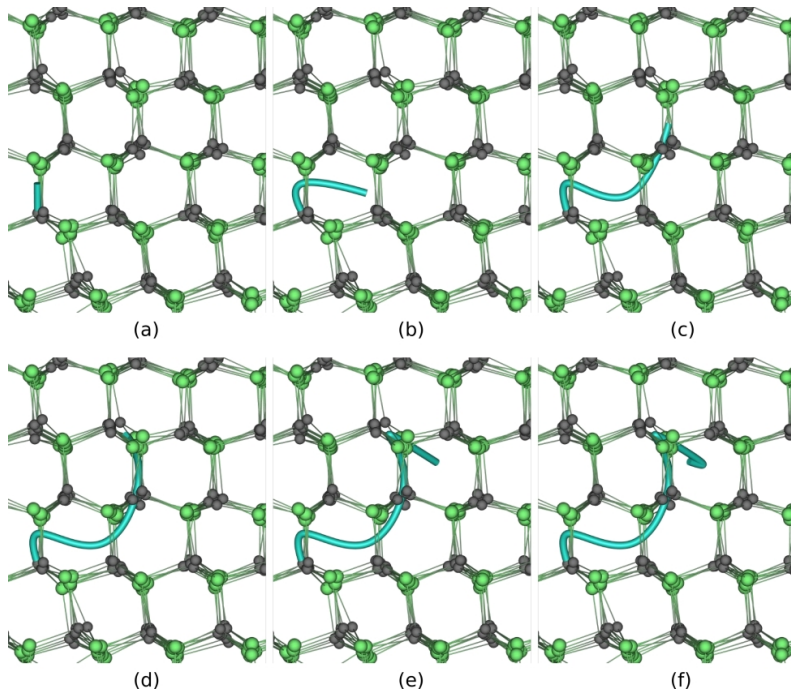


**Figure 4.15:** A representative path of  $\text{Ag}^+$  ion long movement within WZ AgI.

tending across many layers, within the same phase or through the WZ/ZB boundary, was observed. To better capture the phenomenon of high ionic mobility and investigate the role of the stacking sequence in heterostructures with fourfold coordinated atoms, we consider traces of  $\text{Ag}^+$  ions displacements and visualize them within the WZ/ZB configurations.

In Figure 4.14, the longest ionic paths have been traced showing large vertical and diagonal displacements across the simulation box.

The close examination of  $\text{Ag}^+$  ions with long displacements shows the existence of two different preferred transport pathways as shown on Figures 4.15 and 4.16. The zoom is made on the local regions of WZ/ZB interface. In Figure 4.15, an ion  $\text{Ag}^+$  leaves its position and vertically diffuse within WZ region through octahedral and associate tetrahedral voids before setting in the final position. In Figure 4.16, however, a diffusion along a perpendicular direction is observed. The  $\text{Ag}^+$  ion propagates within ZB structure without leaving across the interface. The path is comprised between two planes of  $\text{I}^-$  ions.

Other fashions are possible (Figure 4.14). This is due to the overlap with the solid-solid regime of the  $\text{I}^-$  ions sublattice that accompany the overall reconstruction. The ion transport properties under high pressure may shed some light on ionic mobility in the 7H/9R superstructures in the composite electrolyte  $\text{AgI}:\text{Al}_2\text{O}_3$  [195, 196, 209].

The simulations performed here indicate the key role of many-layer interface to

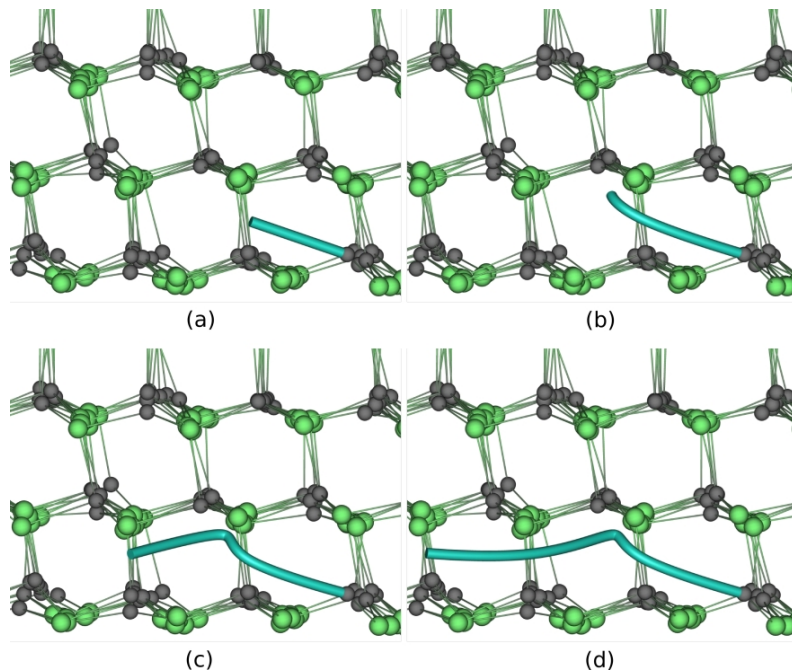


**Figure 4.16:** A representative path of  $\text{Ag}^+$  ion long movement within ZB AgI.

enhance ion mobility. This effect is distinctive of heterogeneous, two component systems like  $\text{AgI-Al}_2\text{O}_3$ ,  $\text{AgBr-Al}_2\text{O}_3$ , and  $\text{AgCl-Al}_2\text{O}_3$  composites. The contact with an ionic insulator in these examples and the interplay between zones of different bulk ionic conduction, cause a difference in vacancies and interstitials distribution in the respective space-charge regions of the composite system leading to an increased space-charge conductivities [196].

In our case, the high-pressure induced phase transition in AgI does not occur in the presence of an ionic insulator and was not simulated so. However, different interfacial along the transition, like RS/WZ and WZ/ZB, allow for the coexistence of different structural motifs with different possibilities for silver disorder in terms of interstitial sites and vacancies affecting the frequency and distribution of Frenkel defects. Consequently, different ion diffusion behavior can be discovered in connection with distinct structural patterns, promoting interlayer disorder.

In summary, pressure-induced phase transformation from mixed system B4/B3 to B1 phase in AgI was investigated by means of molecular dynamics simulations in combination with transition path sampling. Two different ionic transport have been observed, diffusionless in the anionic sublattice and diffusive in the cationic sublattice. Cations diffusion in AgI is promoted by the different types of voids present in wurtzite and zincblende structures as well as the interfaces between them. Accordingly, two types of  $\text{Ag}^+$  superionic movements were identified, intralayer and interlayer paths as-

sociated with B3 and B4, respectively. The disorder induced by superionic movements of  $\text{Ag}^+$  incurred different stacking sequences in the final B4/B3 superstructures. The overall transformation mechanism is realized as a two step mechanism with different phase coexistence regimes. First insets of RS appear in the ZB region forming a WZ/RS mixed system. Then, the latter is fully transformed into RS.

---

# 5 Phase Transitions in Elements

---

## 5.1 Phosphorus, P

When external pressure is applied to a material, the nuclei are brought closer to one another. In order to avoid the increasing mutual repulsion, electron density is compelled to adapt to the new situation through a *modification*.

Bond breaking and formation are often associated with pressure-induced transformations in covalent solids. In solid phases of elements, like phosphorus, carbon, nitrogen, and silicon, varying pressure and temperature lead to a polymorphism very rich in structures and with atomic arrangements often specific to a particular element. Moreover, recent experiments have shown that the high-pressure behavior of elements can be strikingly unexpected and even counterintuitive, like the new partially ionic high-pressure phase of boron [210], or the insulating high-pressure phase of sodium [211].

Although the progress achieved in the determination of crystal structures of elements and the investigation of their chemical and physical properties, the nature of bond change under extreme conditions is not clarified yet.

The still unexplained features of the phase diagram of phosphorus, P, and its ability to form different structural patterns, either as a solid or in the liquid state, have prompted our curiosity. In this chapter we turn our attention to the first transition observed in black P under pressure, in particular, the focus is set on the bond switching mechanism.

### 5.1.1 Polymorphism and Properties

Black phosphorus PI (orthorhombic,  $Cmca$ , A17) is known to be the thermodynamically stable P allotrope under ambient temperature and pressure [212,213]. It consists of layers of six-membered rings in chair conformation where all P atoms are threefold coordinated. Pairs of rings are connected in *cis*-decalin fashion (Figure 5.1a) and form zigzag layers stacked along [010]. This phase is a semiconductor with a narrow band gap of 0.3 eV [214,215].

On compression, the A17 phase of P undergoes a phase transition to the PV phase (rhombohedral,  $R\bar{3}m$ , A7) at  $\sim 5$  GPa [216,217]. P atoms are threefold coordinated in this modification as well. The six-membered ring layers, however, are made of pairs

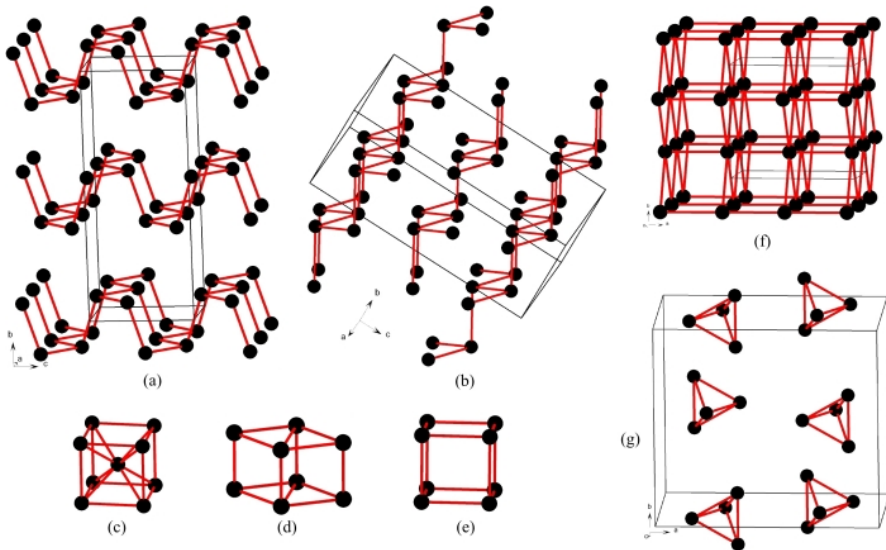


**Figure 5.1:** Polymorphs of phosphorus: (a) black phosphorus PI (A17), (b) As-I like PV (A7), (c) PVIII (*bcc*), (d) PVII (*sh*), (e) PVI (*sc*), (f) incommensurate PIV (*ic*), and (g) white phosphorus P4.

of chair-type rings connected in *trans*-decalin fashion instead. The layers are stacked along  $[001]$  in the hexagonal axis system (Figure 5.1b).

The occurrence of metallization during the A17-A7 phase transition in P was confirmed by optical [218] and electrical conductivity measurements [219]. The superconducting temperature increased from 4.5 K to 13 K [220].

The semi-metallic PV phase transforms into the metallic simple cubic structure PVI (*sc*,  $Pm\bar{3}m$ ) (Figure 5.1e) at  $\sim 10$  GPa [216,217], to which it is group-subgroup related. Accordingly, the transformation was described via small antiparallel displacements of  $\pm 0.035$  along  $[111]_{\text{PVI}}$ , with an increase of the rhombohedral angle from  $57.262^\circ$  to  $60^\circ$  [216].

The cubic modification, PVI, is stable up to  $\sim 107$  GPa where it transforms into an intermediate phase PIV (Figure 5.1f) followed by another transition to the simple hexagonal phase PVII (*sh*,  $P6/mmm$ ) (Figure 5.1d) at a pressure  $\sim 137$  GPa [217, 221]. Both transformations are first-order and the metallic character is maintained.

The intermediate phase PIV along the simple cubic to simple hexagonal transition remained for a long time as an unknown structure. Few descriptions have been proposed, like the orthorhombic  $Imma$ , the host-guest Ba-IV type, and the orthorhombic  $C2mm$  structures. In 2008, the incommensurate modulation was determined from X-ray diffraction experiments and first-principles calculations in the orthorhombic modification noted  $Cmmm(00\gamma)s00$  [222].

Extreme compression to 262 GPa induced transformation to the body-centered cubic phase PVIII (*bcc*,  $Im\bar{3}m$ ) (Figure 5.1c) and represents the highest transition

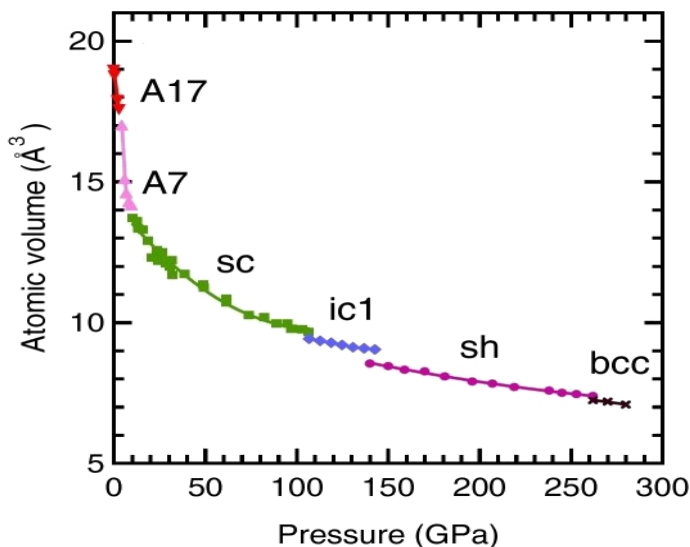


**Figure 5.2:** Dependence of the atomic volume on pressure for phosphorus solid phases.

pressure in all materials [223].

The full transformation sequence in elemental phosphorus at ambient temperature and on varying pressure is:  $PI(Cmca) \rightarrow PV(R\bar{3}m) \rightarrow PVI(Pm\bar{3}m) \rightarrow PIV(Cmmm(00\gamma)) \rightarrow PVII(P6/mmm) \rightarrow PVIII(Im\bar{3}m)$ , and the pressure dependence of atomic volumes as shown on Figure 5.2<sup>1</sup>.

The overall behavior of phosphorus under pressure is strikingly different to that of its heavier homologues, As, Sb, and Bi. While P adopts simple packed structures at high pressure, like simple cubic PVI and simple hexagonal PVII, the other elements transform into a more complex host-guest arrangements like the Bi-III structure. The *s-d* band mixing under the effect of compression is believed to play a key role in the stability of the corresponding structures [224].

Beside the series of structures obtained by varying pressure, phosphorus has been synthesized in form of polymeric tubes, like in fibrous red phosphorus and violet phosphorus varieties [225].

Another less common feature of monoatomic compounds, however exhibited by P, is the occurrence of a first-order liquid-liquid phase transition. At low pressures, liquid P forms a molecular liquid consisting of P<sub>4</sub> tetrahedral molecules. Compression or heating cause a transition to a polymeric liquid accompanying dissociation of the molecules and large volume contraction [226].

The unique features of the phase diagram of phosphorus is owed to the ability of P atoms to bond to one another in different coordinations and structures. The chemical trends behind P polymorphism and its high pressure behavior can be clarified by a firm understanding of bond change mechanism during structural reconstruction from

<sup>1</sup>Figure adapted from [223]

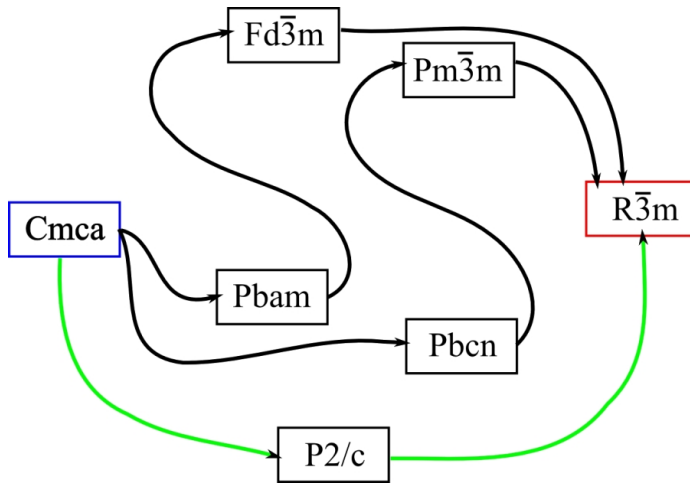


**Figure 5.3:** Symmetry relationships between space groups of A17 (blue frame) and A7 (red frame) phases of P based on a displacive approach of the transformation. Three paths are proposed: one going through a common subgroup (green path) and two paths implying a symmetry upgrade to ensure the connection (black paths).

one phase to another. We shall elucidate how bonding in phosphorus is influenced by pressure to drive the phase transformation from PI to PV structures.

### 5.1.2 Phase Transition Models

The A17-A7 phase transition in phosphorus is first-order and the space groups of the corresponding phases are not directly related in terms of one group-subgroup relationship. Recently, three symmetry-based models were proposed [216]. The first uses a common monoclinic subgroup to relate atomic positions in PI and PV phases, while the two others imply common cubic supergroups as shown in Figure 5.3.

In the common subgroup description, the A17 and A7 structures can be described in a monoclinic structure ( $P2/c$ ,  $Z=8$ ) (Figure 5.6) with phosphorus atoms occupying two Wyckoff positions  $4g$  for each structure: (0.0806, 0.7500, 0.8534) and (0.4194, 0.2500, 0.8534) in the A17 structure, (0.0700, 0.5000, 0.8925) and (0.4300, 0.0000, 0.8575) in the A7 structure. Consequently, the A17 structure can be transformed into the A7 by antiparallel displacements of adjacent (010) layers by  $\pm 1/4$  along [100]. A shear deformation is coupled with the latter displacements decreasing the monoclinic angle  $\beta$  of the common substructure from  $90^\circ$  to  $86.62^\circ$ .

Both PI and PV structures contain as building units six-membered rings in the chair conformation, stacked along [012] in PI and along [111] in PV, in a very similar fashion to that observed in the neighboring Group IVa elements Si and Ge [227]. This idea is at the origin of the path going through the supergroup  $Fd\bar{3}m$  where both structures, A17 and A7, are derived from a diamond-type structure.

The last alternative, through a simple cubic structure  $Pm\bar{3}m$ , was suggested from



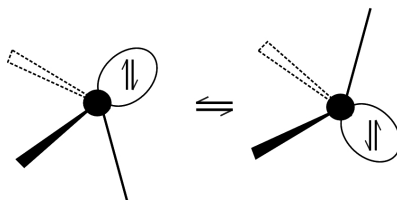


**Figure 5.4:** Local reorientation of a lone pair associated with the A17-A7 phase transition in P pictured via a schematic representation of lone pair flipping between two local environments corresponding to both structures.

a Peierls distortion based on comparison of phonon modes in both polymorphs [228].

The simple cubic structure ( $Pm\bar{3}m$ ) is adopted by P on further compression of the PV phase, and the corresponding phase transition,  $PV \rightarrow PVI$ , requires a much higher pressure to be observed ( $P_{PI \rightarrow PV} = 4.2$  GPa and  $P_{PV \rightarrow PVI} = 10.2$  GPa). This invalidates the path  $Cmca \rightarrow Pbcn \rightarrow Pm\bar{3}m \rightarrow R\bar{3}m$ .

The other path making use of a diamond-like structure in the supergroup  $Fd\bar{3}m$  implies a variation of the coordination number of P atoms from 3 (PI) to 4 (diamond-like), then to 3 (PV) again. With five electrons in the valence states ( $3s^23p^3$ ), P is unlikely to adopt fourfold coordination within this range of pressure (0-5 GPa). In the absence of first-principles calculations that demonstrate the relevance of the intermediate structure with fourfold coordinated atoms as a step in an energetically favored PI–PV transformation path, such assumption appears highly questionable.

Approaching the PI→PV phase transition in terms of symmetry relationships linking both polymorphs overlooks a very important aspect of phosphorus: the existence of *lone pairs* and their role and dynamics during the transformation (Figure 5.4).

Stereochemically active lone pairs show an intriguing phenomenon. The tendency to be localized in well-defined regions creates volumes of lone pairs that shape the crystal structure. For instance, it was shown that lone pairs tend to aggregate with negatively charged ions to form an interface that divides inorganic materials into ionic and covalent parts [229].

In order to understand the chemical aspect of the PI–PV transition, we need first to have an idea about the bonding in P, precisely in PI and PV polymorphs.

### 5.1.3 Orbital Localization in Phosphorus from Maximally Localized Wannier Functions

The orbital localization, in molecular and periodic systems, can be nicely pictured and analyzed using the Maximally Localized Wannier Functions (MLWFs) [146, 230–234]. Their concept was first introduced by Wannier in 1937 [230] and has recently attracted a considerable attention due to the advancement achieved in the field of electronic structure calculations [231].

For periodic solids, the electronic structure is described in terms of Bloch functions, eigenfunctions of both Hamiltonian and lattice translation operators. Their

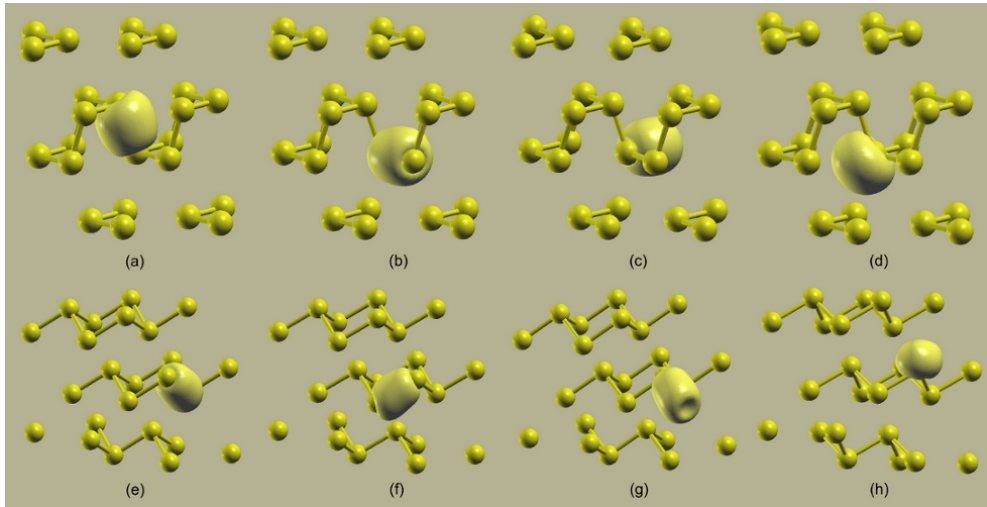


**Figure 5.5:** Maximally localized Wannier functions projected on  $3s$  and  $3p$  states of P for both PI (upper row) and PV (lower row) phases. The  $\sigma$  bond like character for the three first functions corresponding to P–P contacts is displayed ((a)-(c) and (e)-(g)), while the *pillow* shape ((d) and (h)) is a clear signature of an orbital carrying a lone pair. The ensemble of the four MLWFs indicates, for each structure, an  $sp^3$  hybridized bonding picture.

delocalized nature hinders any meaningful visualization. To remedy such a weakness, MLWFs provide a solution using a unitary transformation of Bloch functions. Unlike the complex Bloch functions, MLWFs are purely real and well localized in the real space. Consequently, they are easy to visualize and analyze, not only by considering their shape, but also by extracting characteristic parameters such as the MLWFs centers, spreads, and hopping integrals [146,232–234]. By the elimination of the imaginary part and the extended nature of the Bloch functions, real space visualization of MLWFs often displays a character similar to  $s$ ,  $p$ ,  $d$ ,  $f$  atomic orbitals, or hybrid thereof ( $sp^3$ ,  $sp^2$ ,  $sp$ ,  $sp^3d$ , ...).

Wannier functions are not uniquely defined, due to the arbitrary freedom in the phases of the Bloch orbitals. In the multiband case, this freedom becomes more general and includes the choice of arbitrary unitary transformation among all the occupied orbitals at every point in the Brillouin zone. This indeterminacy was resolved by requiring that the total spread (Eq. (5.1)) of the Wannier functions be minimized in real space.

$$S = \sum_n (\langle r^2 \rangle_n - \langle r \rangle_n^2) \quad (5.1)$$

The application of the concept of MLWFs to phosphorus phases (PI and PV) allows to identify bonding and non-bonding interactions. The corresponding centers can be associated with  $\sigma$  P–P simple bonds and lone pairs based on a localized orbital approach [235]. Figure 5.5 illustrates the isosurface plot of the MLWFs projected on

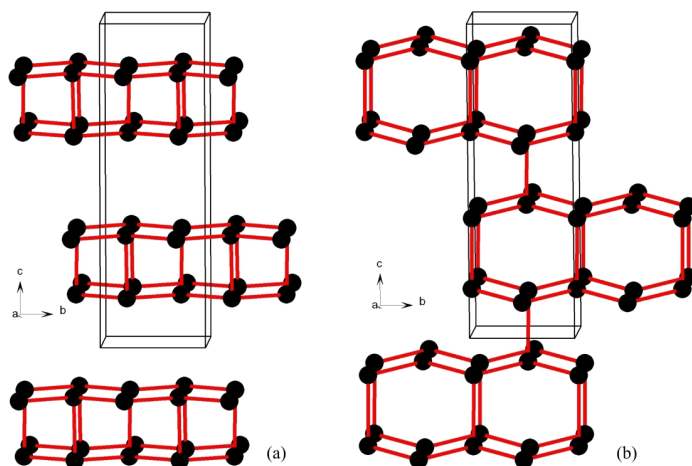


**Figure 5.6:** Common cells (solid black lines) used to relate atomic positions in the (a) PI structure and the (b) PV structure using a monoclinic subgroup  $P2/c$ .

the valence states  $3s3p$  of P. For a selected atom, an  $sp^3$ -like hybridization can be clearly identified with three functions displaying  $\sigma$  character of P–P simple bonds, for each structure, A17 (Figure 5.5a-c) and A7 (Figure 5.5e-g). While the centers of the latter MLWFs are located around the middle of the corresponding P–P bonds, the centers of the pseudo-spherically shaped functions (Figures 5.5d and 5.5h), are more attracted to the P atom and both functions are associated with lone pairs.

Once interatomic interactions are clarified in terms of MLWFs, we proceed to the elucidation of the mechanistic details of the pressure induced phase transition in P. Transition path sampling method in combination with molecular dynamics simulations, as described and applied in previous chapters, was used to obtain the mechanism of the A17-A7 transition. The latter is analyzed by calculating MLWFs in order to understand the change in electronic structure of P under high pressure.

#### 5.1.4 Orthorhombic A17 to Rhombohedral A7 Phase Transition

The only prerequisite for the simulation procedure (TPS combined with MD simulations) is the existence of a first trajectory connecting PI and PV structures. Because such a trajectory does not need to propagate close to the real transition regime, we use for its fabrication the symmetry based model proposed in [216], and shown on Figure 5.6.

In a common monoclinic cell belonging to the space group  $P2/c$ , atomic positions are mapped from one structure to another via linear interpolation. Cell parameters are derived accordingly. The interpolated intermediate structures are propagated in both directions of time until a successful trajectory is obtained. This dynamical first path is used for trajectory sampling.

The simulation box contained 144 phosphorus atoms. To account for the metallic

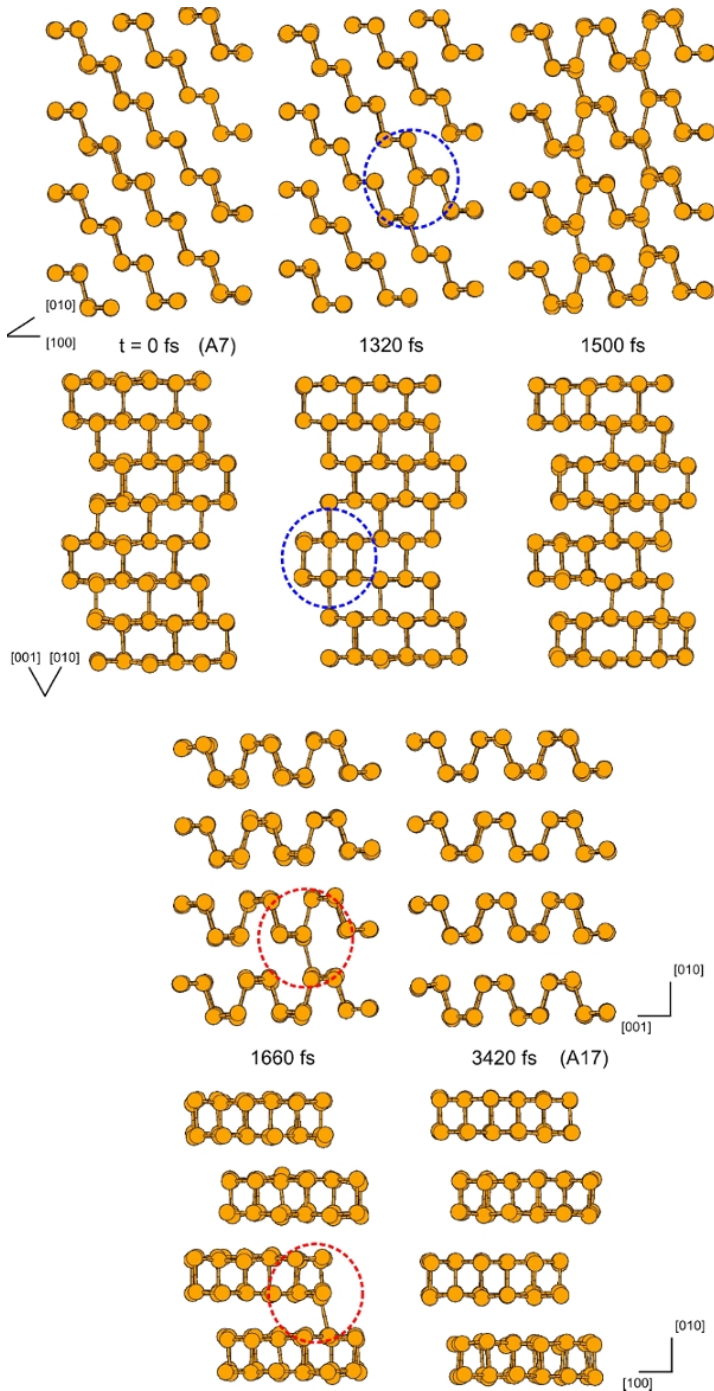


**Figure 5.7:** Snapshots taken from a representative trajectory of the real mechanism for the PI-PV phase transition. Both front (upper row) and side (lower row) views are shown for better visibility of relevant atomic displacements along the transition. The nucleus marking the onset of the A7→A17 (or A17→A7) transition is highlighted by blue (or red) circle.

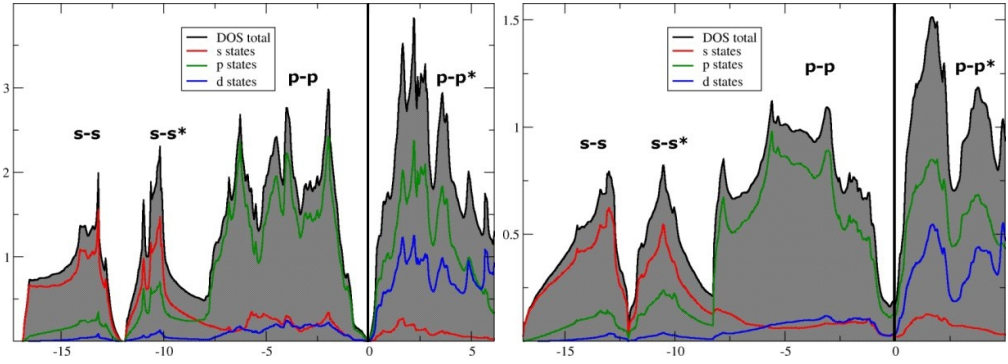


**Figure 5.8:** Total and projected densities of states for phosphorus in the normal pressure (left) A17 structure and (right) the high pressure A7 structure. Fermi level is set to zero.

character of PI and PV phases of P, and due to the covalent P–P bonding, interatomic forces were determined according to the tight-binding density functional scheme developed by Seifert [236]. Molecular dynamics runs have been performed using *ab initio* molecular dynamics code cp2k<sup>2</sup> [237]. Therein, the integration of equations of motion is carried by the velocity verlet algorithm [61]. Good time-reversibility is maintained using a time step as small as 0.2 fs. In order apply experimental conditions of temperature and pressure (300 K and 4.2 GPa respectively), constant-temperature and constant-pressure ensemble developed by Martyna *et al.* [238] has been used.

Several runs of trajectory sampling, with different initial conditions of velocity distribution and momenta perturbation amplitude, have been started. All runs have converged to the same mechanistic regime illustrated in Figure 5.7. The onset of the transition is marked by the formation of a nucleus via a single bond switch from an intra-layer P–P contact to an inter-layer one (Figure 5.7, at  $t = 1320$  fs for A7→A17 and at  $t = 1660$  fs for A17→A7). A chain of bond switching events are triggered by this event and propagated (Figure 5.7, at  $t = 1500$  fs) until P layers stacked along  $[010]_{A17}$  are completely reconstructed into A7 structure

During transformation, the interlayer spacing is compressed via antiparallel shift of P layers along  $[100]_{A17}$  and cell contraction along  $[010]_{A17}$ . Consequently, pairs of non-bonded P atoms are juxtaposed at a shorter distance than in the original A17 structure. A new P–P bond is formed along  $[021]_{A17}$  at the expense of the intralayer bonds (Figure 5.7, at  $t = 3420$  and 1660 ps).

The propagation of such bond switching along  $[010]_{A17}$  converts the A17 structure into the A7 structure (Figure 5.7, at  $t = 1500, 1320,$  and  $0$  ps). As a result,  $(001)_{A17}$  layers are parallel to  $(211)_{A7}^{trigonal}$  layers and  $(100)_{A17}$  layers are parallel to  $(01\bar{1})_{A7}^{trigonal}$  layers.

The above mechanism analysis, pictured in Figure 5.7, is based on an interatomic P–P distance criterion ( $r_{cut}=1.4$  Å). This description offers a convenient crystallographic picture of the transition and a simple way to identify local atomic displacements. The concept of bond deformation (breaking and formation), however, requires

<sup>2</sup>M. Parrinello *et al.*, <http://cp2k.berlios.de>

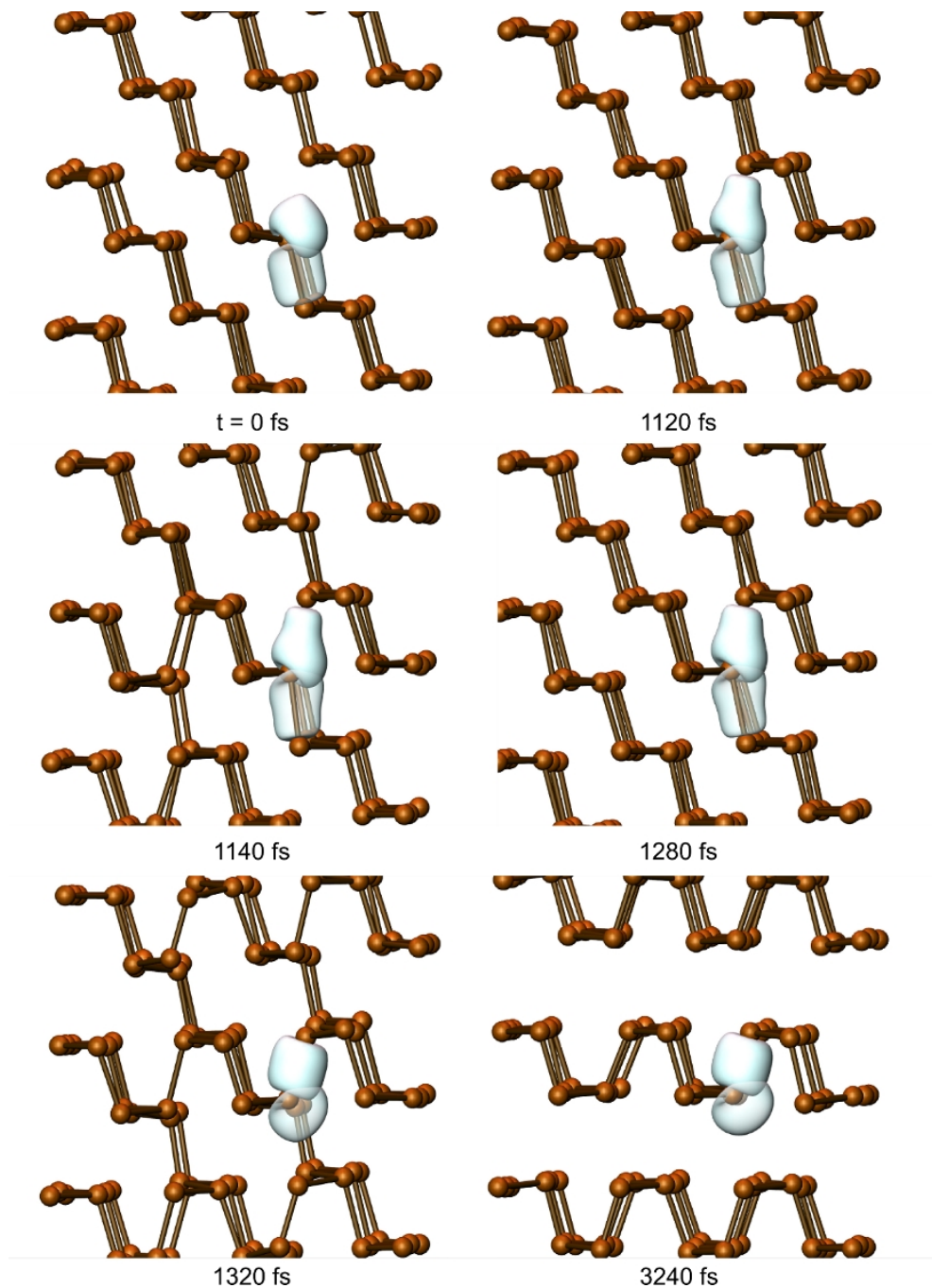


**Figure 5.9:** Changes of two MLWFs of a selected atom during the A17-A7 transformation. Two MLWFs are shown. The opaque function is initially associated with a lone pair, and the transparent one with a  $\sigma$  P-P bond. The overall picture emphasizes a lone pair  $\leftrightarrow$  simple bond conversion mechanism during the A17-A7 transition in phosphorus.

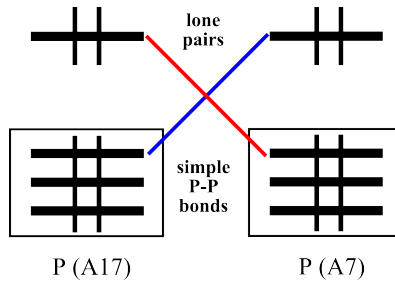


**Figure 5.10:** Schematic diagram of the frontier molecular orbitals of P in a threefold symmetry. Blue and red lines represent the correspondence between states after phase transition.

a deeper analysis performed at the electronic level of details.

To capture the electronic aspects of the A17–A7 transition in P, we have computed the electronic density of states (DOS) for the ground state and the high-pressure structures. The corresponding curves are shown in Figure 5.8. The calculations have been performed using first-principles full-potential FPLO method <sup>3</sup>. The DOS splits, in both cases, into four parts:  $s-s$  bonding,  $s-s^*$  antibonding,  $p-p$  bonding, and  $p-p^*$  antibonding. The Fermi level is placed between the two latter blocks of states and both elements remain semimetals. The DOS of the high pressure modification of P is qualitatively very similar to that of the normal conditions structure.

Although P atoms remain threefold coordinated after transition, the A17–A7 phase transition is reconstructive and involves bond deformation. Drawing the electronic profile of the transition via a simple comparison of DOS plots of the limiting structures may overlook relevant aspects associated with local structural changes. The interplay of the occupied electronic states is hidden behind the general similar splitting of the density of states into  $s$ -dominated and  $p$ -dominated blocks. However, the determination of changes in the electronic structure, in a manner consistent with the local atomic displacements depicted in Figure 5.7, is required.

The concept of the MLWFs was employed the analysis of trajectories collected during path sampling simulations. Geometries corresponding to snapshots taken from a model trajectory are analyzed. The construction of MLWFs is based on the use of Bloch functions and overlap matrices generated using an *ab initio* method. We used the first-principles pseudo-potential plane-wave method coded in the Quantum-ESPRESSO <sup>4</sup> program to get wavefunctions corresponding to the selected geometries. The calculations were conducted using an ultrasoft pseudopotential for P with the electronic configuration  $3s^23p^2$  and nonlinear core correction. The exchange-correlation interaction was taken into account within the generalized gradient approximation (GGA) [239] according to Perdew-Burke-Ernzerhof (PBE) functional [240]. We have used a  $4 \times 4 \times 4$  k-point mesh, and a plane-wave energy cutoff of 60 Ry.

After the ground state of each P configurations is obtained, Bloch states are generated on a uniform k-point grid. Then, a list of the required overlaps is computed. In

<sup>3</sup>K. Koepnik and H. Eschrig, <http://www.fplo.de>

<sup>4</sup>P. Giannozzi *et al.*, <http://www.quantum-espresso.org>

the next step, Bloch states are projected, in the real space, onto a set of trial orbitals using the post-processing utility pw2wannier90 [146]. The final step consisted in the construction the MLWFs performed with the wannier90 program <sup>5</sup>.

The MLWFs obtained for a representative trajectory of the real transition mechanism of the A17–A7 transition of P are represented in Figure 5.9. For better clarity, two MLWFs of a guiding atom have been selected to follow bond deformation during the transition. Figure 5.9 illustrates the evolution of MLWFs associated with a lone pair (opaque surface) and  $\sigma$  P–P bond (transparent surface), respectively.

On the eve of P network reconstruction, and before the formation of nucleus at  $t = 1140$  fs, centers of initially different MLWFs are shifted off their original positions in the A7 structure (Figure 5.9,  $t = 0 - 1120$  ps). The center of the MLWF associated with a lone pair is displaced along  $[\bar{1}11]_{A7}^{trigonal}$  and the resulting MLWF indicates a mixing with states of the P atom in the next  $(111)_{A7}^{trigonal}$  layer (Figure 5.9,  $t = 1120 - 1140$  ps). As the structure starts transforming, and the first new P–P contact appears (Figure 5.9,  $t = 1140$  ps), the deformed lone pair MLWF is shaping into a function characteristic of a  $\sigma$  P–P bonding contact (Figure 5.9,  $t = 1140 - 1320$  ps).

The MLWF associated with the  $\sigma$  P–P simple bond shown in Figure 5.9 at  $t = 0$  ps, however, undergoes the inverse deformation of the previous function. The corresponding function center is displaced off P–P bond center toward the guiding P atom while the function adopts an asymmetrical form (Figure 5.9,  $t = 1120 - 1280$  ps) that shapes into a lone pair MLWF (Figure 5.9, at  $t = 3240$  ps). The formation of *nucleus* via bond/lone pair deformation triggers a chain of bond switching along  $[010]_{A17}$  as illustrated on Figure 5.7 at  $t = 1500$  ps.

In both structures, A17 and A7, each P atom displays an  $sp^3$ -like hybridization. Three  $\sigma$  bonds and a lone pair. At the first next neighbor coordination, P atoms have the same local symmetry that can be described by the point group symmetry  $C_{3v}$ . Similarly to the molecular orbital diagram of a  $NH_3$  molecule, valence electrons occupy three energy levels corresponding to  $\sigma$  P–P bonds, while lone pairs are on the chemically active frontier orbital (Figure 5.10). During the transition, the lone pair and one of the P–P bonds MLWFs start deforming simultaneously and exchanging roles according to the new packing of atoms.

So far, the PI-PV transformation was described as a bond switching mechanism. The nucleation of high pressure modification is realized by formation new contacts between  $(010)_{PI}$  layers. Then, the formation of a series of similar contacts is initiated along  $[010]_{PI}$  until reconstruction is completed (Figure 5.7).

The rearrangement of six-membered rings connection from *cis*-decalin to *trans*-decalin fashion keeps lone pairs *stereochemically active*, unlike in the next high pressure modifications (PVI, PIV, PVII, and PVIII). Since the reconstruction cannot occur via simple rotation of rigid pseudo-tetrahedral P units, the reorientation of lone pairs would require a more articulated mechanism.

Orbital localization picture obtained from calculating MLWFs indicated a bond switching mechanism achieved by simultaneous deformation of functions associated with lone pairs and  $\sigma$  P–P bonds. During the transition, the chemical roles are locally swapped (Figure 5.9).

<sup>5</sup>A. A. Mostofi *et al.*, <http://www.wannier.org>



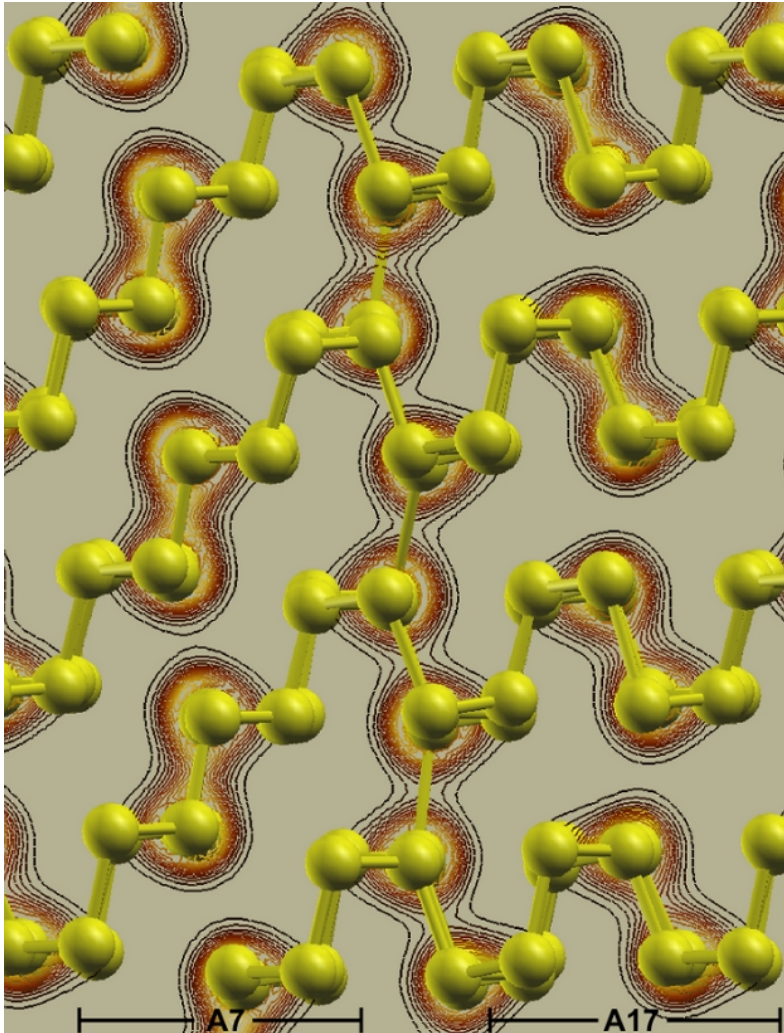


**Figure 5.11:** Isolines of the valence charge density projected on  $(100)_{A17}$  in the phase co-existence regime of A17 and A7 structures. A low dimensional (1D) intermediate structure in the form of a polymeric chain of equidistant P atoms in zigzag fashion is formed along  $[010]_{A17}$ . Isostructural to a  $-(\text{CH}_2)_n-$  polymer, the  $-(\text{PP}_2)_n-$  chain is formed at the interface between PI and PV phases. It is associated with a Peierls instability that facilitates the transition between two types of pairing P atoms in PI and PV.

The simultaneity of orbital deformation during transformation is associated with the appearance of an interface of fourfold bonded P atoms (Figure 5.11, interface between A17 and A7 phases). A zigzag chain running along  $[010]_{PI}$  is made of equidistant P atoms. This *low dimensional polymerization under pressure* is responsible of the reorientation of lone pair electrons during the transition (Figure 5.11).

The polymeric zigzag chain is created at the interface between A17 and A7 structures (Figure 5.11). The calculation of the valence charge density corresponding to the coexistence regime (A7/intermediate/A17) was performed on a uniform grid using the *ab initio* pseudopotential simulation package *siesta*<sup>6</sup>. The projection of charge density on a  $(100)_{A17}$  plane is illustrated using isolines in Figure 5.11.

The projected charge density analysis indicates an atom pairing in both structures, A17 and A7. The reconstruction, however, is realized via an infinite zigzag chain formed along  $[010]_{A17}$ . This monodimensional atomic arrangement is not favorable for P because of the instability caused by the electron excess if compared to a polymeric chain  $-(\text{CH}_2)_n-$ . A Peierls distortion thus leads to a new pairing associated with bond switching and lone pairs reorientation.

In summary, the pressure-induced orthorhombic-to-trigonal (A17-A7) phase transformation in elemental phosphorus has been investigated by means of molecular dynamics simulations combined with transition path sampling method. The A17-A7 transformation is realized by very small atomic movements if compared to several other first-order transitions in the solid state. Additionally, phosphorus atoms remain threefold coordinated after the transition. This suggest a scenario of bond interplay in order to observe the transitio. The transition mechanism obtained from our simulations is characterized by two main events. First, a nucleation center is formed by a switch of a single bond between P layers. Then, a series of bond switching is triggered along  $[010]_{A17}$  until complete transformation from A17 to A7 structures. The nature of the electronic states interplay was determined from a localized orbitals approach as conversion between lone pairs and  $\sigma$  P–P bonds. This conversion is realized by the formation of a low dimensional intermediate zigzag chain along  $[010]_{A17}$  at the interface between PI (A17 structure) and PV (A7 structure) phases. Therein, pairs of P atoms are brought together at equidistant P–P contacts. The Peierls instability associated this zigzag chain offers two possibilities of P atoms pairing and helps switching bonds from a configuration into another.

---

<sup>6</sup><http://www.uam.es/siesta>

# Conclusions and Outlook

*It is a miracle that curiosity survives formal education.*

Albert Einstein

In this work, atomic scale investigation of pressure-induced transformations in the solid state have been carried out. A series of compounds including GaN, ZnO, CaF<sub>2</sub>, and AgI, in addition to elemental phosphorus have been studied. The corresponding transition mechanisms have been elucidated with a clear description of atomic displacements and intermediate structures involved therein.

In the first group of compounds (Chapter 3), the long standing debate on the transition path of the wurtzite(WZ)-to-rocksalt(RS) transition in semiconductors, GaN and ZnO was resolved using geometrical modeling combined with molecular dynamics (MD) simulations conducted in the frame of transition path sampling (TPS) method. In GaN, a two-step mechanism through a metastable intermediate phase with a tetragonal structure  $iT$  has been revealed from simulations. In ZnO, the tetragonal intermediate structure was kinetically less stable, although still part of the real transition mechanism. It appeared at the interface between WZ and RS as consequence of a layers shearing. The transition regime in ZnO was characterized by a competition between  $iT$  structure and another hexagonal intermediate with hexagonal symmetry  $iH$ . Although possible, the latter is not functional for the transition.

In both cases, GaN and ZnO, two points of agreement with experiments have been revealed. The tilting of structures after transition, and the phonon mode softening associated with atomic displacements leading to the tetragonal structure  $iT$

In the second group of compounds (Chapter 4), the investigation of transitions in superionic conductors, CaF<sub>2</sub> and AgI, demonstrated a different and particular behavior of atomic motion under pressure. The solid-solid reconstruction of CaF<sub>2</sub> structure was shown to be initiated and preceded by high disorder of the anionic sublattice. The percolation of fluoride ions through voids in the fluorite structure created a thin interface of liquid like state. The sparse regions caused by the departure of anions facilitates the cation sublattice reconstruction.

In AgI, ion diffusion during the wurtzite/zincblende(ZB) $\leftrightarrow$ rocksalt transition was more pronounced due to the extended stacking disorder WZ/ZB. The Ag<sup>+</sup> ions profited not only from the structure of the interface but used the combination of interstitial voids offered by both phases, WZ and ZB, to achieve long diffusion paths and cause

the cation sublattice to melt. Clearly, a proper account for such phenomena cannot be provided by geometry-designed mechanisms based on symmetry arguments.

In phosphorus (Chapter 5), the question of how the stereochemically active lone pairs are reorganized during the orthorhombic (PI) to trigonal (PV) structural transition was answered by means of simulations. Computation was performed at different levels theory.

First, the mechanism of the transition was obtained from TPS MD simulations. MD runs were performed within density functional tight binding method (DFTB). The analysis of atomic displacements along the real transformation path indicated a fast bond switching mechanism.

In a second step, the nature of the interplay between orbitals of phosphorus during the bond switching was investigated. A simultaneous deformation of lone pair and  $\sigma$  P–P bond showed a mutual switching of roles during the transformation. This interplay caused a low dimensional polymerization of phosphorus under pressure. The corresponding structure formed as zigzag linear chain of fourfold coordinated phosphorus atoms ( $\cdots(\text{P}(\text{P}_2))_n\cdots$ ) at the interface between PI and PV phases.

A further result of this work was the development of a simulation strategy to incorporate defects and chemical doping to structural transformations. On top of the transition path sampling iterations, a Monte Carlo like procedure is added to step-wise substitute atoms in the transforming system. Introducing a chemically different dopant to a pure system represents a perturbation to the energy landscape where the walk between different phases is performed. Therefore, any change in the transition regime reflects the kinetic preference of a given structural motif at times of phase formation.

This method was applied to the elucidation of WZ-RS transition mechanism in the series of semiconducting compounds AlN, GaN, and InN. Simulations showed that In atoms adopt the same transformation mechanism as in GaN and favor it, while Al atoms demonstrated a significant reluctance to the path going through tetragonal intermediate  $iT$ . The difference between transition regime in mixed systems  $\text{In}_x\text{Ga}_{1-x}\text{N}$  and  $\text{Al}_x\text{Ga}_{1-x}\text{N}$  is in agreement with experiments on high-pressure behavior of AlN, GaN, and InN. While transitions in GaN and InN are reversible down to ambient conditions, AlN is stable.

The work presented in this thesis constitutes the seed of new perspectives in the understanding of pressure-induced phase transformations in the solid state, where the physics and the chemistry are brought together by means of computer simulations.

# Bibliography

- [1] N. V. Chandara Shekar and K. Govinda Rajan, *Bull. Mater. Sci.* **24**, 1 (2001).
- [2] P. Ehrenfest, *Proc. Kon. Amsterdam Acad.* **75b**, 153 (1933).
- [3] P. Borrmann, O. Mülken, and J. Harting, *Phys. Rev. Lett.* **84**, 3511 (2000).
- [4] J. M. Buerger, in *Phase Transformation in Solids*, edited by R. Smoluchowski, J. E. Mayer, and W. A. Weyl (Wiley, New York, 1951).
- [5] L. Delaey, in *Diffusionless Transformations. In Phase Transformations in Materials, Material Science and Technology*, edited by P. Haasen (VCH Publishers, New York, 1991).
- [6] A. G. Christy, *Acta Cryst. B* **49**, 987 (1993).
- [7] V. P. Dmitriev, S. B. Rochal, Y. M. Gufan, and P. Toledano, *Phys. Rev. Lett.* **60**, 1958 (1988).
- [8] T. Matsuo, in *Encyclopedia of Supramolecular Chemistry*, edited by J. L. Atwood and J. W. Steed (CRC Press, New York, USA, 2003).
- [9] B. Van Roie, J. Leys, K. Denolf, C. Glorieux, G. Pitsi, and J. Thoen, *Phys. Rev. E* **72**, 041702 (2005).
- [10] R. Hilfer, *Phys. Rev. E* **48**, 2466 (1993).
- [11] P. Perrot, *A to Z of Thermodynamics* (Oxford University Press, USA, 1998).
- [12] M. P. Anisimov, *Russian Chem. Rev.* **72**, 591 (2003).
- [13] J. W. Gibbs, *The Collected Works* (Longmans, Green and Co. Ltd., New York, London, Toronto, 1928).
- [14] J. Frenkel, *Kinetic Theory of Liquids* (Oxford University Press, London, 1946).
- [15] J. Merikanto, A. Lauri, E. Zapadinsky, and H. Vehkamäki, in *NUCLEATION AND ATMOSPHERIC AEROSOLS: An Insight into the Failure of Classical Nucleation Theory*, edited by C. D. O'Dowd and P. E. Wagner (Springer, Netherlands, 2008).
- [16] L. Landau and E. Lifshitz, *Course of theoretical physics* (Pergamon Press, Oxford, 1959).
- [17] J. C. Tolédano, P. Tolédano, and J.-C. Tolbedano, *The Landau Theory of Phase Transitions: Application to Structural, Incommensurate, Magnetic and Liquid Crystal Systems* (World Scientific Pub. Co., Singapore, 1987).
- [18] P. Tolédano and V. Dmitriev, *Reconstructive Phase Transitions: In Crystals and Quasicrystals* (World Scientific Pub. Co., Singapore, 1996).
- [19] M. T. Dove, *Amer. Miner.* **82**, 213 (1997).
- [20] J. L. Alperin, *Local Representation Theory: Modular Representations as an Introduction to the Local Representation Theory of Finite Groups* (Cambridge University Press, Cambridge, 1993).
- [21] H. T. Stokes and D. M. Hatch, *Phys. Rev. B* **30**, 4962 (1984).
- [22] H. Sowa and E. Koch, *Acta Cryst. A* **57**, 406 (2001).
- [23] M. Catti, *Phys. Rev. Lett.* **87**, 035504 (2001).

- [24] M. Catti, Phys. Rev. B **72**, 064105 (2005).
- [25] A. Laio and M. Parrinello, Proc. Natl. Acad. Sci. USA **99**, 12562 (2002).
- [26] J. C. Schön and M. Jansen, Angew. Chem., Int. Ed. Engl. **35**, 1286 (1996).
- [27] D. Chandler, in *Classical and Quantum Dynamics in Condensed Phase Simulations*, edited by B. J. Berne, G. Cicotti, and D. F. Coker (World Scientific, Singapore, 1998).
- [28] H. Eyring, J. Chem. Phys. **3**, 107 (1935).
- [29] E. Wigner, Trans. Faraday Soc. **34**, 29 (1938).
- [30] C. J. Cerjan and W. H. Miller, J. Chem. Phys. **75**, 2800 (1981).
- [31] J. P. K. Doye and D. J. Wales, Z. Phys. D **40**, 194 (1997).
- [32] P. G. Bolhuis, D. Chandler, C. Dellago, and P. L. Geissler, Annu. Rev. Phys. Chem. **53**, 291 (2002).
- [33] J. B. Anderson, J. Chem. Phys. **58**, 4684 (1973).
- [34] C. H. Bennett, *Algorithms for Chemical Computations* (R. E. Christoffersen, Washington D. C.: Amer. Chem. Soc., 1998).
- [35] D. Chandler, J. Chem. Phys. **68**, 2959 (1978).
- [36] H. Grubmüller, Phys. Rev. E **52**, 2893 (1995).
- [37] A. Laio and M. Parrinello, Proc. Natl. Acad. Sci. USA **99**, 12562 (2002).
- [38] M. Iannuzzi, A. Liao, and M. Parrinello, Phys. Rev. Lett. **90**, 238302 (2003).
- [39] S. Melchionna, Phys. Rev. E **62**, 8762 (2000).
- [40] G. T. Barkema and N. Mousseau, Phys. Rev. Lett. **77**, 4358 (1996).
- [41] G. Henkelmann and H. Jónsson, J. Chem. Phys. **111**, 7010 (1999).
- [42] D. T. Gillespie, J. Comput. Phys. **28**, 395 (1978).
- [43] A. F. Voter, Phys. Rev. B **34**, 6819 (1986).
- [44] K. A. Fichthorn and W. H. Weinberg, J. Chem. Phys. **95**, 1090 (1991).
- [45] D. J. Wales, Mol. Phys. **100**, 3285 (2002).
- [46] A. F. Voter, J. Chem. Phys. **106**, 4665 (1997).
- [47] A. F. Voter, Phys. Rev. Lett. **78**, 3908 (1997).
- [48] M. R. Sørensen and A. F. Voter, J. Chem. Phys. **112**, 9599 (2000).
- [49] A. F. Voter, Phys. Rev. B **57**, R13985 (1998).
- [50] J. N. Murrell and K. J. Laidler, Trans. Faraday Soc. **64**, 371 (1968).
- [51] H. Jónsson, G. Mills, and K. W. Jacobsen, *Classical and Quantum Dynamics in Condensed Phase Simulations* (World Scientific, Singapore, 1998).
- [52] W. E. W. Ren, and E. Vanden-Eijnden, Phys. Rev. B **66**, 052301 (2002).
- [53] D. Passerone and M. Parrinello, Phys. Rev. Lett. **87**, 108302 (2001).
- [54] R. Olender and R. Elber, J. Chem. Phys. **105**, 9299 (1996).
- [55] P. Eastman, N. Grønbech-Jensen, and S. Doniach, J. Chem. Phys. **114**, 3823 (2001).
- [56] S. T. anase Nicola and J. Kurchan, Phys. Rev. Lett. **91**, 188302 (2003).
- [57] L. R. Pratt, J. Chem. Phys. **85**, 5045 (1986).
- [58] C. Dellago, P. G. Bolhuis, F. S. Csajka, and D. Chandler, J. Chem. Phys. **108**, 1964 (1998).
- [59] C. Dellago, P. G. Bolhuis, and D. Chandler, J. Chem. Phys. **108**, 9263 (1998).
- [60] C. Dellago, P. G. Bolhuis, and D. Chandler, Faraday Discuss. **110**, 421 (1998).
- [61] D. Frenkel and B. Smit, *Understanding Molecular Simulation: From Algorithms to Applications, Second Edition* (Academic Press, San Diego, California, 2002).
- [62] D. Chandler, *Introduction to Modern Statistical Mechanics* (Oxford University Press, New York, 1987).
- [63] L. R. Pratt, J. Chem. Phys. **85**, 5045 (1986).
- [64] R. Car and M. Parrinello, Phys. Rev. Lett. **55**, 2471 (1985).
- [65] D. P. Landau and K. Binder, *A Guide to Monte Carlo Simulations in Statistical Physics* (Cambridge University Press, Cambridge, 2000).

- [66] N. Metropolis, A. W. Rosenbluth, M. N. Rosenbluth, A. H. Teller, and E. Teller, *J. Chem. Phys.* **21**, 1087 (1953).
- [67] C. Dellago, P. G. Bolhuis, and P. D. Geissler, *Adv. Chem. Phys.* **123**, 1 (2002).
- [68] C. Dellago, P. G. Bolhuis, and D. Chandler, *J. Chem. Phys.* **110**, 6617 (1999).
- [69] S. Nakamura and G. Fasol, *The Blue Laser Diode - GaN-based Light Emitters and Lasers* (Springer-Verlag, Berlin Heidelberg, 1997).
- [70] H. Morkoc, S. Strite, G. B. Gao, M. E. Lin, B. Sverdlov, and M. Burns, *J. Appl. Phys.* **76**, 1363 (1994).
- [71] S. Nakamura, *MRS Bull.* **22**, 29 (1997).
- [72] J. M. Olsen, D. J. Friedman, and S. Kurtz, in *Handbook of Photovoltaic Science and Engineering*, edited by A. Luque and S. Hegedus (Wiley, Chichester England, 1997).
- [73] T. Lei, M. Fanciulli, R. J. Molnar, T. D. Moustakas, R. J. Graham, and J. Scanlon, *Appl. Phys. Lett* **59**, 944 (1991).
- [74] B. M. Shi, M. H. Xie, H. S. Wu, N. Wang, and S. Y. Tong, *Appl. Phys. Lett* **89**, 151921 (2006).
- [75] C. Stampfl and C. G. V. de Walle, *Phys. Rev. B* **59**, 5521 (1999).
- [76] J. Serrano, A. Rubio, E. Fernández, A. Muñoz, and A. Mujica, *Phys. Rev. B* **62**, 16612 (2000).
- [77] J. A. V. Vechten, *Phys. Rev.* **182**, 891 (1969).
- [78] E. Kittle, R. Wentzkowitch, R. Jeanloz, and M. L. Cohen, *Nature* **337**, 349 (1989).
- [79] A. Mujica, A. Rubio, A. Muñoz, and R. J. Needs, *Rev. Mod. Phys.* **75**, 863 (2003).
- [80] V. Ozoliņš and A. Zunger, *Phys. Rev. Lett.* **82**, 767 (1999).
- [81] Q. Cui, Y. Pan, W. Zhang, X. Wang, J. Zhang, T. Cui, Y. Xie, J. Liu, and G. Zou, *J. Phys.: Condens. Matter* **14**, 11041 (2002).
- [82] P. Perlin, C. Jauberthie-Carillon, J. P. Itie, A. S. Miguel, I. Grzegory, and A. Polian, *Phys. Rev. B* **45**, 83 (1992).
- [83] H. Xia, Q. Xia, and A. L. Ruoff, *Phys. Rev. B* **47**, 12925 (1993).
- [84] M. Ueno, M. Yoshida, A. Onodera, O. Shimomura, and K. Takemura, *Phys. Rev. B* **49**, 14 (1994).
- [85] S. Uehara, T. Masamoto, A. Onodera, M. Ueno, O. Shimomura, and K. Takemura, *J. Phys. Chem. Solids* **58**, 2093 (1997).
- [86] Y. Tagaki, M. Ahart, T. Azuhata, T. Sota, K. Suzuki, and S. Nakamura, *Physica B* **219**, 547 (1996).
- [87] M. D. Drory, J. W. I. Ager, T. Suzuki, I. Grzegory, and S. Porowski, *Appl. Phys. Lett* **69**, 4044 (1996).
- [88] A. Muñoz and K. Kunc, *Phys. Rev. B* **44**, 10372 (1991).
- [89] I. Gorczyca and N. E. Christorsen, *Solid State Commun.* **80**, 335 (1991).
- [90] P. E. V. Camp, V. E. V. Doren, and J. T. Devreese, *Solid State Commun.* **81**, 23 (1992).
- [91] R. Pandey, M. Causa, N. M. Harrison, and M. Seel, *J. Phys.: Condens. Matter* **8**, 3993 (1996).
- [92] Z. W. Chen, M. Y. Lv, L. X. Li, Q. Wang, X. Y. Zhang, and R. P. Liu, *Thin Solid Films* **515**, 2433 (2006).
- [93] F. Bechstedt, J. Furthmüller, and J.-M. Wagner, *Phys. Stat. Sol. (c)* **6**, 1732 (2003).
- [94] J. W. Orton and C. T. Foxon, *Rep. Prog. Phys.* **61**, 1 (1998).
- [95] F. Bernardini, V. Fiorentini, and D. Vanderbilt, *Phys. Rev. B* **56**, R10024 (1997).
- [96] J. A. Croll, *Phys. Rev.* **157**, 623 (1967).
- [97] S. H. Tolbert and A. P. Alivisatos, *J. Chem. Phys.* **102**, 4642 (1995).
- [98] S. M. Sharma and Y. M. Gupta, *Phys. Rev. B* **58**, 5964 (1998).
- [99] M. D. Knudson, Y. M. Gupta, and A. B. Kunz, *Phys. Rev. B* **59**, 11704 (1999).

- [100] S. Limpijumnong and W. R. L. Lambrecht, *Phys. Rev. Lett.* **86**, 91 (2001).
- [101] H. Sowa, *Acta Cryst. A* **57**, 176 (2001).
- [102] F. Shimojo, S. Kodiyalam, I. E. o, R. K. Kalia, A. Nakano, and P. Vashishta, *Phys. Rev. B* **70**, 184111 (2004).
- [103] H. Sowa, *Acta Cryst. A* **61**, 325 (2005).
- [104] C. Capillas, J. M. Perez-Mato, and M. I. Aroyo, *J. Phys.: Condens. Matter* **19**, 275203 (2007).
- [105] H. T. Stokes, J. Gunter, D. M. Hatch, J. Dong, H. Wang, and J. P. Lewis, *Phys. Rev. B* **76**, 012102 (2007).
- [106] A. M. Saitta and F. Decremps, *Phys. Rev. B* **70**, 035214 (2004).
- [107] S. Leoni and R. Nesper, *Acta Cryst. A* **56**, 383 (2000).
- [108] S. Leoni and D. Zahn, *Z. Kristallogr.* **219**, 339 (2004).
- [109] H. G. von Schnering and R. Nesper, *Angew. Chem., Int. Ed. Engl.* **26**, 1059 (1987).
- [110] W. Smith and T. R. Forester, *J. Mol. Graphics* **14**, 136 (1996).
- [111] S. Melchionna, G. Ciccotti, and B. L. Holian, *Mol. Phys.* **78**, 533 (1993).
- [112] P. Zapol, R. Pandey, and J. D. Gale, *J. Phys.: Condens. Matter* **9**, 9517 (1997).
- [113] B. G. Dick and A. W. Overhauser, *Phys. Rev.* **112**, 90 (1958).
- [114] P. C. Donohue, *Inorg. Chem.* **9**, 335 (1970).
- [115] U. Schwarz and K. Syassen, *High Press. Res.* **9**, 148 (1992).
- [116] J. F. Liu, S. Yin, H. P. Wu, Y. W. Zeng, X. R. Hu, Y. W. Wang, G. L. Lv, and J. Z. Jiang, *J. Phys. Chem. B* **110**, 21588 (2006).
- [117] D. Zahn and S. Leoni, *Phys. Rev. Lett.* **92**, 250201 (2004).
- [118] J. A. Chisholm, D. W. Lewis, and P. D. Bristowe, *J. Phys.: Condens. Matter* **11**, L235 (1999).
- [119] F. A. Ponce and D. P. Bour, **386**, 351 (1997).
- [120] L. Brus, *Science* **276**, 373 (1997).
- [121] A. Hernández Battez, R. González, J. L. Viesca, J. E. Fernández, J. M. Díaz Fernández, A. Machadoc, R. Choud, and J. Riba, *Wear* **265**, 422 (2008).
- [122] C. Klingshirn, *Phys. Chem. Phys.* **8**, 782 (2007).
- [123] C. W. Bunn, *Proc. Phys. Soc. London* **47**, 835 (1935).
- [124] V. A. Coleman and C. Jagadish, in *Zinc Oxide Bulk, Thin Films and Nanostructures*, edited by C. Jagadish and S. J. Pearton (Elsevier, Amsterdam, The Netherlands, 2006).
- [125] K. Ellmer, A. Klein, and B. Rech, in *Transparent Conductive Zinc Oxide*, edited by K. Ellmer, A. Klein, and B. Rech (Springer-Verlag, Berlin Heidelberg, 2008).
- [126] L. Geward and J. S. Olsen, *Synchrotron Radiat.* **2**, 233 (1995).
- [127] E. H. Kisi and M. M. Elcombe, *Acta Cryst. C* **45**, 1867 (1989).
- [128] J. E. Jaffe and A. C. Hess, *Phys. Rev. B* **48**, 7903 (1993).
- [129] A. B. M. Almamun Ashrafi, A. Ueta, A. Avramescu, H. Kumano, and I. Suemune, *Appl. Phys. Lett* **76**, 550 (2000).
- [130] S.-K. Kim, S.-Y. Jeong, and C.-R. Cho, *Appl. Phys. Lett* **82**, 562 (2003).
- [131] F. Decremps, J. Zhang, and R. C. Liebermann, *Europhys. Lett.* **51**, 268 (2000).
- [132] H. Karzel, W. Potzel, M. Kofferlein, W. Schiessl, M. Steiner, U. Hiller, G. M. Kalvius, D. W. Mitchell, T. P. Das, P. Blaha, K. Schwarz, and M. P. Pasternak, *Phys. Rev. B* **53**, 11425 (1996).
- [133] S. Desgreniers, *Phys. Rev. B* **58**, 14102 (1998).
- [134] F. Decremps, J. Pellicer-Porres, F. Datchi, J. P. Itié, A. Polian, F. Baudalet, and J. Z. Jiang, *Appl. Phys. Lett* **81**, 48 (2002).
- [135] H. Liu, Y. Ding, M. Somayazulu, J. Qian, J. Shu, D. Häusermann, and H. K. Mao, *Phys. Rev. B* **71**, 212103 (2005).



- [136] C. H. Bates, W. B. White, and R. Roy, *Science* **137**, 993 (1962).
- [137] J. Z. Jiang, J. S. Olsen, L. Gerward, D. Frost, D. Rubie, and J. Peyronneau, *Europhys. Lett.* **50**, 48 (2000).
- [138] S.-Y. Chen, P. Shen, and J. Jiang, *J. Chem. Phys.* **121**, 11309 (2004).
- [139] J. E. Jaffe, J. A. Snyder, Z. Lin, and A. C. Hess, *Phys. Rev. B* **62**, 1660 (2000).
- [140] J. Uddin and G. E. Scuseria, *Phys. Rev. B* **74**, 245115 (2006).
- [141] Y. Mori, N. Niiya, K. Ukegawa, T. Mizuno, K. Takarabe, and A. L. Ruoff, *Phys. Stat. Sol. (b)* **241**, 3198 (2004).
- [142] U. Özgür, Y. I. Alivov, C. Liu, A. Teke, M. A. Reshchikov, S. Doğan, V. Avrutin, S.-J. Cho, and H. Morkoç, *App. Phys. Rev.* **98**, 041301 (2005).
- [143] A. K. Tagantsev, *Appl. Phys. Lett.* **93**, 202905 (2008).
- [144] Y. C. Yang, C. Song, X. H. Wang, F. Zeng, and F. Pan, **92**, 012907 (2008).
- [145] Z. Alahmed and H. Fu, *Phys. Rev. B* **77**, 045213 (2008).
- [146] A. A. Mostofi, J. R. Yates, Y.-S. Lee, I. Souza, D. Vanderbilt, and N. Marzari, *Comput. Phys. Commun.* **178**, 685 (2008).
- [147] J. C. Phillips, *Bonds and bands in Semiconductors* (Academic, New York, 1973).
- [148] G. C. Zhou, L. Z. Sun, J. B. Wang, X. L. Zhong, and Y. C. Zhou, *Physica B* **403**, 2832 (2008).
- [149] A. R. H. Preston, B. J. Ruck, L. F. J. Piper, A. DeMasi, K. E. Smith, A. Schleife, F. Fuchs, F. Bechstedt, J. Chai, and S. M. Durbin, *Phys. Rev. B* **78**, 155114 (2008).
- [150] H. Q. Ni, Y. F. Lu, and Z. M. Ren, *J. Appl. Phys.* **91**, 1339 (2002).
- [151] C. G. Van de Walle, *J. Phys.: Condens. Matter* **20**, 064230 (2008).
- [152] J. E. Jaffe, R. Pandey, and A. B. Kunz, *Phys. Rev. B* **43**, 14030 (1991).
- [153] H. Karzel, W. Potzel, M. Köfferlein, W. Schiessl, M. Steiner, U. Hiller, and G. M. Kalvius, *Phys. Rev. B* **53**, 11425 (1996).
- [154] A. Qteish, *J. Phys.: Condens. Matter* **12**, 5639 (2000).
- [155] H. Sowa and H. Ahsbahs, *App. Cryst.* **39**, 169 (2005).
- [156] S. Limpijumngong and S. Jungthawan, *Phys. Rev. B* **70**, 054104 (2004).
- [157] F. Decremps, J. Pellicer-Porres, A. M. Saitta, J.-C. Chervin, and A. Polian, *Phys. Rev. B* **65**, 092101 (2002).
- [158] H. Wu, X. Cheng, H. Zhang, and Z. Liu, *Phil. Mag. Lett.* **88**, 181 (2008).
- [159] F. Decremps, J. Zhang, B. Li, and R. C. Liebermann, *Phys. Rev. B* **63**, 224105 (2001).
- [160] F. Decremps, F. Datchi, A. M. Saitta, A. Polian, S. Pascarelli, A. Di Cicco, J. P. Itié, and F. Baudelet, *Phys. Rev. B* **68**, 104101 (2003).
- [161] J. Serrano, A. H. Romero, F. J. Manjón, R. Lauck, M. Cardona, and A. Rubio, *Phys. Rev. B* **69**, 094306 (2004).
- [162] A. Zaoui and W. Sekkal, *Phys. Rev. B* **66**, 174106 (2002).
- [163] A. M. Saitta, D. Alfè, S. de Gironcoli, and S. Baroni, *Phys. Rev. Lett.* **78**, 4958 (1997).
- [164] M. Catti, *Phys. Rev. Lett.* **87**, 035504 (2001).
- [165] D. J. Binks and R. W. Grimes, *J. Amer. Ceram. Soc.* **76**, 2370 (1993).
- [166] G. V. Lewis and C. R. A. Catlow, *J. Phys. C* **18**, 1149 (1985).
- [167] A. J. Kulkarni, K. Sarasamak, J. Wang, F. J. Ke, S. Limpijumngong, and M. Zhou, *Mech. Res. Commun.* **35**, 73 (2008).
- [168] P. Ruterana, M. Abouzaid, A. Béré, and J. Chen, *J. Appl. Phys.* **103**, 033501 (2008).
- [169] J. M. Calleja and M. Cardona, *Phys. Rev. B* **16**, 3753 (1977).
- [170] E. Morris, T. Groy, and K. Leinenweber, *J. Phys. Chem. Solids* **62**, 1117 (2001).
- [171] K. F. Seifert, *Ber. Bunsenges. Phys. Chem.* **70**, 1041 (1966).
- [172] D. P. Dandekar, , and J. C. Jamieson, *Trans. Am. Crystallogr. Assoc.* **5**, 19 (1969).
- [173] L. Gerward, J. S. Olsen, S. Steenstrup, S. Åsbrink, and A. Waskowaska, *J. Appl. Crystallogr.* **25**, 578 (1992).

## 110 Bibliography

- [174] A. M. Pendás, J. M. Rico, M. Flórez, and V. Luaña, *Phys. Rev. B* **49**, 5858 (1994).
- [175] S. Speziale and T. S. Duffy, *Phys. Chem. Miner.* **29**, 465 (2002).
- [176] V. Kanchana, G. Vaitheeswaran, and M. Rajagopalan, *Physica B* **328**, 283 (2003).
- [177] F. S. El'kin, O. B. Tsiok, L. G. Khvostantsev, and V. V. Brazhkin, *Phys. Rev. B* **73**, 094113 (2006).
- [178] R. Khenata, B. Daoudi, M. Sahnoun, H. Baltache, M. Rérat, A. H. Reshak, B. Bouhaf, H. Abid, and M. Driz, *Eur. Phys. J. B* **47**, 63 (2005).
- [179] J. Haines, J. M. Leger, and O. Schulte, *Phys. Rev. B* **57**, 7551 (1998).
- [180] J. M. Leger, J. Haines, and A. Atouf, *Phys. Rev. B* **51**, 3902 (1995).
- [181] V. Kanchana, G. Vaitheeswaran, and M. Rajagopalan, *J. Alloys Compd.* **359**, 66 (2003).
- [182] X. Wu, S. Qin, and Z. Wu, *Phys. Rev. B* **73**, 134103 (2006).
- [183] Y. Ma and M. Rohlfing, *Phys. Rev. B* **75**, 205114 (2007).
- [184] G. W. Rubloff, *Phys. Rev. B* **5**, 662 (1972).
- [185] E. L. Shirley, *Phys. Rev. B* **58**, 9579 (1998).
- [186] J. B. Boyce and B. A. Huberman, *Phys. Rep.* **51**, 189 (1979).
- [187] K. Schmalzl, D. Strauch, and H. Schober, *Phys. Rev. B* **68**, 144301 (2003).
- [188] M. T. Hutchings, *J. Phys. C: Solid State Phys.* **17**, 3903 .
- [189] S. E. Boulfelfel, D. Zahn, O. Hochrein, Y. Grin, and S. Leoni, *Phys. Rev. B* **74**, 094106 (2006).
- [190] M. Valle, *Z. Kristallogr.* **220**, 585 (2005).
- [191] J. Maier, *Nature* **4**, 805 (2005).
- [192] B. C. Wood and N. Marzari, *Phys. Rev. Lett.* **97**, 166401 (2006).
- [193] V. Bitrián, J. Trullàs, and M. Silbert, *J. Chem. Phys.* **126**, 021105 (2007).
- [194] B. L. Davis and L. H. Adams, *Science* **146**, 519 (1964).
- [195] J.-S. Lee, S. Adams, and J. Maier, *J. Electrochem. Soc.* **147**, 2407 (2000).
- [196] Y.-G. Guo, J.-S. Lee, Y.-S. Hu, and J. Maier, *J. Electrochem. Soc.* **154**, K51 (2007).
- [197] A. Hao, C. Gao, M. Li, C. He, X. Huang, G. Zou, Y. Tian, and Y. Ma, *J. Appl. Phys.* **101**, 053701 (2007).
- [198] H. Sowa, *Z. Kristallogr.* **222**, 89 (2007).
- [199] P. R. Prager, in *Crystal Growth and Characterization of Polytype Structures*, edited by S. Chandra (North Holland, Amsterdam, 1983).
- [200] B. L. Davis and L. R. Johnson, *Cryst. Lattice Defects* **5**, 235 (1974).
- [201] H. Arima, O. Ohtaka, T. Hattori, Y. Katayama, W. Utsumi, and A. Yoshiasa, *J. Phys.: Condens. Matter* **19**, 076104 (2007).
- [202] O. Ohtaka, H. Takebe, A. Yoshiasa, H. Fukui, and Y. Katayama, *Solid State Commun.* **123**, 213 (2002).
- [203] D. A. Keen and S. Hull, *J. Phys.: Condens. Matter* **5**, 23 (1993).
- [204] Y. Li, L. J. Zhang, T. Cui, Y. W. Li, Y. Wang, Y. M. Ma, and G. T. Zou, *J. Phys.: Condens. Matter* **20**, 195218 (2008).
- [205] R. C. Hanson, T. A. Fjeldly, and H. D. Hochheimer, *Phys. Stat. Sol. (b)* **70**, 567 (1975).
- [206] S. Hull and D. A. Keen, *Phys. Rev. B* **59**, 750 (1999).
- [207] J.-H. Chang, A. Zürn, and H. G. von Schnering, *Z. Anorg. Allg. Chem.* **634**, 2156 (2008).
- [208] L. Palomino-Rojas, M. López-Fuentes, G. H. Coccoletzi, G. Murrieta, R. de Coss, and N. Takeuchi, *Solid State Sciences* **10**, 1228 (2008).
- [209] Y.-G. Guo, J.-S. Lee, and J. Maier, *Solid State Ionics* **177**, 2467 (2006).
- [210] A. R. Oganov, J. Chen, C. Gatti, Y. Ma, Y. Ma, C. W. Glass, Z. Liu, T. Yu, O. O. Kurakevych, and V. L. Solozhenko, *Nature* **453**, 863 (2009).

- [211] Y. Ma, M. Eremets, A. R. Oganov, Y. Xie, I. Trojan, S. Medvedev, A. O. Lyakhov, M. Valle, and V. Prakapenka, *Nature* **458**, 182 (2009).
- [212] R. Hultgren, N. S. Gingrich, and B. E. Warren, *J. Chem. Phys.* **3**, 351 (1935).
- [213] A. Brown and S. Rundqvist, *Acta Cryst.* **19**, 684 (1965).
- [214] R. W. Keyes, *Phys. Rev.* **92**, 580 (1953).
- [215] R. Ahuja, *Phys. Stat. Sol. (b)* **235**, 282 (2003).
- [216] H. Katzke and P. Tolédano, *Phys. Rev. B* **77**, 024109 (2008).
- [217] T. Kikegawa and H. Iwasaki, *Acta Cryst. B* **39**, 158 (1983).
- [218] C. A. Vanderborgh and D. Schiferl, *Phys. Rev. B* **40**, 9595 (1989).
- [219] M. Okajima, S. Endo, Y. Akahama, and S.-I. Narita, *Jpn. J. Appl. Phys.* **23**, 15 (1984).
- [220] H. Kawamura, I. Shirovani, and K. Tachikawa, *Solid State Commun.* **49**, 879 (1984).
- [221] Y. Akahama, M. Kobayashi, and H. Kawamura, *Phys. Rev. B* **59**, 8520 (1999).
- [222] M. Marqués, G. J. Ackland, L. F. Lundegaard, S. Falconi, C. Hejny, M. I. McMahon, J. Contreras-García, and M. Hanfland, *Phys. Rev. B* **78**, 054120 (2008).
- [223] H. Fujihisa, Y. Akahama, H. Kawamura, Y. Ohishi, Y. Gotoh, H. Yamawaki, M. Sakashita, S. Takeya, and K. Honda, *Phys. Rev. Lett.* **98**, 175501 (2007).
- [224] U. Hässermann, *Chem. Eur. J.* **9**, 1472 (2003).
- [225] M. Ruck, D. Hoppe, B. Wahl, P. Simon, Y. Wang, and G. Seifert, *Angew. Chem., Int. Ed. Engl.* **44**, 7616 (2005).
- [226] J. L. Yarger and G. H. Wolf, *Science* **306**, 820 (2004).
- [227] H. Katzke, U. Bismayer, and P. Tolédano, *Phys. Rev. B* **73**, 134105 (2006).
- [228] S. Sugai, T. Ueda, and K. Murase, *J. Phys. Soc. Jpn.* **50**, 3356 (1983).
- [229] Z. Mayerová, M. Johnsson, and S. Lidin, *Angew. Chem., Int. Ed. Engl.* **45**, 5602 (2006).
- [230] G. H. Wannier, *Phys. Rev.* **52**, 191 (1937).
- [231] P. L. Silvestrelli, N. Marzari, D. Vanderbilt, and M. Parrinello, *Solid State Commun.* **107**, 7 (1998).
- [232] F. Freimuth, Y. Mokrousov, D. Wortmann, S. Heinze, and S. Blügel, *Phys. Rev. B* **78**, 035120 (2008).
- [233] N. Marzari and D. Vanderbilt, *Phys. Rev. B* **56**, 12847 (1997).
- [234] I. Souza, N. Marzari, and D. Vanderbilt, *Phys. Rev. B* **65**, 035109 (2001).
- [235] R. Hoffmann, *Solids and Surfaces: A Chemist's View of Bonding in Extended Structures* (Wiley-VCH, New York, 1988).
- [236] G. Seifert, *J. Phys. Chem. A* **111**, 5609 (2007).
- [237] G. Lippert, J. Hutter, and M. Parrinello, *Mol. Phys.* **92**, 477 (1997).
- [238] G. J. Martyna, D. J. Tobias, and M. L. Klein, *J. Chem. Phys.* **101**, 4177 (1994).
- [239] A. D. Becke, *Phys. Rev. A* **38**, 3098 (1988).
- [240] J. P. Perdew, K. Burke, and M. Ernzerhof, *Phys. Rev. Lett.* **77**, 3865 (1996).

# Acknowledgements

This work has been completed in the group of Prof. Yuri Grin at the Max-Planck-Institut für Chemische Physik fester Stoffe in Dresden from fall 2004 to 2009.

I would like to thank Prof. Yuri Grin for providing me the possibility to work on this interesting topic, guidance and support throughout this work, and fruitful discussions.

I would like to thank Dr. Stefano Leoni for his constant support, advise and assistance during my work, for sharing his knowledge about phase transitions and solid state chemistry, and helpful discussions.

I would like to thank Dr. Dirk Zahn for his help and assistance during my work, for sharing his experience in molecular dynamics simulations, and fruitful discussions.

I would like to thank Prof. Dr. Gotthard Seifert for refereeing this work and for providing me with DFTB parameters.

# Versicherung

Hiermit versichere ich, dass ich die vorliegende Arbeit ohne unzulässige Hilfe Dritter und ohne Benutzung anderer als der angegebenen Hilfsmittel angefertigt habe, die aus fremden Quellen direkt oder indirekt übernommenen Gedanken sind als solche kenntlich gemacht. Die Arbeit wurde bisher weder im Inland noch im Ausland in gleicher oder ähnlicher Form einer anderen Prüfungsbehörde vorgelegt.

Die vorliegende Dissertation wurde unter Betreuung von Herrn Prof. Yuri Grin in der Zeit von Oktober 2004 bis July 2009 am Max-Planck-Institut für Chemische Physik fester Stoffe in Dresden angefertigt.

Dresden, den